

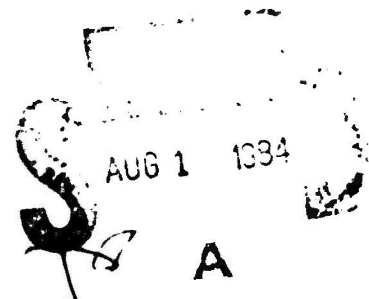


ELECTROMAGNETIC LAUNCHERS AND GUNS PHASE ONE FINAL REPORT OF THE M. I. T. GROUP

NOVEMBER 1979 TO MAY 1980

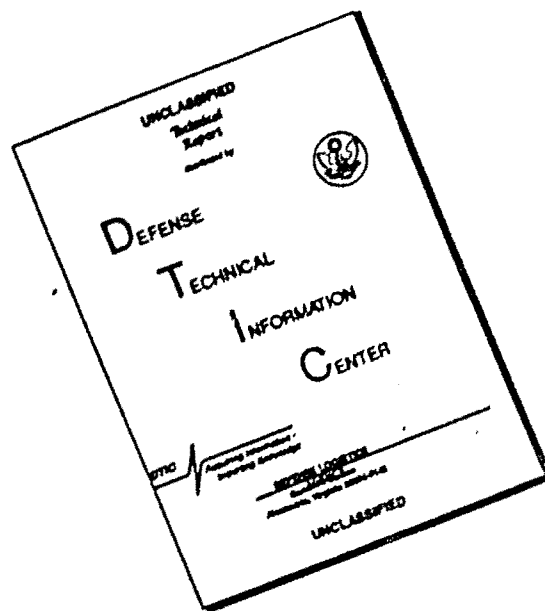
AD-A143 778

DTIC FILE COPY



CA 02 20

DISCLAIMER NOTICE



THIS DOCUMENT IS BEST QUALITY AVAILABLE. THE COPY FURNISHED TO DTIC CONTAINED A SIGNIFICANT NUMBER OF PAGES WHICH DO NOT REPRODUCE LEGIBLY.

ELECTROMAGNETIC LAUNCHERS AND GUNS
PHASE ONE FINAL REPORT
OF THE M.I.T. GROUP
NOVEMBER 1979 TO MAY 1980

Henry Kolm
Francis Bitter National Magnet Laboratory

Rene Miller
Department of Aeronautics and Astronautics

Massachusetts Institute of Technology
Cambridge, Massachusetts 02139

June 1980

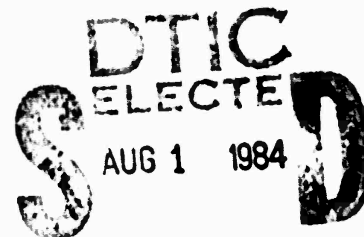
Sponsored by:

U.S. Army Armament Research and Development Command
Propulsion Technology Branch
Dover, New Jersey 07801

and by:

Defense Advanced Research Projects Agency, DoD,
Tactical Technology Division
1400 Wilson Boulevard
Arlington, Virginia 22209

Under Contract No. DAAK10-79-C-0384



Disclaimer:

The views and conclusions contained in this document are those of the authors, and should not be interpreted as representing the official policies, either expressed or implied, of the U.S. Army Armament Research and Development Command, or the U.S. Government.

ABSTRACT

A facility has been established at the M.I.T. Francis Bitter National Magnet Laboratory for studying various electromagnetic means for accelerating vehicles and projectiles to very high velocity, and for training a generation of scientists and engineers in the technologies involved. The facility has been staffed by about fourteen undergraduate and graduate students, technicians, faculty and research staff.

→ During the first six months (phase one) the group ~~has~~ constructed a 65 kJ, 6 kV fast discharge capacitor bank, a 134 kJ, 900 V slow discharge bank, and a 245 kJ, 350 V mobile bank for field launching was started. Also completed was an accelerator test bench and a protected control and observation room instrumented with digital data processing equipment. Studies have been initiated on three acceleration mechanisms, and on the theoretical limitations in general.)

() A "helical railgun" (brush-commutated helical accelerator) ~~has been~~ ^{was} bench-tested to 500 gee acceleration and 30 m/s velocity achieved over a 12 inch section. A 20 foot, twin helix launcher and optimized cargo or reconnaissance glider ~~have been~~ ^{were} designed, for construction during phase two.

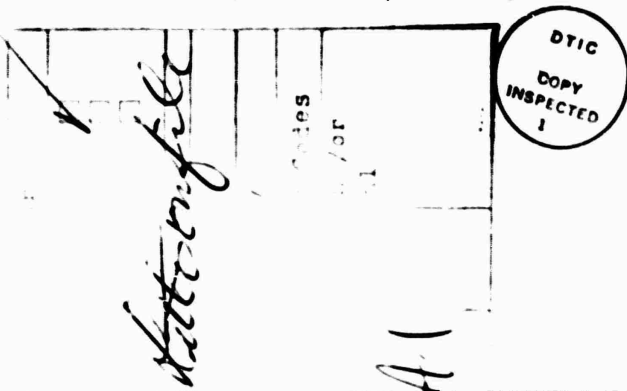
Mass driver (discrete-coil, synchronous accelerator) coils ~~have been~~ ^{were} tested to destruction over a range of pulse conditions to gain an understanding of failure modes and develop improved designs for different ranges of operation.)

→ A "momentum transformer" has been constructed for transferring momentum from a pneumatically driven sabot to a smaller projectile.

Theoretical studies indicate that the smallest vehicle capable of surviving a ground-based launch to earth escape velocity at reasonable atmospheric losses of mass and energy is a 25 kg, 6 cm caliber cylinder, and that a promising mechanism for accelerating it to escape velocity is a self-energized superconducting mass driver in which the launch energy is stored inductively in a 1 km length of superconducting drive coils of 35 cm caliber.

TABLE OF CONTENTS

ABSTRACT	1
INTRODUCTION	4
OBJECTIVES	5
PERSONNEL	8
FACILITIES	10
space and services	10
dedicated energy storage	11
the fast bank	11
the slow banks	12
instrumentation	14
THE HELICAL ACCELERATOR	15
first internal helical accelerator	15
second external helical accelerator	15
THE GLIDER LAUNCHER	27
general configuration	27
mechanical design	29
electrical design	29
THE GLIDER	36
general objectives	36
trajectory analysis	37
initial design	59
PULSED COIL DYNAMICS	72
THE MOMENTUM TRANSFORMER	75
basic principle	75
experimental apparatus	76
preliminary results	78



(continued next page)

TABLE OF CONTENTS, CONTINUED

MASS DRIVER TWO CRYOGENIC SYSTEM	80
results of tests	84
thermal behavior	84
electrical behavior	84
conclusions	85
EARTH-BASED SPACE LAUNCHERS	86
rationale for catapults	86
the telephone pole launcher	92
the self-energized, superconducting mass driver	94
APPENDIX A	96
THE DYNAMIC DEFORMATION OF PULSED CURRENT COILS	
APPENDIX B	120
THE SELF-ENERGIZED, SUPERCONDUCTING MASS DRIVER AS A MEANS FOR LAUNCHING SPACE VEHICLES FROM EARTH	

INTRODUCTION

The MIT National Magnet Laboratory was built in 1960-1963 with funding by the Air Force Office of Scientific Research (AFOSR) to serve as a center of expertise in the generation of very intense magnetic fields, and their application to solid state and plasma research. It was named in honor of Francis Bitter, who built the first high field research facility at MIT in 1936. Support of the laboratory has since been taken over by the National Science Foundation, with substantial contribution from the Department of Energy to the Alcator fusion research project. The core powerplant is capable of generating up to 32 MW of highly regulated dc power, and has been supplemented with a pulsed power capability of 225 MW dedicated to the Alcator machine. The laboratory provides high fields to visiting researchers from government, university and industry, and also maintains in-house research in solid state, plasma and superconductivity physics. The laboratory also serves the DoE as designer and contracting officer for large MHD magnets.

Work in propulsion began in 1970, when Henry Kolm and Richard Thornton developed the MIT Magneplane, a high-speed maglev transportation system based on a linear synchronous motor [1,2,3]. In 1975 Gerard K. O'Neill of Princeton University recognized the applicability of this mechanism to launchers, and there followed the development of Mass Drivers for launching lunar raw materials to space construction sites. The collaboration was supported by NASA in two NASA-AMES summer studies in 1976 and 1977 [4,5] and in joint grants to MIT and Princeton [6].

In 1978 Dr. Harry Fair, Chief of the Propulsion Branch of ARRADCOM, sponsored a preliminary survey of all practical electromagnetic accelerating mechanisms and their applicability to DoD requirements. The conclusions were presented at the JANNAF meeting in March 1979 [7] and elsewhere [8,9,10]. Henry Kolm also assisted in establishing a Technical Advisory Panel on Electromagnetic Guns and Launchers to bring all available resources and expertise to bear on planning a coordinated r&d program.

The work reported here represents the first six-month phase of MIT's contribution to such a program.

OBJECTIVES

It is the main purpose of this project to establish a facility for studying all electromagnetic accelerating mechanisms of interest, without prejudice toward existing capability or equipment, and to train a first generation of experts in the basic science and engineering of this art. To this end, we draw on the entire MIT student body, graduate and undergraduate, without departmental barriers. Our group operates at a high level of involvement and enthusiasm.

Four tasks have been selected as deserving first-priority attention, considering the fact that the very important railgun-homopolar launcher technology is already being pursued at Westinghouse and University of Texas, Austin.

The helical railgun, or brush-commutated helical accelerator, consists of a short coil sliding inside or outside a helical barrel. The sliding coil and adjacent segments of the barrel are energized by rings of brushes surrounding the helical barrel. The device seems well suited for accelerating heavy vehicles to relatively moderate velocities, but the efficiency and performance limits were completely unknown. It is our objective to construct and bench-test a short segment of helical accelerator, and on the basis of the knowledge thus gained to design a half-scale field launcher and glider vehicle, to be constructed during phase two. The full-scale launcher is intended to launch 50 pound gliders for reconnaissance purposes, or for transporting cargo over inaccessible terrain. The launcher is intended to operate at 100 gee acceleration, 100 m/s (224 mph) velocity, with a range of several miles. A larger version to be designed in the future would accelerate a 300 pound stretcher vehicle at 5 gee for medical evacuation purposes.

The accelerators intended for launching purposes will have external slide coils. This configuration provides easy access to the brushes and helical barrel surfaces for studying the commutation processes, arcing damage, etc. On the basis of tests with the external sliders we hope to establish the performance limits of helical accelerators for internal use in artillery applications.

The study will also generate trade-off curves for launched glider design.

Mass drivers, or discrete-coil synchronous accelerators in general, are limited in performance by failure of the vehicle coil or of the drive coils. Failure of the vehicle coil is governed by a relatively straightforward thermal limit, but failure of the drive coils is a complex problem which has not been studied for large-caliber, thin-build pulse coils. Depending on the operating regime, failure may be thermal, static or dynamic. We wish to correlate the observed failure of simple coils with computer models to determine the performance limit of mass driver type accelerators, and means to design drive coil structures for maximum performance.

Momentum transfer flux compressors, or momentum transformers, are devices in which a metal sabot provided with a radial slot is accelerated chemically (or pneumatically, in our tests) into a region of strong magnetic field confined by a copper barrel. The magnetic flux, which cannot penetrate the sabot in the available time, is thereby concentrated into the inner bore of the slotted sabot, so that the field intensity is increased by about the ratio of outside to inside cross section. A conducting projectile located inside the sabot is thereby expelled by induced eddy currents, carrying with it a hopefully large fraction of the sabot's momentum at a correspondingly higher velocity. We plan to study the mechanism by inductance simulation, using alternating currents and a dummy sabot, and by pneumatically driving a one inch caliber sabot into a field coil.

There are certain theoretical limits on the performance of the basic acceleration processes, imposed by materials, energy transfer rates, losses, etc. We are interested in defining the performance limits of the helical accelerator in terms of thrust, efficiency (heating), projectile size, and speed, insofar as these limits can be derived from experimental data, for extrapolation to the larger launchers for tactical use.

We are also interested in deriving the theoretical melting limit for multiple impulse inductors, that is accelerators which drive short-circuited, passive coils or washers by synchronized pulse coils of the mass driver type.

Finally, we intend to determine the feasibility of launching space vehicles electromagnetically, the minimum vehicle size for survival, the mass and energy losses in traversing the atmosphere, and the suitability of various energy storage and accelerating mechanisms.

The group has one additional mission, funded by NASA-LEWIS rather than ARRADCOM-DARPA, which we include in the present report because of its relevance to DoD applications: design and construction of the superconducting bucket and associated cryogenic service station for Mass Driver Two. The station serves to cool the bucket to liquid helium temperature, induce a persistent current in its two coils, and inject it into the mass driver being built at Princeton University. We will then collaborate with Princeton in testing the overall system, and obtain experimental data on the performance limit of superconducting bucket coils under the field transients involved in mass driver type accelerators.

This work fills a gap in the present DoD program, which does not as yet include a cryogenic/superconducting system. We believe that such systems will be of importance in two contexts: linear inertial energy storage in Pulsar type devices, such as those developed by Cowan at Sandia [11], and inductive energy storage for space launchers and possibly also tactical and strategic launchers. Relatively little is known about the behavior of hard superconductors under fast transients, and other groups at the National Magnet Laboratory are beginning to investigate this area.

PERSONNEL

The following persons contributed to the Phase One work, in the manner indicated.

Henry Kolm, Senior Scientist (Natl. Magnet Lab), Lecturer (Aero.Astro Dept.)
co-principal investigator, electromagnetics

Rene Miller, Professor, Aeronautics and Astronautics Department
co-principal investigator, aerodynamics

Peter Mongeau, BS, Physics, Doctoral Candidate, Physics
crew chief, supervises all projects, makes job assignments, concentrates on theoretical analysis and instrumentation; conceptual planning;

Fred Williams, BS, Mechanical Engineering; veteran of magneplane and pulsed metal forming projects; chief designer and constructor, with special responsibility for capacitor switching and safety; idea generation; procurement of surplus equipment; improvisation and adaptation;

Peter Graneau, Ph.D., Elect. Engr., specialist in cryo-cables, circuit breakers, physics of metal vapor arcs, electromagnetic theory; 20% time consultant; special responsibility for quench-gun analysis and arc-commutation; fundamental analysis;

Whitney Hamnett, Electro-Mechanical Project Technician; BS in art;
shop manager, responsible for documentation and illustration, detail designing, special responsibility for cryogenic systems and tests.

Al Djiauw, Electro-Mechanical Project Technician; pulsed field experience; special responsibility for design and construction of capacitor banks and switching circuitry, fabrication of helical launcher booms, test bench facilities;

Ken McKinney, third year student, candidate for BS in Physics and Mech Engr.
has worked on undergrad. thesis and later as student employee; special responsibility for data processing, computer-modelling of coil dynamics, and management of the Digital PDP-11 system and interface.

Osa Fitch, third year student, candidate for BS in Aeronautical Engr.;
working on undergrad. thesis project (UROP, "Undergrad. Research Opportunity" project) for academic credit; responsible for coil dynamics project experimentation, planning to do BS thesis for project later;

Robert Sharp, third year student, candidate for BS in Physics;
Working on UROP project for credit, coil dynamics experiments.

Michael Paluszek, BS, Aeronautical Engr.,
Part time; did glider trajectory trade-off analysis and basic design;

Mark Zeitlin, BS, Aeronaut. Engr., Candidate for MS;
Responsible for structural design and construction of glider vehicle, radio control, instrumentation, and aeronautical testing;

Lika Levi, third year student at Bryn Mawr College, Candidate for BS in Physics;
Joined project for one-week externship during spring vacation; may
return as student employee later if needed.

Roger Durst, fourth year student, candidate for BS in Aeronautical Engineering;
Working as student employee on construction of launcher booms and
capacitor banks; may join project as graduate student for MS;

Kevin Maguire, high school student; part-time employee;
will work as summer student employee, special case community service;

The following additional persons are associated with the Mass Driver
group at Princeton:

Gerard K. O'Neill, Professor of Physics, Princeton University
author of "The High Frontier" and leading advocate of space colonization.

William Snow, MS, Aeronautical Engineering,
former graduate student at MIT and veteran of the Mass Driver One group,
responsible for design and construction of the main part of Mass
Driver Two.

FACILITIES

SPACE AND SERVICES

The group now occupies about 3,000 square feet of office and laboratory space, with room for expansion as required. There is an adjacent garage area where the trailer-mounted twin-helix launcher can be assembled, and a little-used railroad siding where initial launching tests can be made. Available in the same building are heavy shop facilities, including lathes large enough to fabricate modules of helical barrels up to eight feet long.

The area has access to the main powerplant which can furnish up to 32 MW of continuous dc power (160 kA at 200 V), and Bitter solenoids with fields up to 220 kG (22 Tesla), oriented horizontally or vertically. The laboratory also owns various capacitor banks which are available for occasional use.

The central research area, 30 x 40 feet, is surrounded by a wire cage. A massive wood test bench 40 ft long was constructed along one wall of this cage, and a plywood observation and control room was built in one corner for protection against noise and debris, and to secure the digital data storage equipment.



Fig. 1. Overall view of central research area completed in January 1980. Test bench at left, control room in far right corner. Fred Williams and Peter Mongeau in background.

DEDICATED ENERGY STORAGE

THE FAST DISCHARGE BANK

Thirty-six 6 KV, 100 mf pyranol capacitors obtained as government surplus from the Princeton Synchrontron were assembled into a fast-discharge, 65 KJ bank.

The bank is divided into six modules of six cans, each housed in a commercial polyethylene tank with 0.25 inch walls on a caster dolly, as shown at right.

Cans are connected individually to RG 217 type coaxial cables in the manner shown, one side of the capacitors being grounded to the cans. The tanks are thus needed for fault protection as well as for PCB containment.

A linear spark gap triggered by four automobile spark plugs was constructed. It is capable of discharging one 6-can module and operates reliably at 1,000 as well as 6,000 volts. A larger version capable of accepting the 36 co-axial leads from all six modules has been designed.

The six modules will fit into six neighboring bays underneath the test bench; two are visible in Fig.

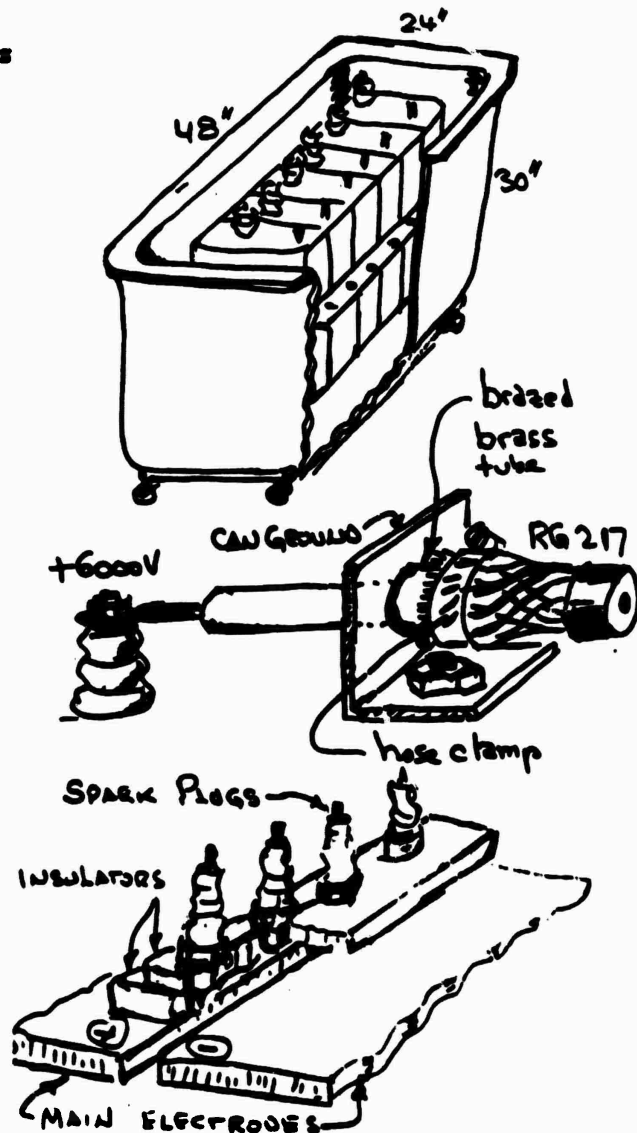


Fig. 2 The 6 KV, 65 KJ fast discharge capacitor bank, connections, and spark gap switch.

THE SLOW DISCHARGE BANKS

We have two slow-discharge capacitor banks made of beer can electrolytics obtained as surplus from the dismantled Princeton Synchrotron. A crowbarred laboratory bank has been completed, and a field bank for use with the trailer-mounted launcher is being assembled.

The laboratory bank uses 960 beer cans, each 3100 mf at 300 V storing 140 J, with a total storage capacity of 134.4 kJ at 900 V.

The bank consists of 40 modules containing 24 cans wired 8 in parallel and 3 in series as shown at right. Each module has its own SCR for initiating its discharge and for reverse fault current protection, as well as a crowbar diode to sustain the discharge current and prevent back-swing when feeding a low-resistance load.

The modules weigh 50 pounds each and are made of 2x8 hemlock planking, with mating top and bottom edges to permit stacking, as shown in Fig. 4. The aluminum current bus connections protrude from the front panel and are protected by the protruding side-walls. Stacked modules can thus be connected easily by vertical aluminum straps.

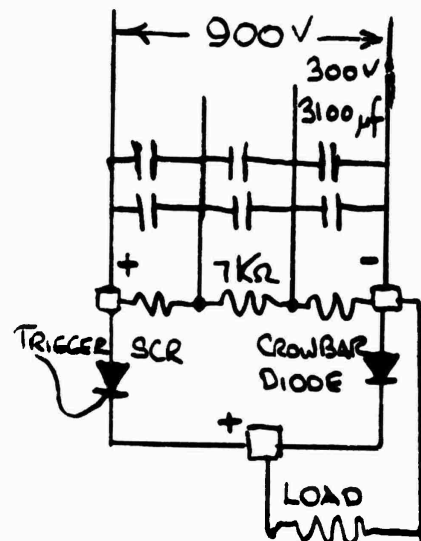


Fig. 3. Circuit of 24-can module of laboratory bank

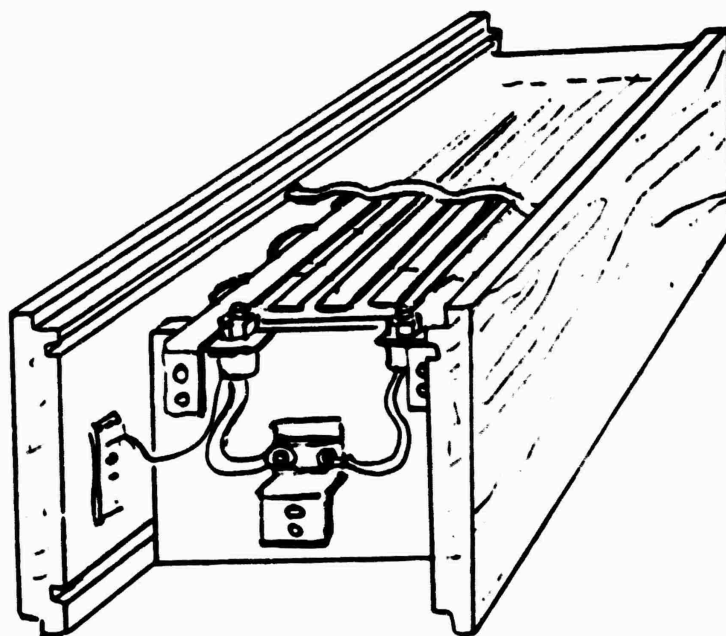
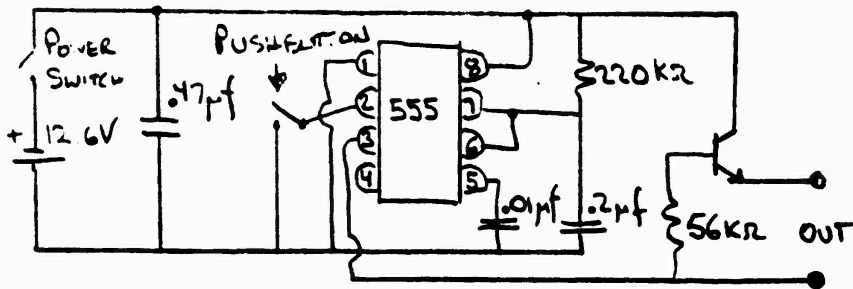
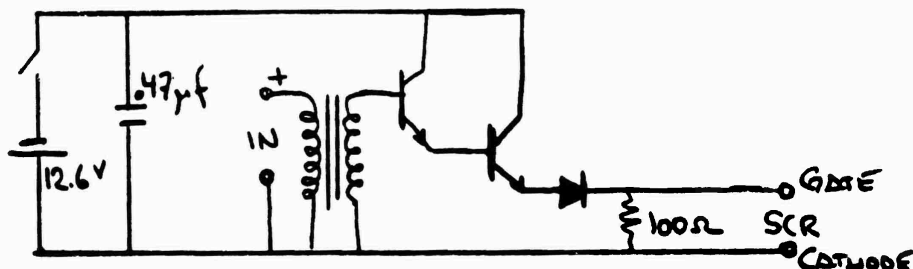


Fig. 4. Enclosure of 24-can, 50-pound stacking modules of laboratory bank.



PULSE GENERATOR CIRCUIT



SCR TRIGGER CIRCUIT

Fig. 5. Discharge controls for the laboratory bank

A standard pulse-forming and SCR trigger circuit shown in Fig. 5 was built, battery operated and transformer coupled to permit complete isolation from the line and prevent premature triggering. This triggered up to three modules. A direct cascade method was later developed to trigger all of the modules.

In practical terms, the whole bank can deliver about 200 KA at 900 V for 0.75 ms. It can thus be thought of as a 180 MW power supply, with a 0.75 ms duty cycle, delivering 134.4 KJ altogether. The bare capacitors have a power density of 70 joule/pound (2 pounds/can).

The mobile bank now being assembled consists of 1600 beer can units, each 2500 mf at 350 V storing 153 J, with a total storage capacity of 245 KJ. It will be parallel-connected for 350 V operation, which matches the helical launcher's impedance plus back-voltage. The cans are being mounted in 4 steel shelving units, the total weight of the bank being 3,200 pounds. The cans will be individually SCR-fired, but without crowbarring diodes. Staggered triggering will ensure quasi-constant current during the launch cycle. The actual, bare-can energy storage

density, referred to the bare capacitor cans, is 76.5 joule/pound.

For comparison, we note that launching the 12.5 pound (5.67 kg) glider to 224 mph (100 m/s) at 80 percent efficiency requires only 36 KJ , or 465 pounds of capacitors. The portable bank thus suffices for testing the launcher to 6.8 times the mass of the model, or 2.6 times the design velocity.

Two charging supplies are available: a 50 KV, 0.2 A unit for the 6 KV bank, and a 2 KV 4 A unit for the 900 V bank. Both were reconditioned from dead storage.

A mobile charging supply for field use to charge the 300 V launching bank will be constructed to be operable on line power or on a gasoline-driven 2.5 KW generator. All of the control and instrumentation for the field launcher will be operated from the 12 V truck battery through a 60 Hz inverter in order to make it independent of the generator.

INSTRUMENTATION

The backbone of our instrumentation system is a Nicolet Explorer digital oscilloscope, which is capable of storing 4,000 data points at time intervals of 50 nanosecond to 20 second per point. All points can be used to store a single variable during a transient event, or they can be used to store up to four variables simulataneously by cycling the points. Once stored on the floppy disk, the data can be displayed, scanned, expanded in the x and y directions, and processed directly by an available Digital PDP-11 computer. A micro-computer will be added to permit on-line computation while experiments are being made.

A set of four optical position sensors has been constructed to provide a measured position reference.

THE HELICAL ACCELERATOR

FIRST, INTERNAL HELICAL ACCELERATOR

A crude, two-foot section of internal helical railgun was first constructed in about two working days, to obtain a feeling for the problems involved. It was made by winding cotton-insulated, one eighth inch square copper wire on a phenolic tube, potting the helix in epoxy, removing the winding mandrel, and honing the inside surface down to bare copper with an expandable cylinder hone. The sabot was a simple, push-only bucket with two carbon brushes, supplied with current through a tether cable from a 12 V lead-acid battery.

The slider reached 5 m/s on battery power, and 15 m/s when energized with electrolytic capacitors, at which point it failed because the accelerating force stripped the coil from the phenolic tube which carried the brushes easily from the outside. External barrels are limited in length by the stiffness of their internal support tube because they can only rest at the breech, or the breech and muzzle if the slider is captive. They are more accessible for research purposes.

SECOND, EXTERNAL HELICAL ACCELERATOR

The second model was made of rectangular, 0.125 x 0.100 inch copper wire wound on the outside of a four inch o.d. phenolic cloth reinforced tube 32 inches long. Spacing between turns was governed by the cotton insulation. The winding was epoxy-impregnated and then machined to a cylinder with a tolerance of about 0.002 inch overall taper.

The external slider is shown full-scale in Fig. 6 on the following page in section, and an isometric sketch appears in Fig. 7. Current will ultimately be supplied through external feed brushes, but the bench model was supplied through a tether cable for simplicity and ease of instrumentation. The electrical specifications are summarized in Fig. 8, and some photographs of the bench model accelerator appear in Fig. 9.

The principle of the brush-commutated helical accelerator is best illustrated by Fig. 6, an axial section through the slider. A helical barrel coil (not shown) is surrounded by a short sliding coil which is supplied with current through two sliding brushes. The sliding coil also carries two sets of commutating brushes at each end which serve to energize adjacent sections of the barrel helix in opposite directions so that the sliding coil is pulled from the front and pushed from behind. Each commutating brush set consists of a ring of fingers which surrounds the entire circumference of the helical barrel, made by slotting a bronze tube as shown in Fig. 7. The inboard brush set is supported by a re-entrant tube to place the brushes as close to the sliding coil as possible.

It is an essential feature of this design that the current flowing to the brush sets exerts repulsive forces between the three nesting coaxial tubes which support the brushes. Brush pressure will therefore increase with increasing current, providing the outermost tube can withstand the cumulative force.

The factors which determine the performance limit of a helical accelerator are the effective system resistance, the inductance coupling coefficient between sliding coil and excited sections of the barrel, and the brush current density achievable at an acceptable service life. The mass of the slider is a trade-off variable.

System resistance (and maximum permissible drive current) can of course be improved by simply using more copper in both the helical barrel and the sliding coil, but this will place the two interacting currents farther apart, thus lowering the coupling constant, and also increase the slider mass, thus lowering the acceleration for a given thrust.

To explore performance limitations in the short bench model, the slider was provided with only two inboard and two outboard brush fingers in the pull-mode commutator (pull-only operation), and its coil only had four layers. It is shown in the photograph of Fig. 9A.

The bench tests were made by energizing the accelerator only momentarily with one module stack of the electrolytic capacitor bank containing 0.165 farad at variable charging voltages up to about 600 volts. The exact dimensions of sliding coil and energized helical coils are shown in Fig. 8, along with the electrical parameters.

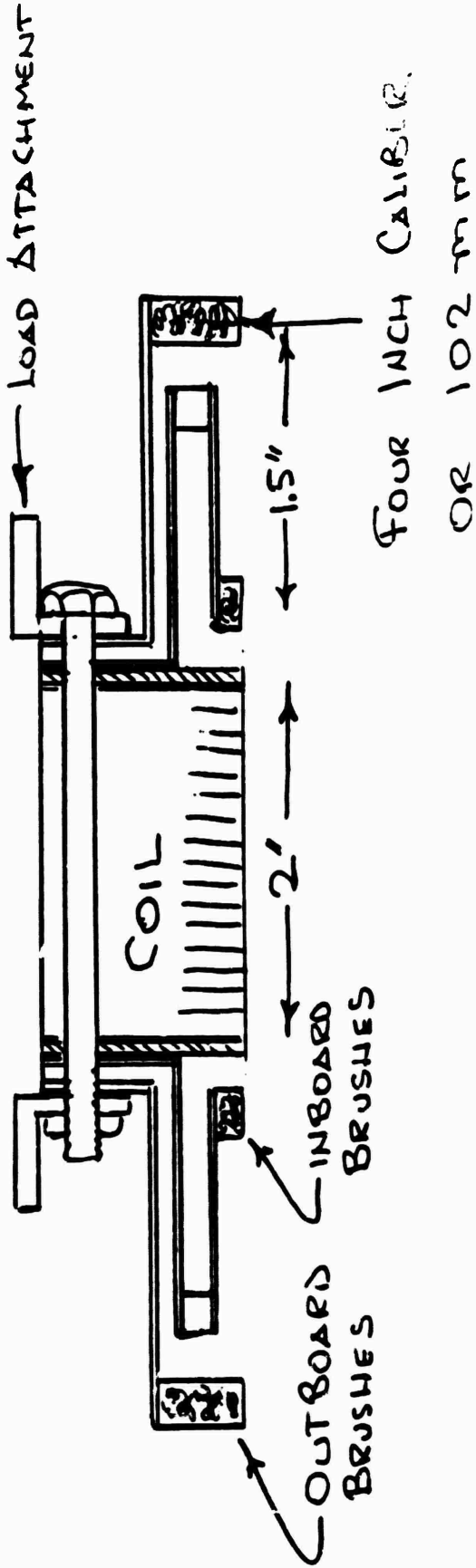
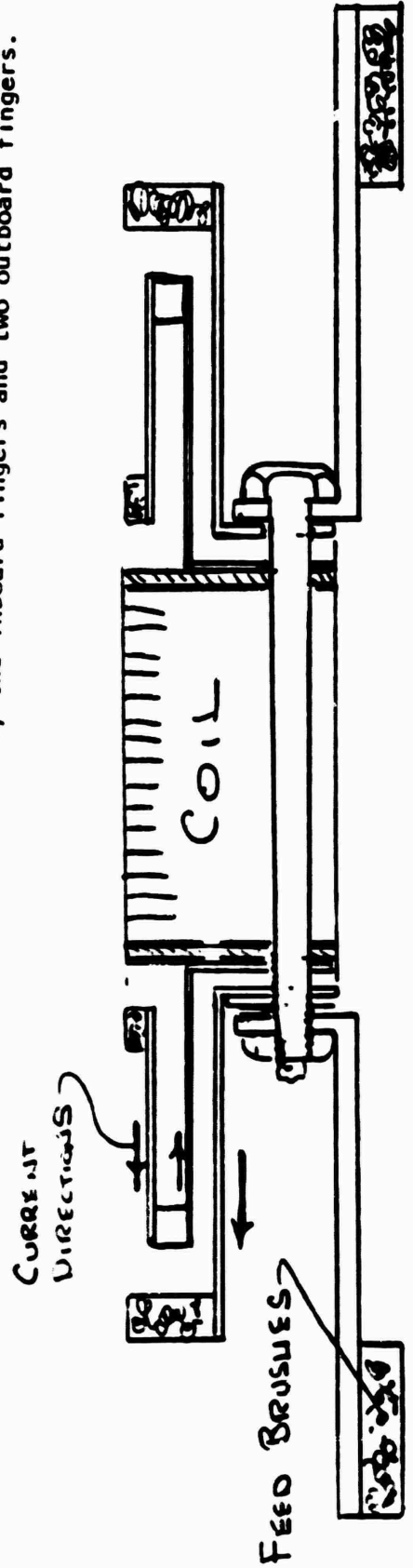


Fig. 6 Bench model helical accelerator with external slider; full scale section; brushes ultimately will surround entire circumference, but first test model brushes had only two inboard fingers and two outboard fingers.



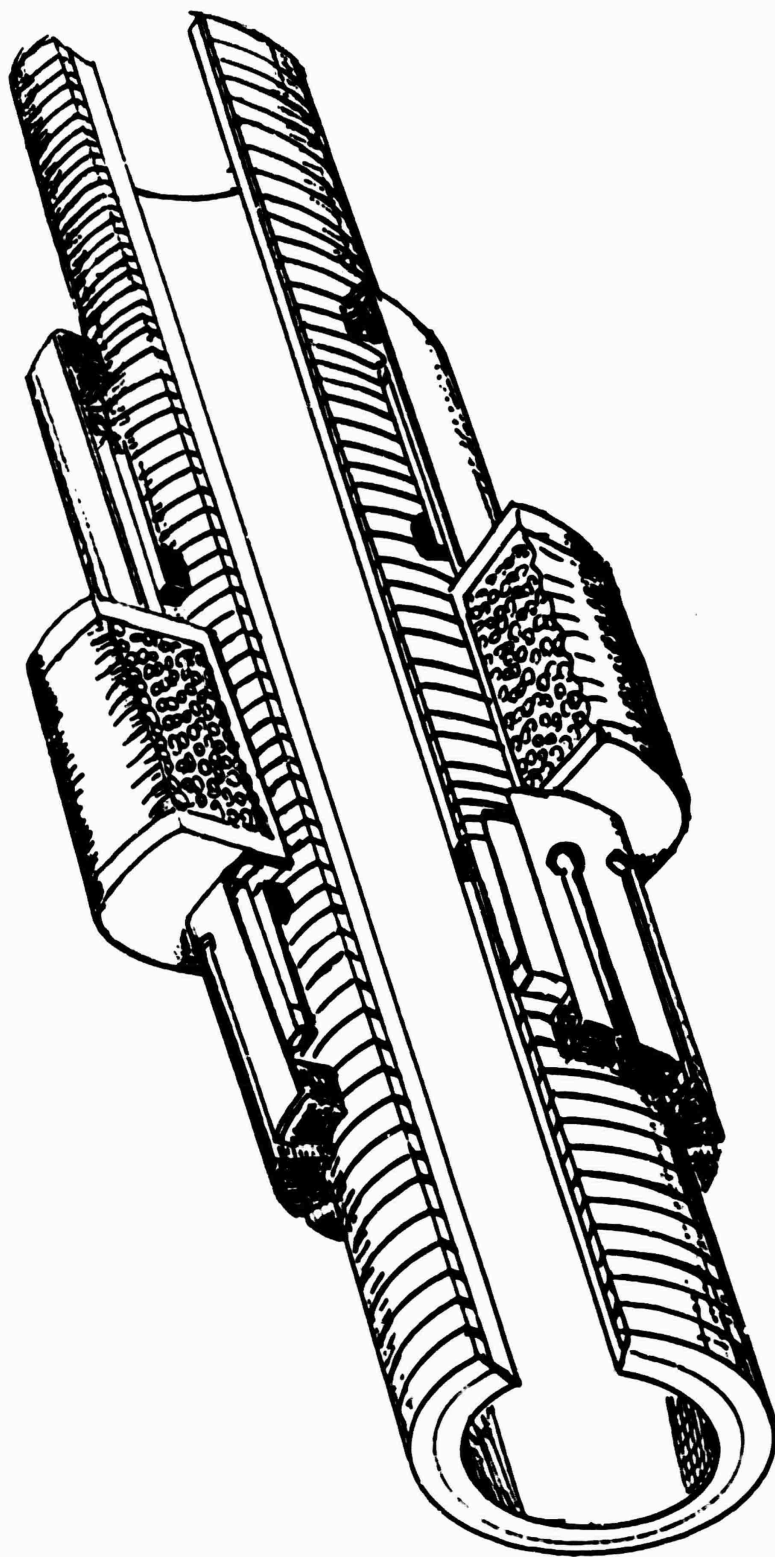
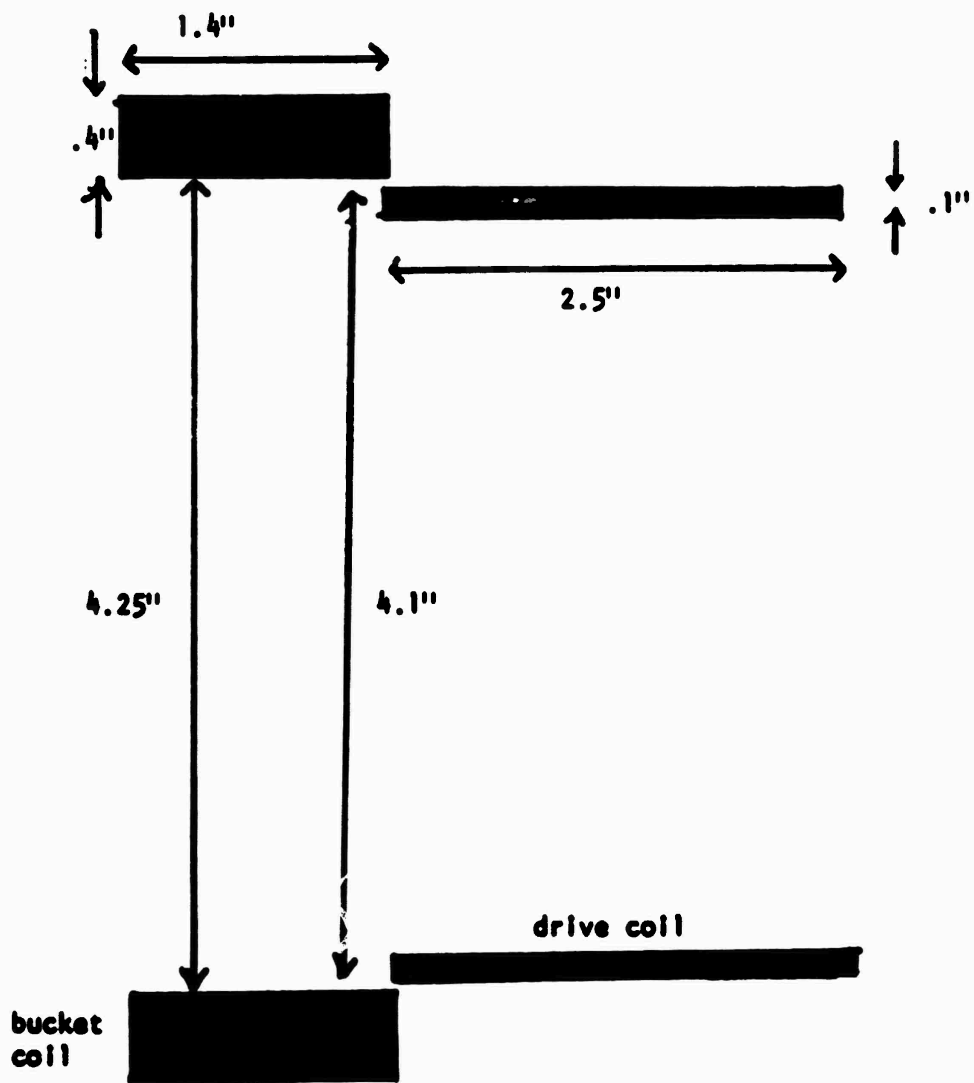


Fig. 7

Push-pull helical accelerator with four circumferential commutator brush sets. Current will be supplied to the slider by two additional rail brushes, not shown. The bench test model has only two brush fingers, one active coil layer, and is fed by a tether cable. The glider launcher will use two such barrels side-by-side with the glider cradled between the two sliders. Sliders will return to breech end after launch.



bucket mass : 2.3 kg

winding material : bucket coil : copper

drive coil : copper

bucket coil resistance : .022 ohms

drive coil resistance : .008 ohms

accelerator length : 0.8 meters

Fig. 8 Electrical specifications of bench model helical accelerator; helical barrel has single layer winding, bucket coil has four layer winding.

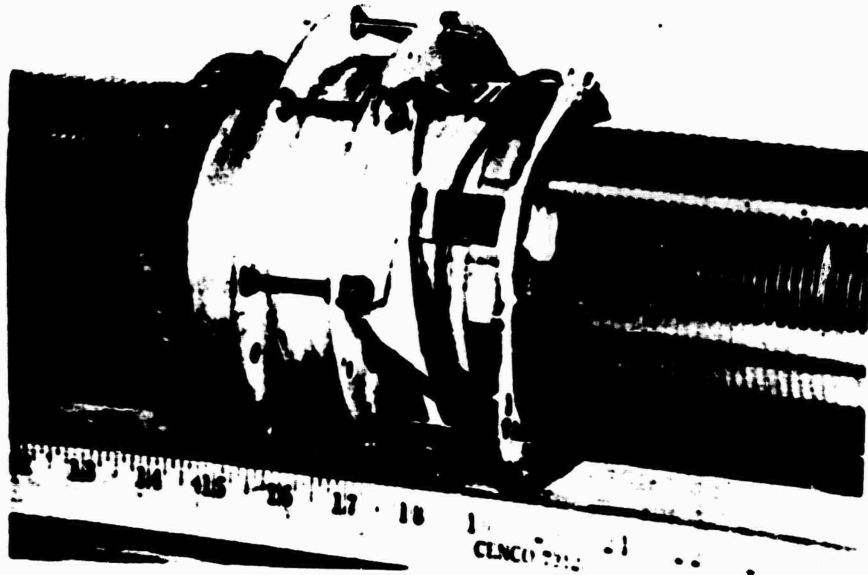


Fig. 9A Bench model helical accelerator with only two brush fingers in trailing and leading commutator and only four coil layers.

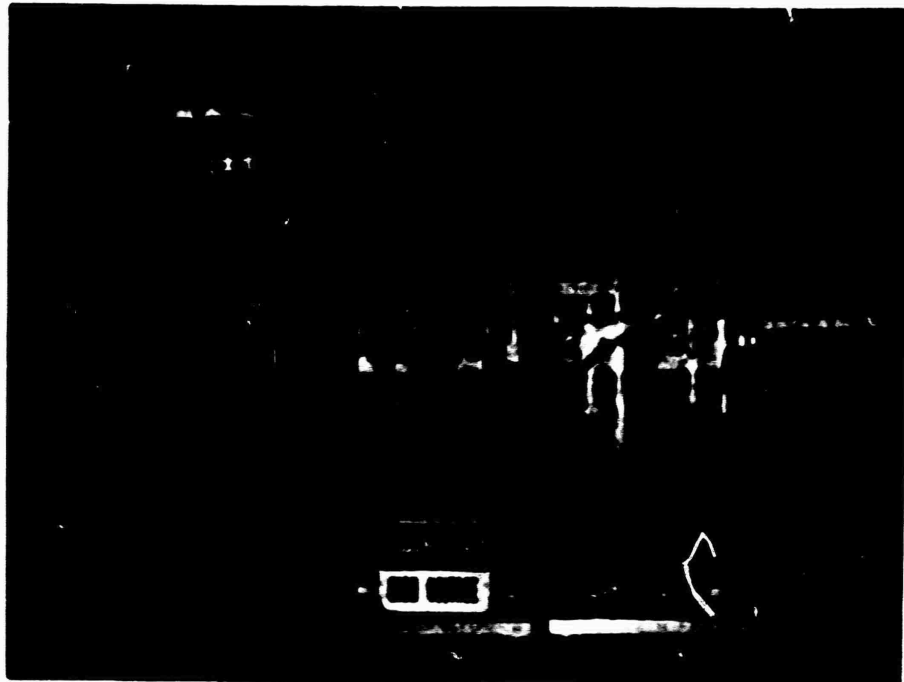


Fig. 9B Two modules of electrolytic capacitor bank used to drive bench model helical accelerator.

Test results are summarized graphically in the next four figures. Fig. 10 is a plot of the peak current as a function of capacitor voltage, and its slope defines the "effective system resistance" as 0.057 ohm. This corresponds to the slider with only four coil layers and four brush fingers operating in the pull-only mode.

Fig. 11 is a plot of the slider momentum versus current impulse measured with only the innermost of the four coil layers energized. The slope of this curve, namely the proportionality constant between the product of slider current and helix current (which are the same) and the propulsion force, is the effective mutual inductance gradient, or dM/dx , between the sliding coil and the energized section of helix. It turns out to be 1.10×10^{-6} henry/meter. The slider mass was assumed to be 2.3 kg, which includes half the mass of the tether (umbilical) cable attached to the slider.

Fig. 12 is a plot of final velocity as a function to the current impulse (ampere²-seconds) with all four layers of the slider coil active. The mutual inductance gradient has now decreased to 0.84×10^{-6} h/m, reflecting the fact that the additional three layers of slider coil are farther removed from the helix and therefore contribute less to the effective mutual inductance gradient. This illustrates dramatically the importance of designing for maximum dM/dx . Adding three layers to the initial single layer coil has decreased the coupling, and thus the thrust obtained for a given current, to only 76% of its initial value.

It is encouraging to note that with only 10% of its brush area and about 20% of its coil windings, the slider reached 30 m/s in an effective acceleration length of only about one foot, and from a standing start. The objective of the glider launcher is to reach 100 m/s in a length of about 16 ft, and with a 5.7 kg gross weight glider model shared between two sliders. In other words, we intend to accelerate about twice the mass to three times the velocity in 16 times the distance, per slider. This implies 18 times the launch energy in 16 times the launch distance. We are able to use ten times the brush area and five times the number of slider coil turns. To be sure, the added turns will contribute less coupling, but this will be compensated somewhat by the fact that we can energize a section of helix behind the slider to achieve push as well as pull action.

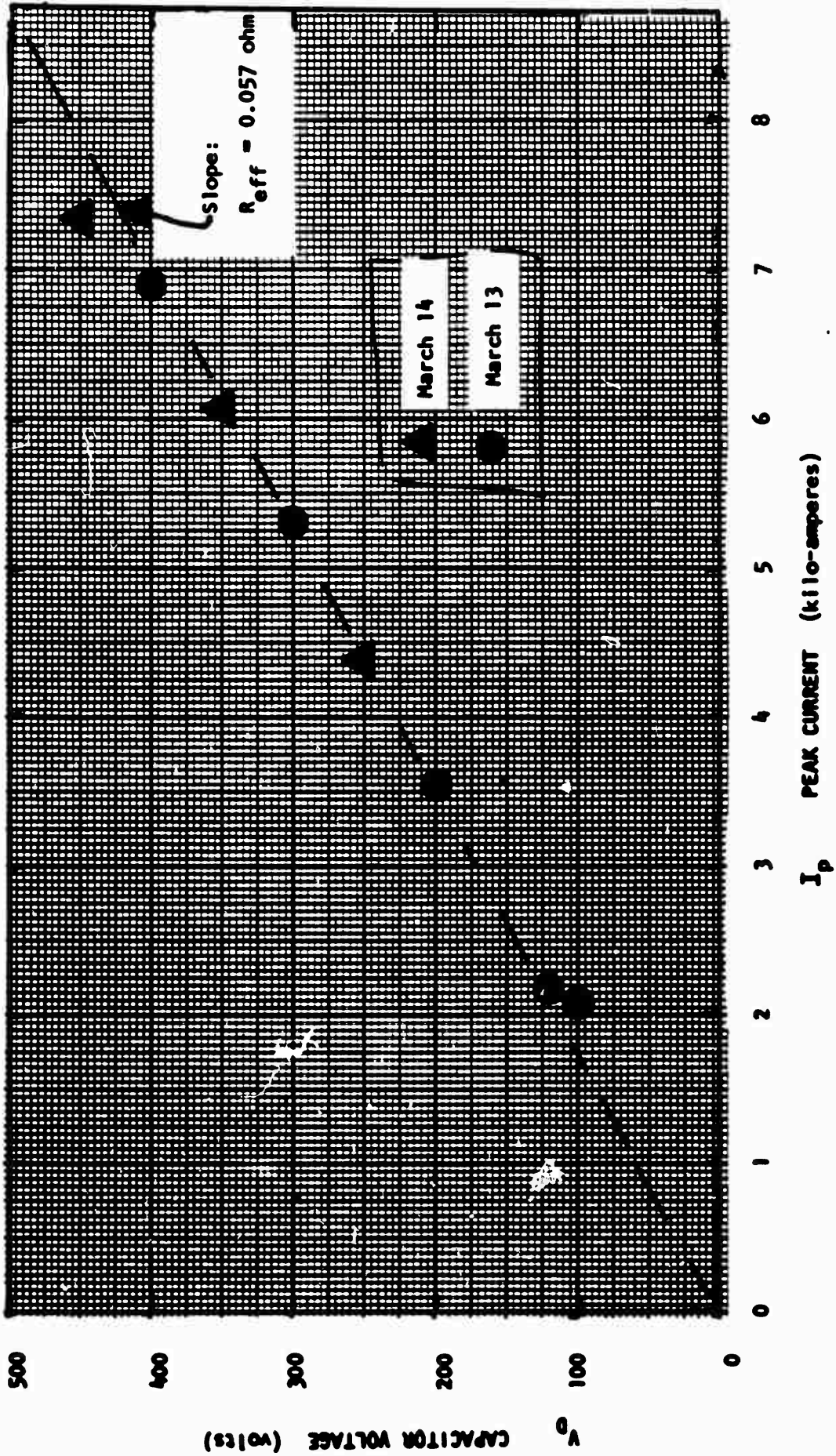


Fig. 10 Characteristics of bench model helical accelerator, external slider Capacitor voltage versus peak current at 0.165 farad capacity.

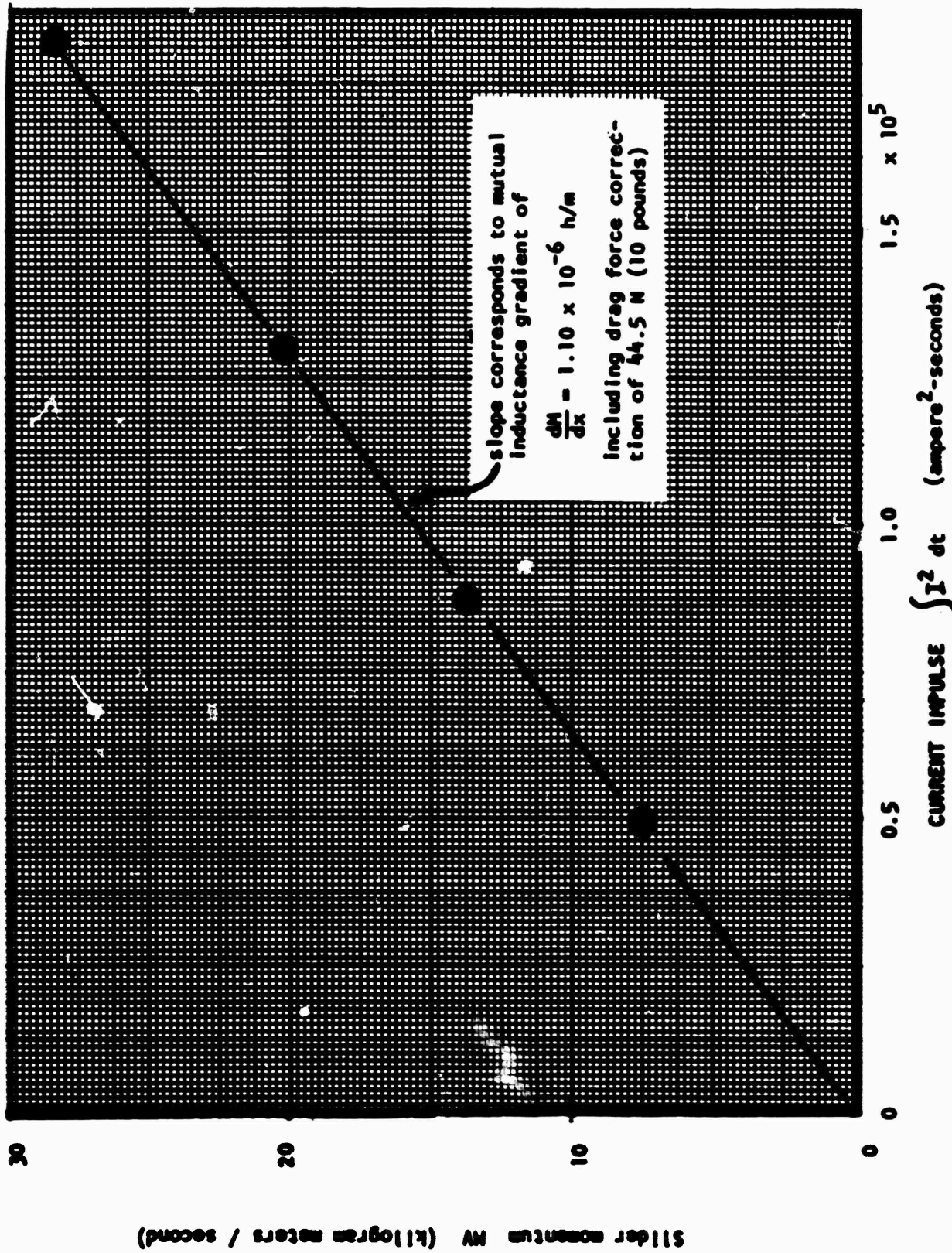


Fig. 11 Momentum versus current impulse, bench model helical accelerator, only innermost of four coil layers energized, pull brushes only, two fingers each; slider mass is 2.3 kg including half of umbilical cord mass.

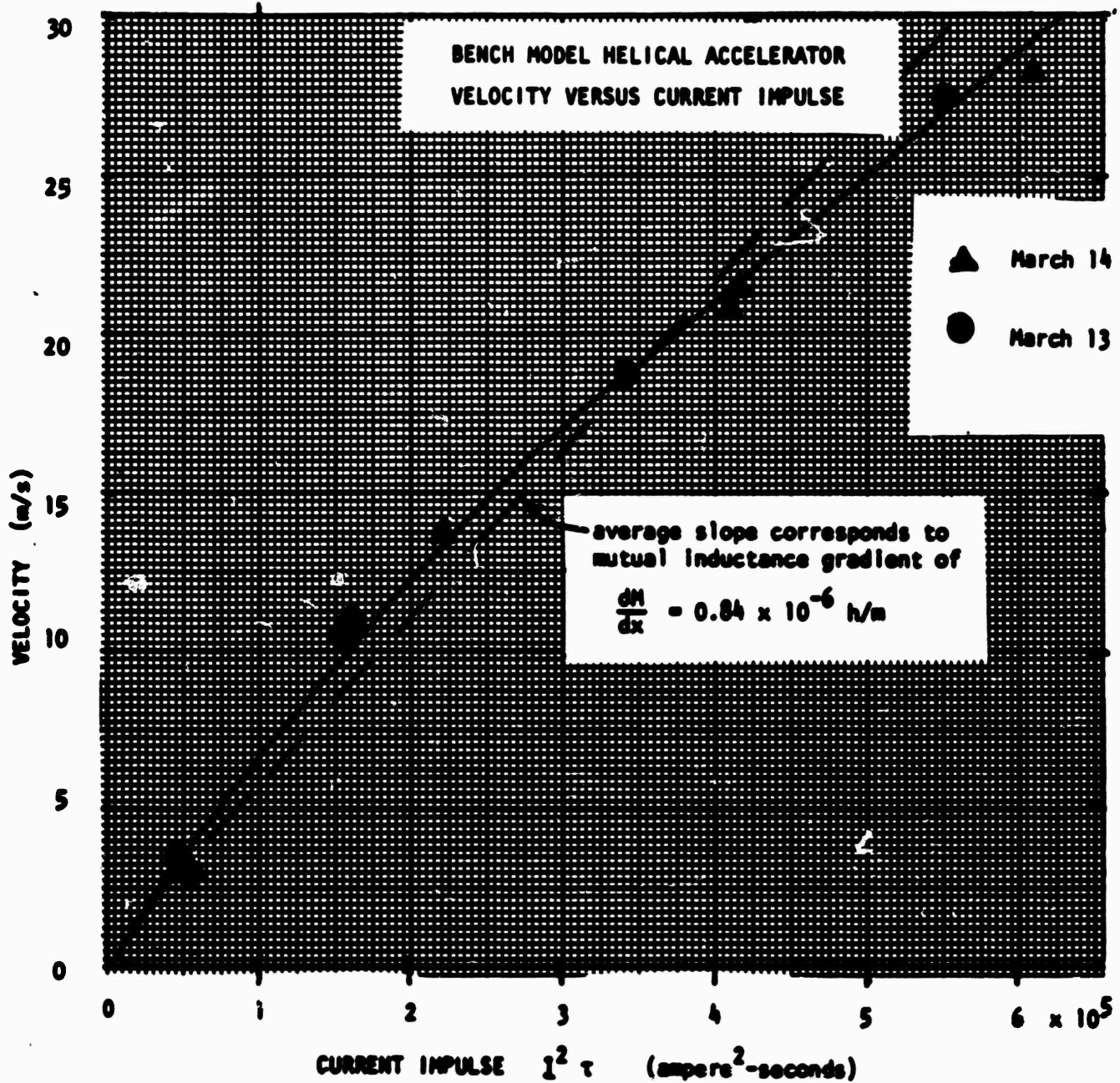


Fig. 12 Velocity versus current impulse, bench model helical accelerator, four coil layers energized, 2-finger pull brushes only, slider mass is 2.3 kg including half of umbilical cord mass.

Fig. 13 is a plot of the electro-mechanical energy conversion efficiency as extrapolated from measurements with the bench model. The equations relating efficiency to the performance parameters are also shown in Fig. 13. The "coupling constant" C is a "normalized" coefficient, namely the mutual inductance gradient dM/dx multiplied by the number of active turns N in the bucket (slider) b , and in the drive coil (helix) d . This notation is derived from the mass driver literature.

It is a fundamental property of most accelerators, including dc railguns, that efficiency increases drastically with velocity at first, and asymptotically approaches 100% eventually. This property derives from the simple fact that both thrust and resistive loss are proportional to the current squared. Thus, if the current is kept constant during acceleration, the thrust and resistive loss will both remain constant as well, but the mechanical power delivered to the slider will increase with velocity.

It will probably prove expedient to inject the slider into the active helical barrel with some initial velocity derived from a spring, compressed air piston, or induction accelerator (pulsed coil). This will eliminate the low-efficiency start, and even more importantly the high local heat input to the helix at zero velocity. The only place any significant pitting was observed in the bench test model helix was at the starting position of the commutating brushes.

The twin-boom glider launcher should achieve somewhat better efficiency than is suggested by Fig. 13 because using about ten times more commutating brush area will reduce the system resistance R significantly.

It is worth noting that helical accelerators operating in the 3 km/s velocity range should achieve efficiencies approaching 90 percent.

$$\text{force} = C I^2$$

$$\text{efficiency} = \frac{C I^2 V}{C I^2 V + I^2 R} = \frac{C V}{C V + R}$$

R = system resistance

C = coupling constant,

$$= N_b N_d \frac{dM}{dx}$$

I = current in slider and helix

V = slider velocity

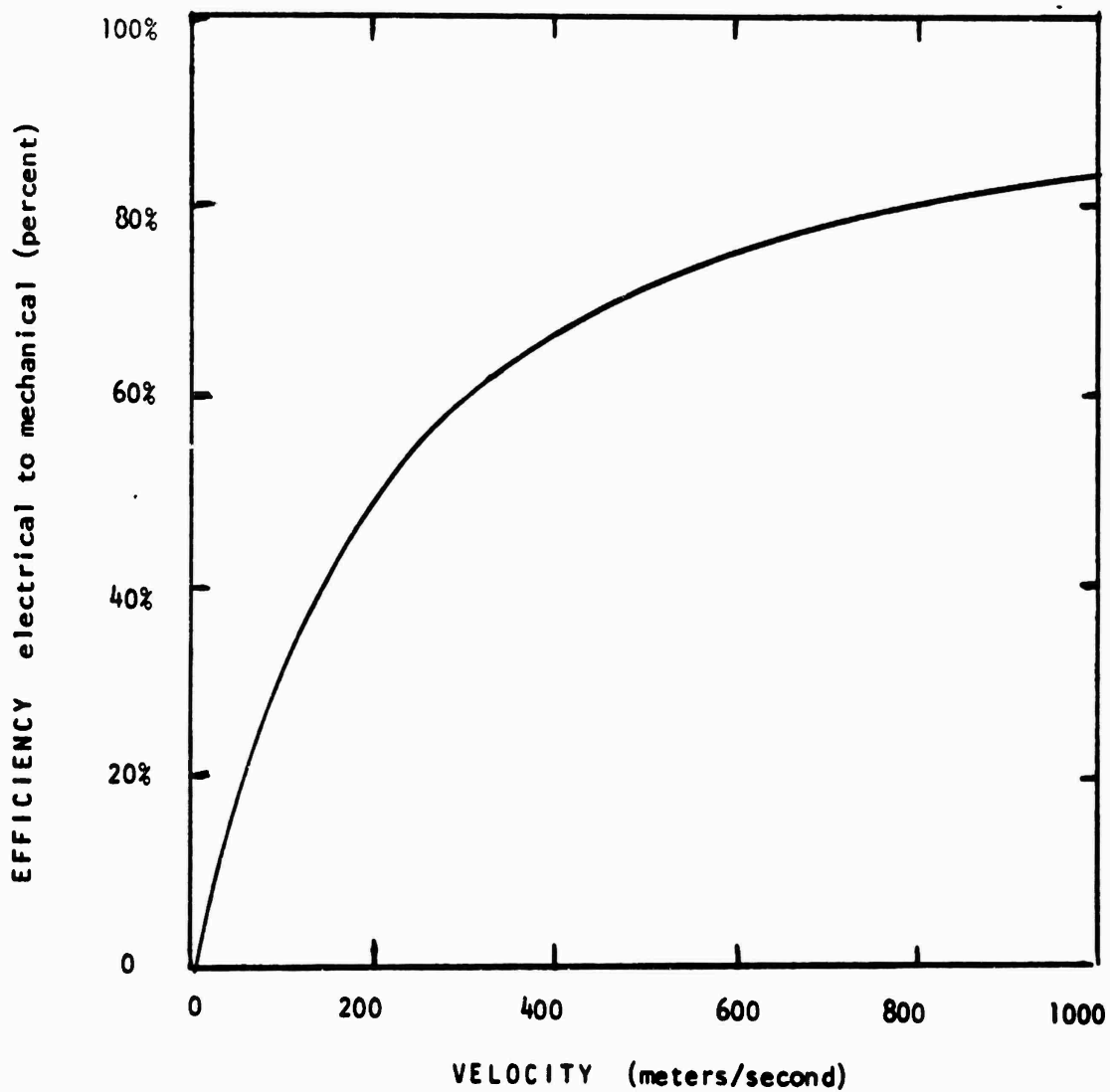


Fig. 13 Efficiency vs velocity, extrapolated from measurements on bench model helical railgun

THE GLIDER LAUNCHER

GENERAL CONFIGURATION

The launcher will consist of two twenty-foot external helical barrels supported side by side by their ends from Y-brackets attached to the ends of an aluminum I-beam. The glider will be accelerated between these twin booms by twin sliders up to the 16 foot point; the sliders will then be stopped in the remaining four feet and returned to the breech end. The full-scale system will launch 50 pound gliders and a truck-mounted version is shown in Fig. 14 on the following page.

There are three comparable options for energy storage: an engine-driven homopolar generator followed by an energy transfer inductor, all operating at room temperature. A set of lead-acid batteries charged by an engine-driven generator and discharged over a period of at most 15 seconds into an energy transfer inductor cooled to liquid nitrogen temperature, which then discharges into the launcher. The third alternative is the use of electrolytic capacitors charged by an engine-driven generator and discharged directly in staggered banks into the launcher. A homopolar generator would probably be used in an actual system.

We have chosen the third alternative, partly because we acquired about 1600 beer can type electrolytic capacitors as government surplus. These cans are 3" diameter, $5\frac{5}{8}$ " long, weigh 2 pounds each, and are rated at 3100 microfarad, 300 V, or 140 joule each. This corresponds to 70 pounds/joule. Their raw volume (not allowing for packaging) amounts to $165 \text{ ft}^3/\text{MJ}$. A one megajoule electrolytic bank at 100% packing density would therefore occupy a cube 5.5 ft on a side.

Launching a 23 kg (50 lb) glider to 88 m/s (200 mph) requires 0.1 MJ of kinetic energy. Assuming 50% efficiency, the task would require an electrolytic bank only about the size of the full-length tool-box on a utility truck (8'x3'x1.5').

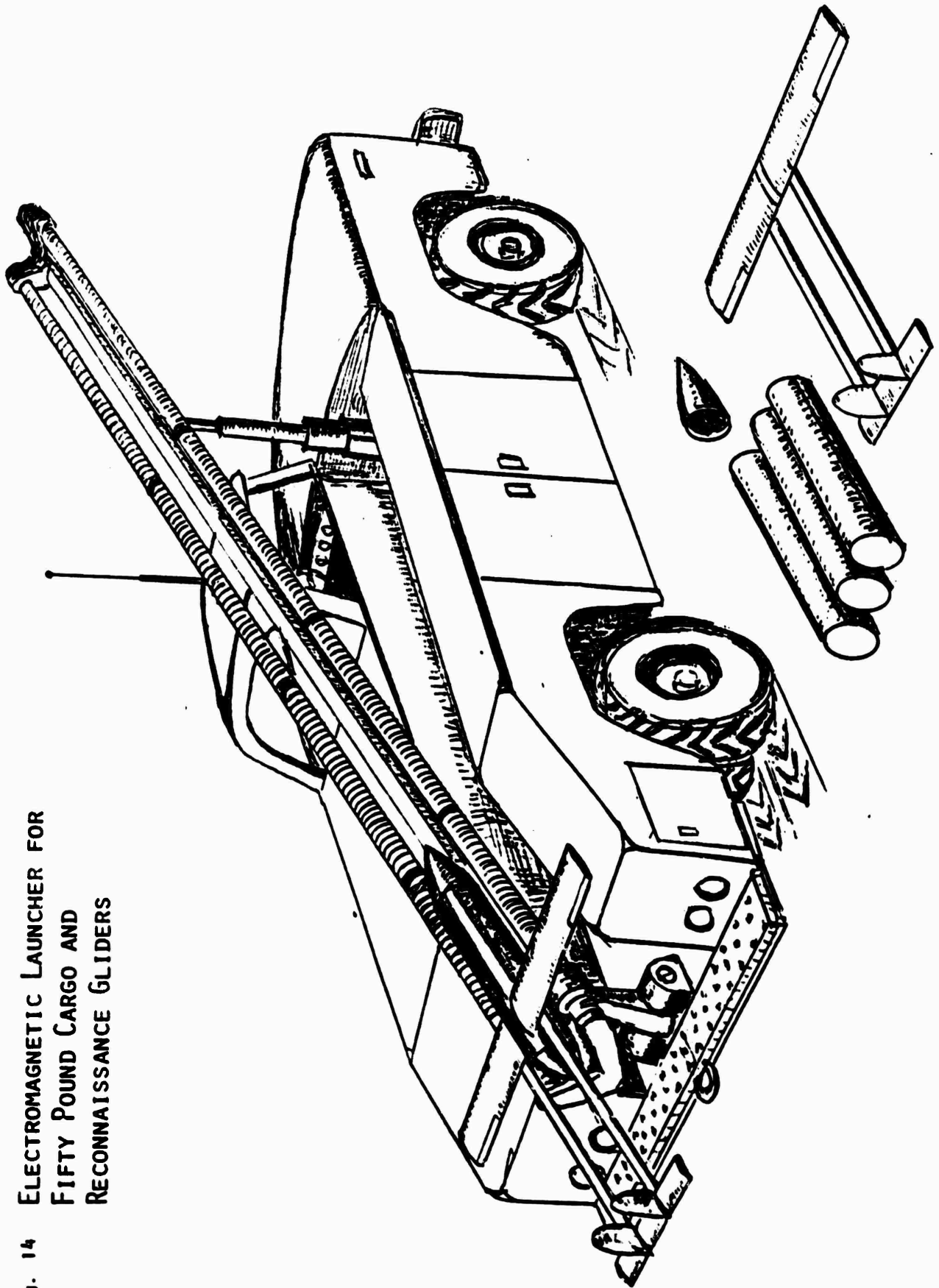


Fig. 14 ELECTROMAGNETIC LAUNCHER FOR
FIFTY POUND CARGO AND
RECONNAISSANCE GLIDERS

MECHANICAL DESIGN

The helical barrels will be fabricated in five foot sections using four inch i.d. transite water pipe, a readily available material of high stiffness, good thermal resistance, and low cost. The transite sections will be wrapped with epoxy and fiberglass cloth and terminated in brass connecting ferrules, then turned to an accurate o.d. Square copper wire, 0.1 x 0.135 inch, cotton insulated, will be wound edge-wise around the cylindrical fiberglass surface and then turned to within $\pm .002$ " of a cylindrical surface slightly more than 5" o.d.

Four helical sections will then be placed over a stainless steel tube with their connecting ferrules meshed, and compressed by means of jacking flanges so as to place the stainless steel core tube in tension. The fourth helical section will be only 48 inches long, the first three making up the remaining 16 feet. The last section will be wound in the opposite sense so as to generate a decelerating force.

The two booms will be supported at their ends, side by side, by Y-shaped brackets riveted to an aluminum I-beam located below the helical booms. The I-beam will also support the two current feed rails from which the two sliders will derive their current.

The cost of each five foot helical section tube made of transite with a fiberglass coating is about \$40, as compared to \$800 if a fiberglass composite tube such as G-10 were used instead. It is likely that a similar structure will prove the most expedient in production launchers as well.

ELECTRICAL DESIGN

The sliders will differ from those shown in Figs. 6 and 7 in that they will have two coil sections with two brush sections between them instead of the other way around. The helical barrel will thus have only one active section at the center of the slider, instead of two active sections. A detailed optimization analysis shows this configuration to be more expedient. The two active bucket coils will be connected in parallel; it would have been difficult to connect the helical sections in parallel.

The nominal performance parameters are as follows:

acceleration	100 gee	peak power	1 MW
mass	10 kg	kinetic energy	50 kJ
force	9.8 kN	launch duration	0.1 sec
velocity	100 m/s		
length	5.1 m = 16.7 ft		

The electrical-to-mechanical energy conversion efficiency is governed by the effective mutual inductance gradient dM/dx , and by the choice of conductor cross section, two related parameters. Once the conductor cross section has been chosen, the number of turns only affects the impedance match.

Having decided to derive the launch energy from electrolytic capacitors rated at 300 V, we design for a maximum back-voltage (kinetic emf, not including resistance drop) of 200 volts. This establishes the required peak current as 5 kA, allowing for 100 volts of resistive drop at peak velocity.

Thrust is given by: $F = N_b N_d \frac{dM}{dx} I^2 = b I^2$, where:

N represents the number of active bucket and drive coil turns,

dM/dx is the mutual inductance gradient in henries/meter

I is the series bucket and drive coil current, and

b defines a performance coefficient having the dimensions of henry/meter.

The energy conversion efficiency is now given by

$$\eta = \frac{b v}{b v + R}, \quad \text{where}$$

R is the total system resistance,

v is the instantaneous velocity, and

b is the coefficient defined above.

The efficiency clearly increases with velocity, asymptotically approaching unity. This is a general property of any dc-operated accelerator.

To achieve reasonable efficiency, the total system resistance must be kept below 20 milli-ohm. This is not a trivial accomplishment if the number of active turns is to be kept reasonably high with good inductive coupling.

On the basis of experience gained with the 40 inch test section, we select the configuration shown at right: the helix is made by edge-winding cotton-insulated rectangular copper wire, 0.1 x 0.135 inch, around an epoxy-fiberglass coated, 4 inch i.d. transite (asbestos) tube.

The helix has 15 active turns in an active length of 1.5 inch.

This active helix section will be connected in series with two bucket coil sections in parallel flanking the active helical section. The circuit is shown in Fig. 16 at right.

If we used one bucket coil flanked by two active drive coil sections, as in the test helix, the drive coil sections would have to be in parallel for topological reasons. Using two

bucket coils flanking a single drive coil section permits better coupling since the average coil-to-coil distance is smaller, in view of the fact that the bucket coils have more build than the single-layer helix. There is no penalty in resistance, and the added advantage that only a single brush set is required instead of two. It therefore emerges as an inevitable decision to use a single active section of the helix, flanked by two bucket coils with their turns located to optimize the mutual inductance gradient.

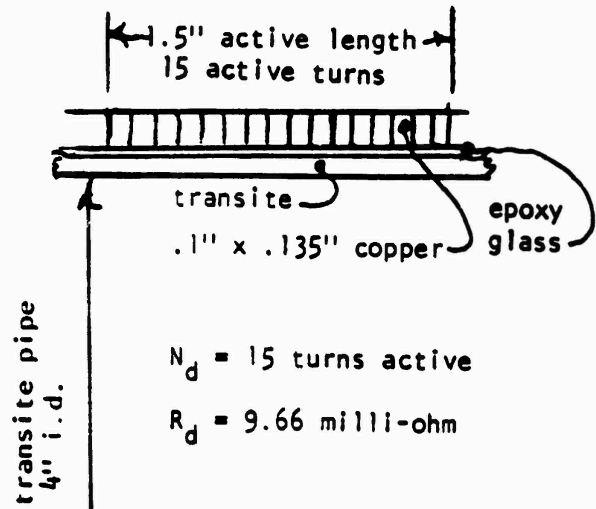


Fig. 15

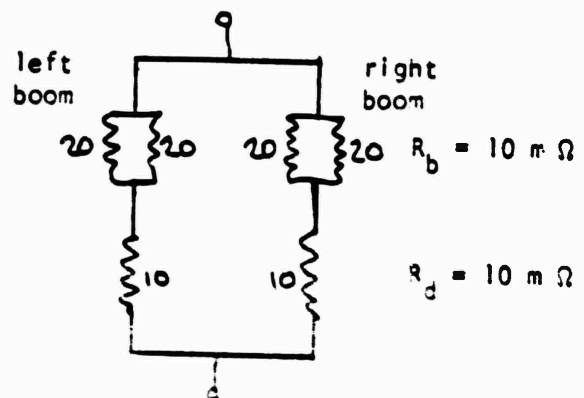


Fig. 16

For optimum efficiency, the bucket coil resistance should be about equal to the drive coil resistance. On the basis of experience with the test helix, we select 22 turns of 0.1 inch square copper wire, co-wound in two parallel starts (i.e., double wire winding of 22 turns, the two wires in parallel). The resistance is 10.18 milli-ohm. The total winding mass of the bucket is 887 grams. This includes two windings of 22 turns each with an i.d. of 4.4 inch, and the resistance corresponds to both windings in parallel. The circuit diagram of Fig. 16 shows the two buckets for the two side-by-side booms, each with two parallel windings.

Current density is 40 kA/cm^2 , temperature rise is 25°C during launch.

To determine the optimum distribution of bucket windings and predict the effectiveness of additional windings we have generated a map of the value of the mutual inductance gradient dM/dx in the vicinity of the active drive helix turns (on one side of the mid-plane), in 0.1 inch grid points. This map is shown on the next two pages, which can be joined at the arrows as indicated. The numbers on this grid are in units of micro-henry per meter, and are directly proportional to the thrust generated by a unit current filament at the locations of the grid, resulting from interaction of this current filament with the entire distributed current in the active drive helix turns. The numbers thus represent the priority of locating turns of the bucket coils which will flank the active drive helix section. The maximum thrust is generated at the ends of the drive helix (at the brush locations) (3.93), and the thrust falls off at about equal rates in the axial and radial directions from this maximum. It falls to one half in a distance of about half an inch. It is obviously important to locate the two bucket coils as close to the commutating brushes as possible, and to operate at the highest current density possible, subject to tolerable heating conditions. The performance (efficiency) of helical launchers will therefore be highly sensitive to the required repetition rate and to the use of cooling methods.

The final page of this section presents the result of a computer simulation in 0.005 second time increments of the launcher performance.

MAP OF MUTUAL INDUCTANCE GRADIENT NEAR ACTIVE DRIVE HELIX

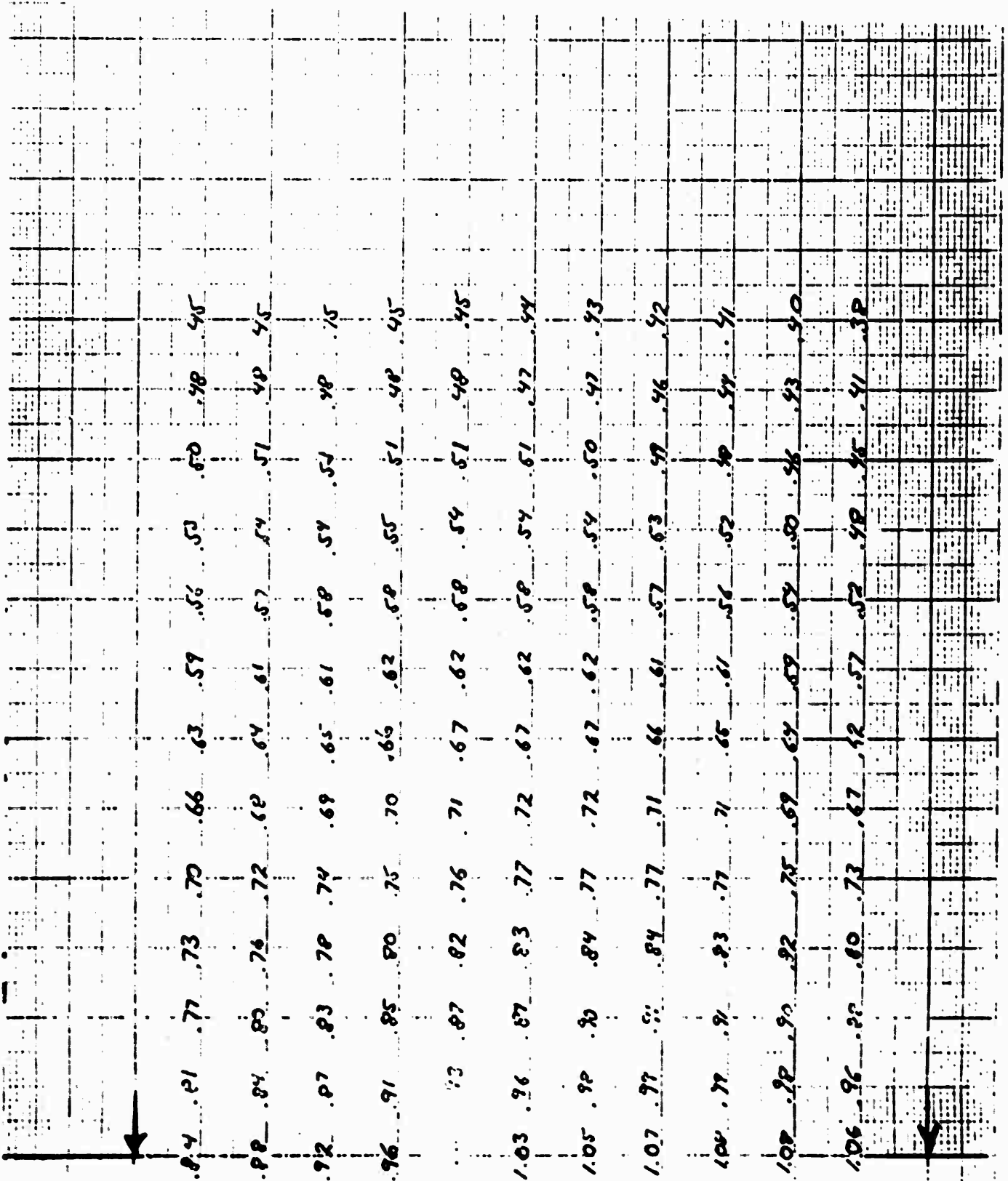
i.d. of drive helix: 4.0 inches; grid spacing: 0.1 inch

values given are $\frac{dM}{dx}$ in microhenry per meter

0	.14	.28	.41	.53	.65	.74	.82	.87	.94	.97	.98	.96	.94	.91	.88	.84
3	.16	.32	.47	.60	.73	.84	.92	.99	1.04	1.07	1.08	1.06	1.03	1.00	.97	.93
6	.18	.36	.53	.68	.82	.94	1.04	1.11	1.16	1.18	1.17	1.15	1.11	1.07	1.02	.97
9	.21	.41	.60	.78	.94	1.07	1.18	1.25	1.30	1.32	1.31	1.28	1.24	1.19	1.14	1.07
12	.23	.46	.69	.89	1.07	1.23	1.34	1.42	1.47	1.44	1.40	1.34	1.28	1.21	1.14	1.07
15	.27	.53	.78	1.02	1.23	1.41	1.54	1.62	1.65	1.64	1.57	1.45	1.36	1.27	1.19	1.03
18	.30	.60	.87	1.17	1.42	1.63	1.78	1.87	1.88	1.84	1.76	1.66	1.55	1.44	1.34	1.23
21	.34	.67	1.07	1.33	1.64	1.90	2.08	2.17	2.16	2.07	1.94	1.80	1.65	1.52	1.39	1.28
24	.37	.74	1.13	1.51	1.89	2.23	2.48	2.66	2.77	2.82	2.73	2.54	2.38	2.23	2.10	1.98
27	.40	.81	1.23	1.69	2.17	2.65	3.01	3.19	3.29	3.26	3.04	2.81	2.62	2.45	2.31	2.19
30	.41	.84	1.31	1.82	2.42	2.94	3.35	3.63	3.70	3.66	3.43	3.24	3.03	2.85	2.70	2.56



This page joins the preceding page at the arrows



edit.

set launch
edit.

run

Helical Rail Gun Launcher Simulation

this program performs a step by step iteration
give the requested parameters to start execution
system resistance

? .01

system couplings

? 8e-4

projectile mass

? 10

VCAP = capacitor voltage

storage capacitor

VBEMF = back-emf generated by moving bucket

? 3

system inductance

units are MKS

? .004

launcher length

? 5

time increment

? .005

initial voltage

? 350

time	x	vel	acc	current	vcap	vbemf
0.005	0.00	0.1	15.3	437	350	0
0.010	0.00	0.4	60.4	869	349	0
0.015	0.00	1.0	133.9	1294	347	1
0.020	0.01	2.2	233.8	1709	344	3
0.025	0.03	4.0	357.7	2115	341	7
0.030	0.05	6.5	502.4	2506	337	13
0.035	0.10	9.8	663.5	2880	333	23
0.040	0.16	14.0	835.4	3231	328	36
0.045	0.24	19.1	1011.2	3555	322	54
0.050	0.35	25.0	1183.0	3846	316	77
0.055	0.49	31.7	1342.3	4096	309	104
0.060	0.67	39.1	1480.3	4302	302	135
0.065	0.88	47.0	1589.4	4457	295	168
0.070	1.14	55.4	1663.9	4561	287	202
0.075	1.44	63.9	1700.4	4610	280	236
0.080	1.78	72.4	1698.6	4608	272	267
0.085	2.16	80.7	1661.3	4557	264	294
0.090	2.58	88.6	1593.4	4463	257	316
0.095	3.04	96.1	1501.8	4333	250	333
0.100	3.54	103.1	1393.7	4174	242	344
0.105	4.07	109.5	1276.5	3994	236	350
0.110	4.64	115.3	1156.3	3802	229	351
0.115	5.23	120.5	1038.2	3602	223	347

edit.

THE GLIDER

GENERAL OBJECTIVES

The glider is intended to reach maximum altitude ballistically, say 2,000 ft with a launch velocity of 200 mph, and then execute a controlled glide to a guided landing with a range of several miles. It is to serve for the delivery of cargo over inaccessible terrain, and as an expendable reconnaissance vehicle. It should be launchable from a truck at a repetition rate of several seconds. The cargo container and attachable airfoil assembly should be capable of compact, nested storage and instantaneous interconnection. The parts should be inexpensive and require no critical dimensions or adjustments, the flight being controlled instead by a reasonably smart on-board electronic controller responsive to ground commands from the launch site and from the landing site. A reasonable choice of size was considered to be 50 pounds gross weight.

It was originally intended to build a half-size, one-eighth weight model. However, the launcher does not scale down readily for electrical reasons, and energy was no problem. It was therefore decided to build a model of about half-weight and 79 percent size, or perhaps even full size. If performance expectations materialize, it should be possible to upgrade a launcher of same size to twice the launch mass.

The design of the glider vehicle is very important because usefulness of the entire electromagnetic launcher concept depends on it, and because it represents a design task which, to our knowledge, has never been tackled previously.

This part of the project was directed by Professor Rene Miller, and performed by two persons: Michael Paluszek, a recent MS graduate of the Department of Aeronautics and Astronautics did a trajectory analysis, and Marc Zeitlin, a graduate student in the Department, designed and started constructing the actual glider.

Both of their reports are included in their entirety. Other persons wishing to examine the problem will find all of the details very useful.

TRAJECTORY ANALYSIS (MICHAEL PALUSZEK)

1. Introduction

The purpose of this phase of the program was to determine the vehicle and launch configuration that would produce the maximum range for a given initial velocity at the exit of the electromagnetic accelerator. The glider characteristics available for modification were the wing aspect ratio (AR) and the wing loading. Given the launch velocity, the only launch parameter that could be varied was the launch angle, although the glider angle of attack was assumed to be controllable (if desired) during flight.

The limits for allowable aspect ratios and wing loadings were calculated by the glider design group, as were all the other vehicle parameters. Maximum launch weight and velocity were given by the accelerator group. Table 1.1 summarizes the relevant information.

Parameter	Value (or range)
C_{Dp}	.03
m	23kg
$C_{L\alpha}$	2π
e	.95
s	$.2m^2 \sim .65m^2$
AR	6 to 13
V_i	88m/sec

Table 1.1 Glider Data

The basic procedure was to numerically integrate the equations of motion to obtain the flight path, and maximum range, varying AR, γ and m/s in a heuristic fashion until the maximum range was achieved. No attempt was made to formally optimize the glider.

Since the philosophy was to design as simple a glider as possible the emphasis was on simple vehicle controls, unless a large gain in range, commensurate with the increase in complexity, could be obtained. The cases studied were the fixed angle of attack case and the ballistic launch case, where the wing produces lift only once the trajectory peak is reached.

This report is divided into three parts detailing the equation of motion, the numerical techniques and the results respectively. Copies of the computer code are included as an appendix.

2. The Equations of Motion

The equations of the motion were written in the flight path axis, as illustrated in Figure 2.1, by the balancing of forces. The equations are:

$$\begin{aligned} m \frac{du}{dt} &= -D - mg \sin \gamma \\ mv \frac{d\gamma}{dt} &= L - mg \cos \gamma \end{aligned} \tag{2.1}$$

where γ is the angle to the horizontal, m is the glider mass, v its velocity, g the acceleration of gravity, D the total drag and L the total lift.

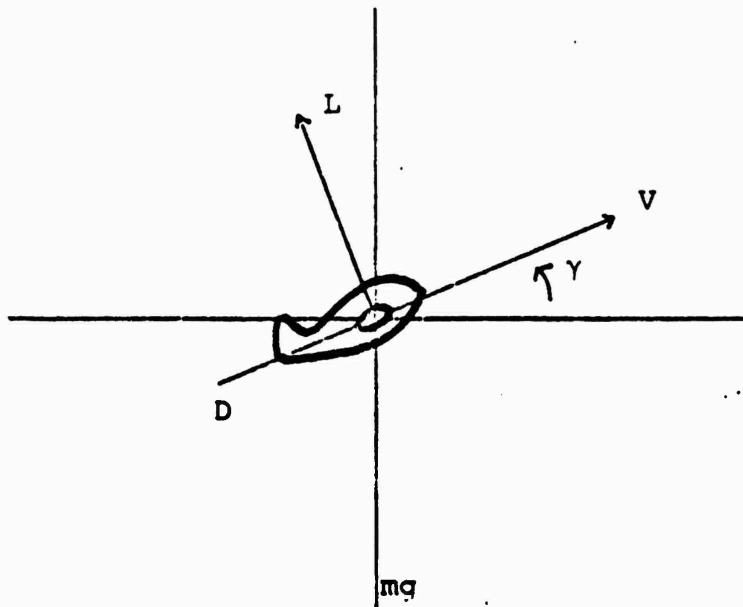
The drag is defined by the equation

$$D = \frac{1}{2} \rho v^2 A C_D \tag{2.2}$$

where ρ is the air density, C_D the drag coefficient and A is the drag reference area. The lift is similarly defined as

$$L = \frac{1}{2} \rho v^2 S C_L \tag{2.3}$$

where S is the lifting surface area and C_L is the lift coefficient.



2.1 Flight Path Axis

The drag coefficient is composed of two elements, one is the lift independent drag and the other the drag induced due to lift.

$$C_D = C_{D_p} + \frac{C_L^2}{\pi e AR} \quad (2.4)$$

The lift coefficient is derived from thin airfoil theory⁴ and is

$$C_L = \frac{C_{L_Y}}{1 + \frac{C_{L_Y}}{\pi AR}} \alpha \quad (2.5)$$

$$C_{L\alpha} = 2\pi$$

The air density is assumed to be an exponential function of altitude and is given by

$$\rho = 1.2 e^{-h/6341} \quad (2.6)$$

with ρ in kg/m^3

3. Numerical Methods

A fourth order Runge-Kutta method was used to integrate the equations numerically. The four equations of motion are arranged as follows

$$\begin{aligned}\frac{du}{dt} &= -D/m -g \sin \gamma \\ \frac{dy}{dt} &= \frac{L}{mv} -g/v \cos \gamma \\ \frac{dv}{dt} &= v \cos \gamma \\ \frac{dv}{dt} &= v \sin \gamma\end{aligned}\tag{3.1}$$

The right hand sides are functions of V , γ and y .

The algorithm used is an extension of the two first order equation case as given in Hildebrandt.² The error is on the order of $(\Delta t)^4$. For the trajectory analysis $\Delta t = 1$ sec and the algorithm was implemented on a PDP 11/10 using single precision arithmetic.

4. Results and Conclusions

4.1 Introduction

In order to establish a baseline vehicle a wide variety of vehicle configurations were simulated on the computer. The cases can be grouped into three general types; ballistic, fixed angle of attack and variable angle of attack. Maximum ranges and optimum launch angles were calculated for all the cases and the results used to choose a configuration for actual construction.

4.2 The Ballistic Vehicles

The simplest case was the ballistic projectile with no lifting surfaces. With a drag coefficient of $C_{D_p} = .03$ and a launch angle of 45° the range was 644m. With $C_{D_p} = .001$ this range increased to 804 m. Essentially, this is an artillery shell with no controls and the simplest structure, due to the absence of wings.

4.3 The Constant Angle of Attack

The constant angle of attack configuration was the next simplest design with the wing preset at a given angle of attack and no active controls. The improvement in range over the ballistic case (with equal C_{D_p}) was 113 m for an aspect ratio of 6 and 192.4 m for an aspect ratio of 13. The reason for this relatively poor performance is the need to maintain stable flight over a wide velocity range and during the very steep climb. Unless the angle of attack at launch is kept well below the angle for optimum L/D the glider will loop. Besides the short range, this configuration has very high landing velocities unless provisions are made for a flare at landing.

4.4 The Variable Angle of Attack

Since it is difficult to obtain good range in a vehicle designed for a high velocity boost and for gliding, the obvious step was to separate the two flight conditions and optimize for each with some simple control system providing the transition. The result was a combination of the previous two cases with a ballistic launch and lifting glide. The wings are deployed on launch but are set to provide no lift. At the peak of the trajectory an actuator sets the wings at the angle of attack for maximum L/D as determined by the relationship.

$$\alpha_{\max} L/D = \sqrt{\frac{\pi eAR C_{Dp}}{C_{L\alpha}^2}} \quad (4.4.1)$$

If the air density does not vary significantly this will produce the maximum glide distance. The glide distance for the constant angle of attack is³

$$\Delta x = \frac{C_L}{C_D} \left(h_i - h_f + \frac{v_i^2 - v_f^2}{2g} \right) \quad (4.4.2)$$

where h is the altitude and v the velocity. Since ρ varies less than 5% in all the analyzed trajectories, this relationship is good for the cases of interest.

The free parameters for this analysis were taken to be γ_1 , the launch angle, AR and s, the wing surface area. γ_1 determines the peak height of the trajectory and the cross-range during the ballistic flight while the latter two, along with the trajectory peak, determine the gliding range.

The procedure was to find an optimum combination of γ_1 and s for every given AR, then to compare the optimums at each AR with each other.

Figures 4.1 and 4.2 give maximum ranges vs. wingloading for AR = 6 and 13, respectively. Each maximum is achieved at a given optimum launch angle which is given in figures 4.3 and 4.4. For each AR there is a wingloading that gives maximum total crossrange. The peak range is achieved with wingloadings on the order of 9.5 to 10 lbs/ft². The roll off in range after the peak is due to the increase in drag during ballistic flight which reduces the trajectory peak and the ballistic crossrange.

Figure 4.5 gives the maximum ranges versus AR for AR ranging from 6 to 20. The variation with AR is nearly linear. Theory predicts that for gliding flight at optimum L/D the range should vary as \sqrt{AR} . This proves to be the case when the ballistic crossrange is subtracted from the total range and the increase in peak trajectory height is accounted for.

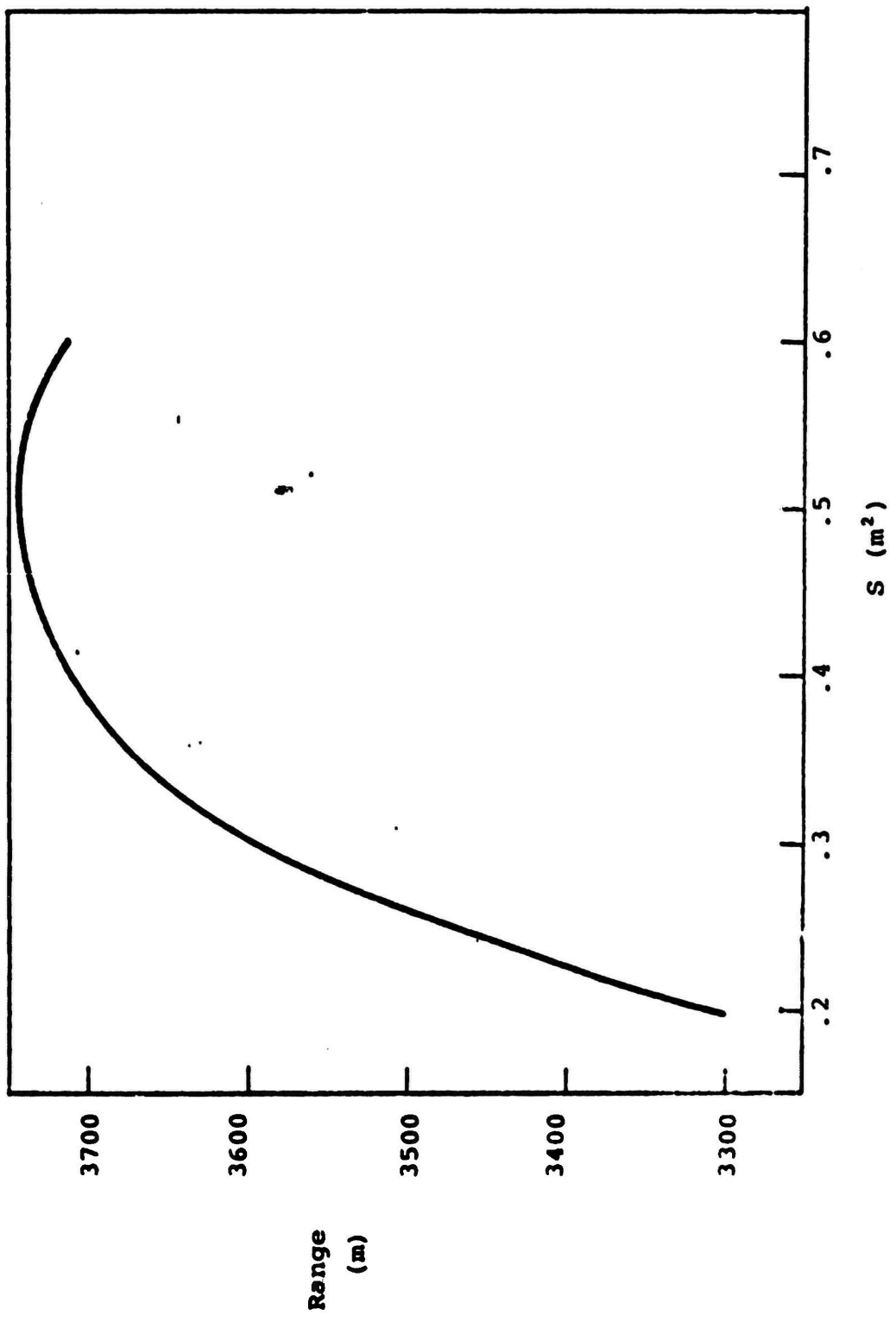


Figure 4.1 Maximum Range vs. Wingloading
AR = 6

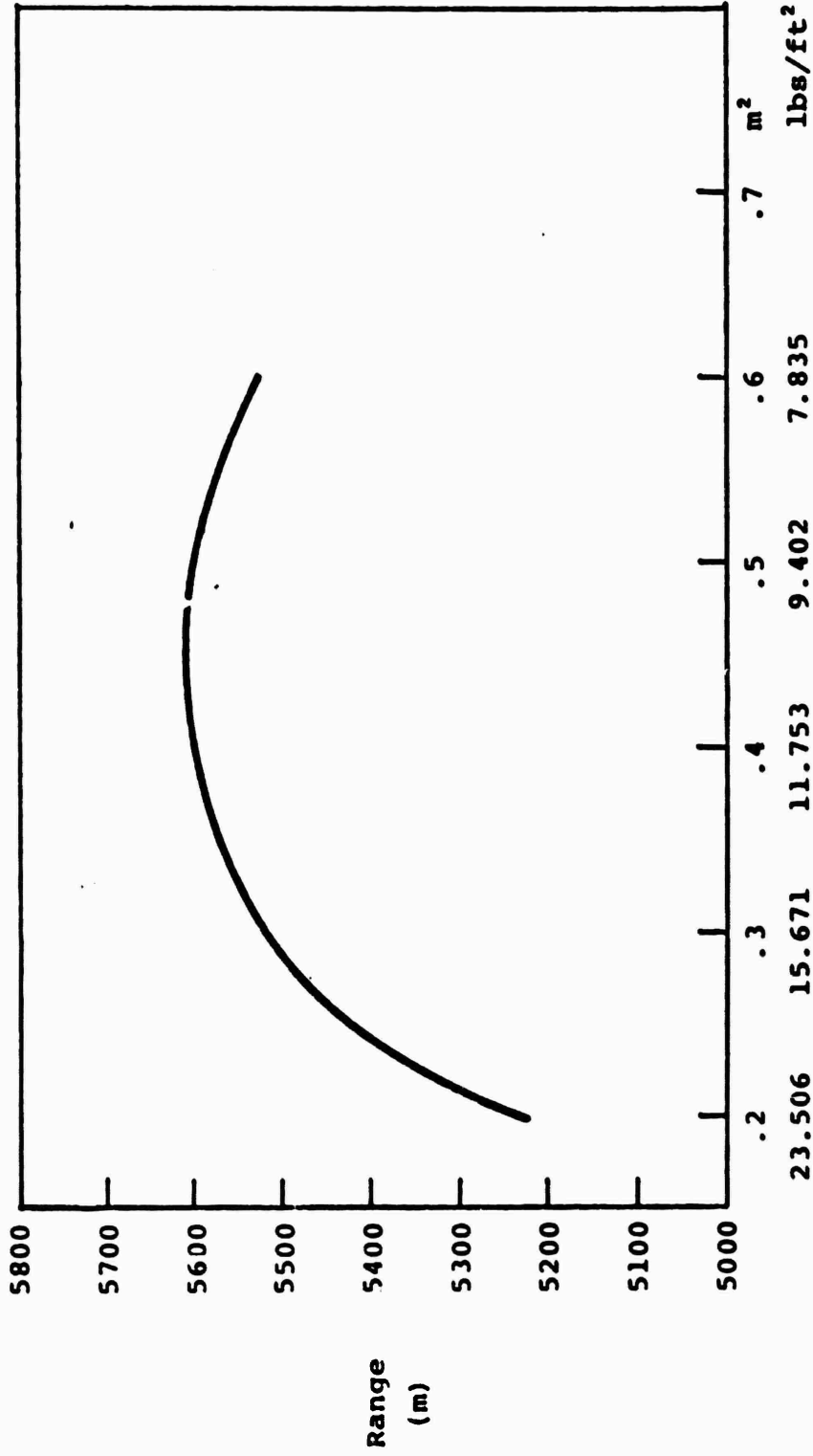


Figure 4.2 Maximum Range vs. Wingloading
for Ballistic Launch

AR = 13

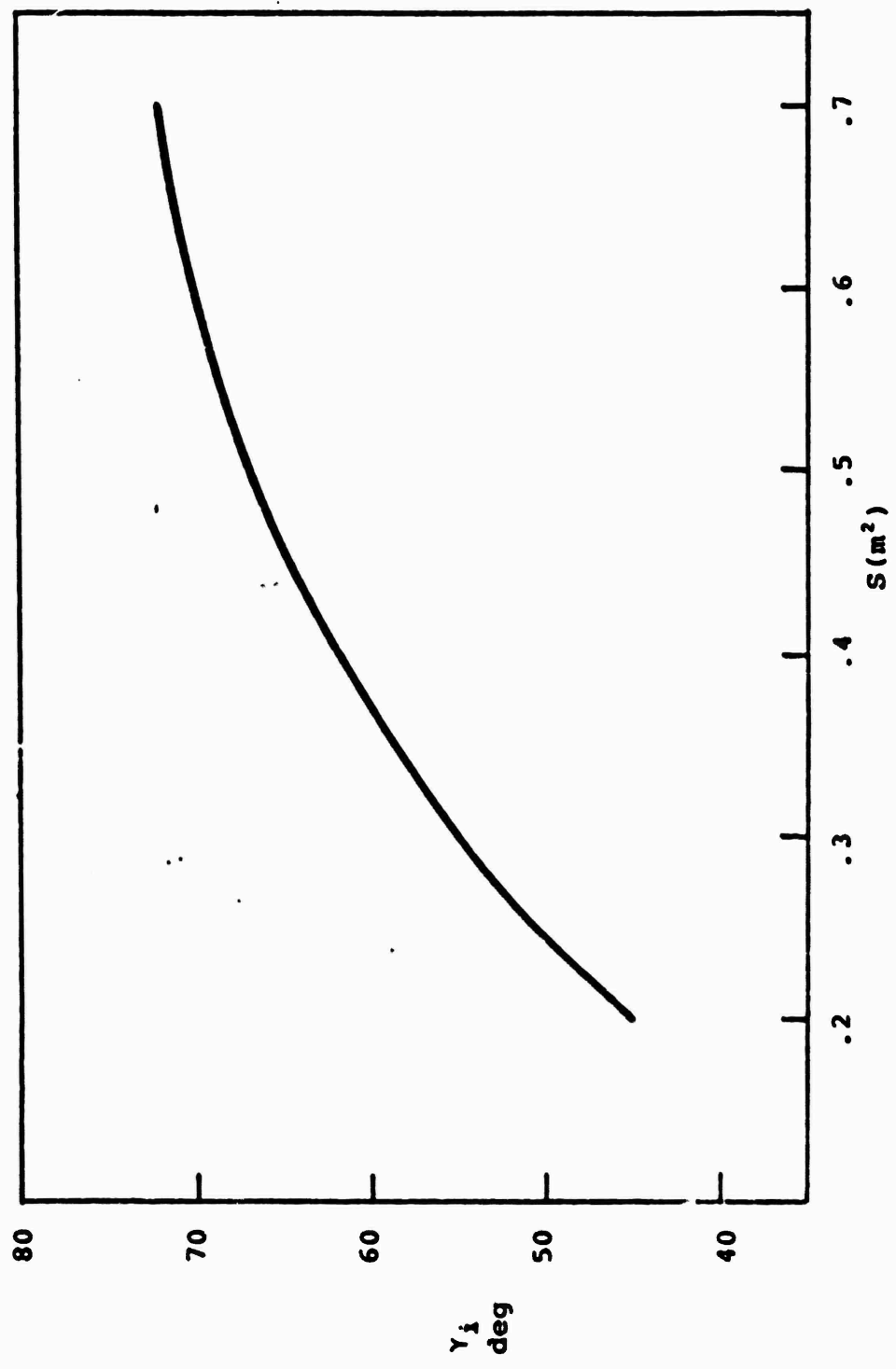


Figure 4.3 Optimum launch angle vs. wing area
AR = 6

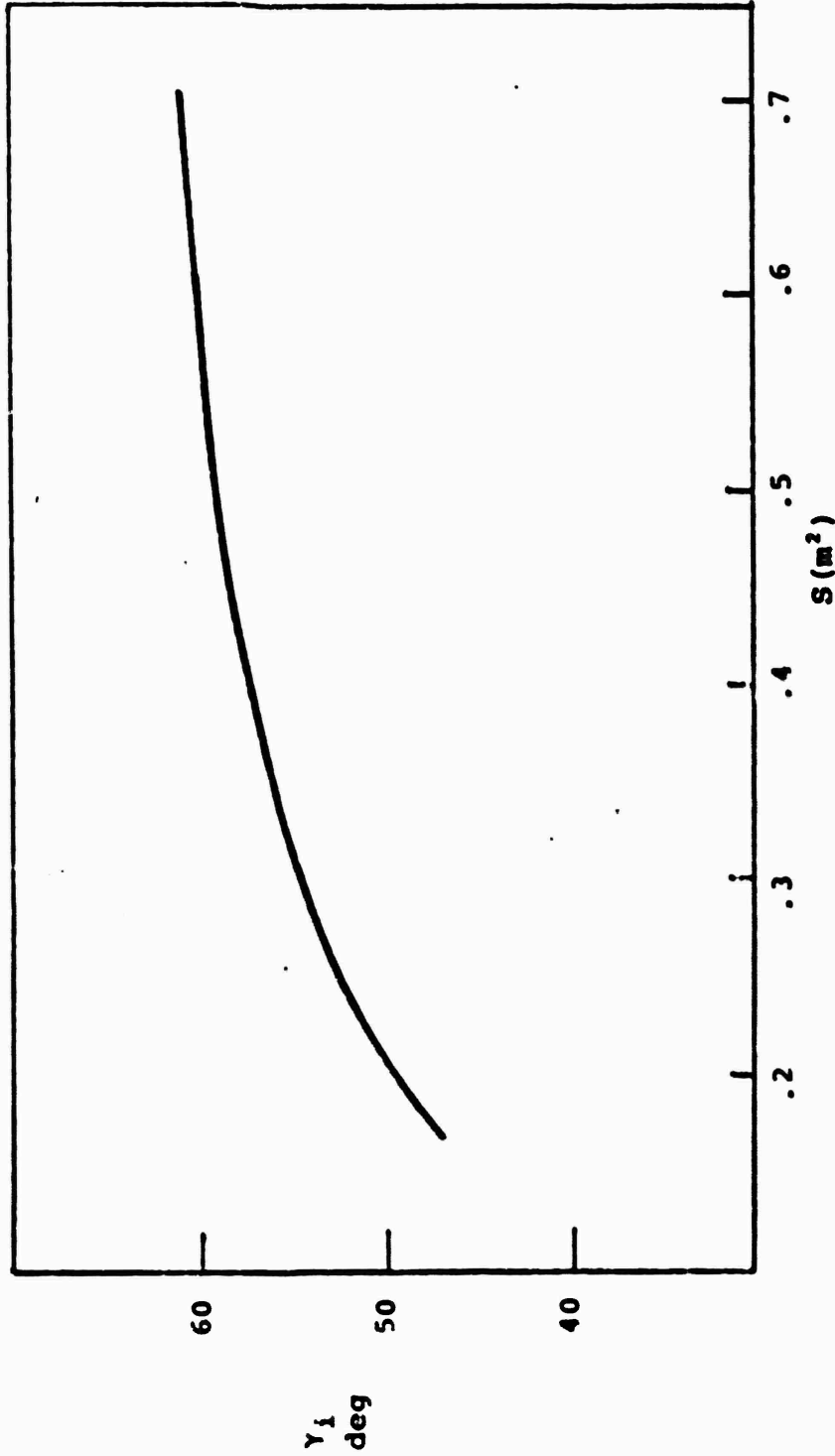


Figure 4.4 Optimum launch angle vs. wing area
R - 13

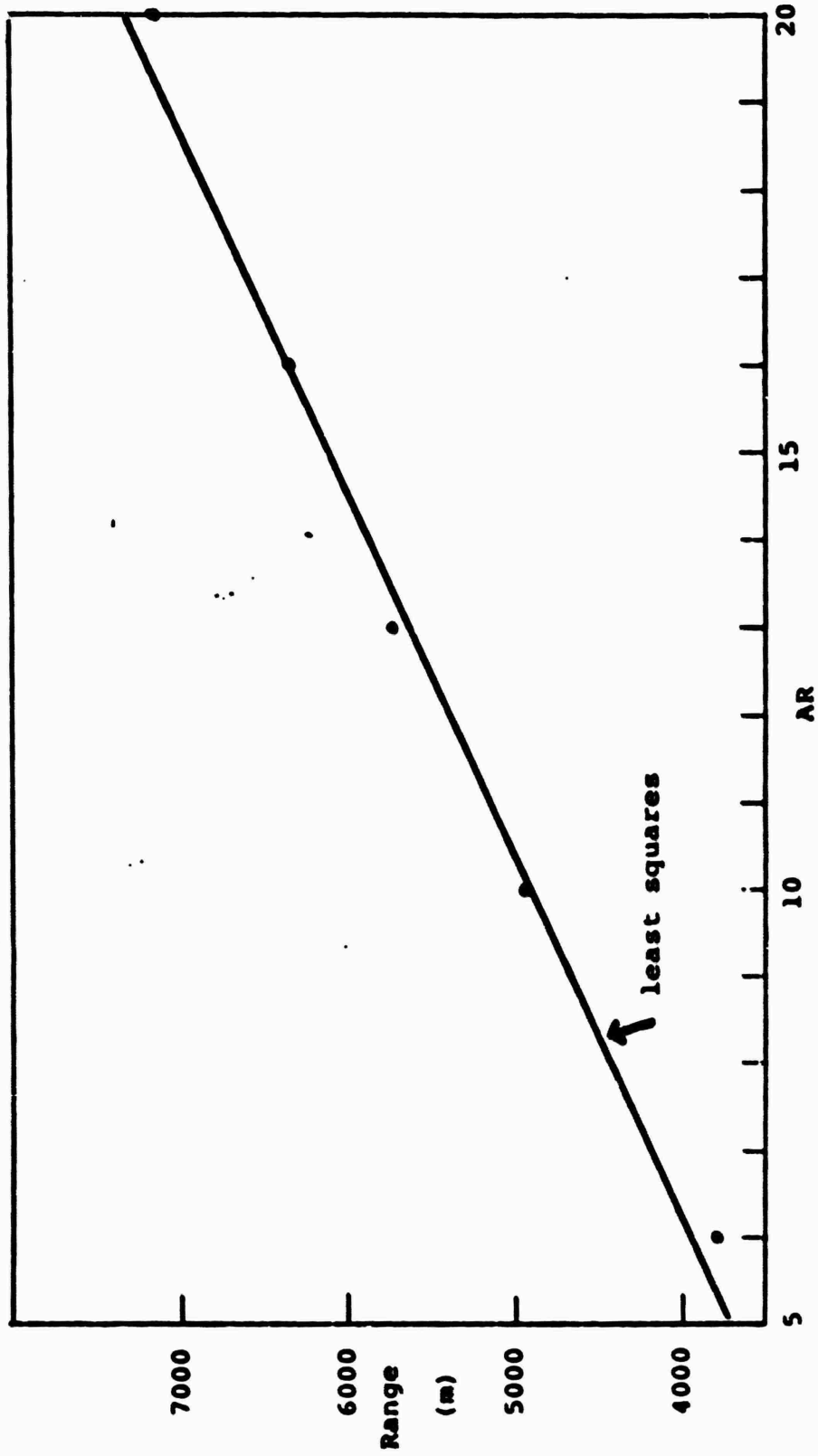


Fig. 4.5 Maximum range vs. AR

4.6 Conclusions

Table 4.1 gives a summary of the data for all the cases examined. Figure 4.6 shows representative trajectories for the ballistic, constant angle of attack and variable angle of attack cases.

The best configuration is the variable angle of attack design with as large an aspect ratio as possible. The only limit to aspect ratio would be due to structural considerations. The wing loading should lie between 9.5 and 10 lbs/ft² and launch angles will be in excess of 70°. Any limits due to diminishing returns on AR will only occur for very large AR when the AR law begins to reassert itself as γ_1 reaches a limit. A further limit may be that the high angles of attack needed for optimum L/D at large AR may be difficult to realize.

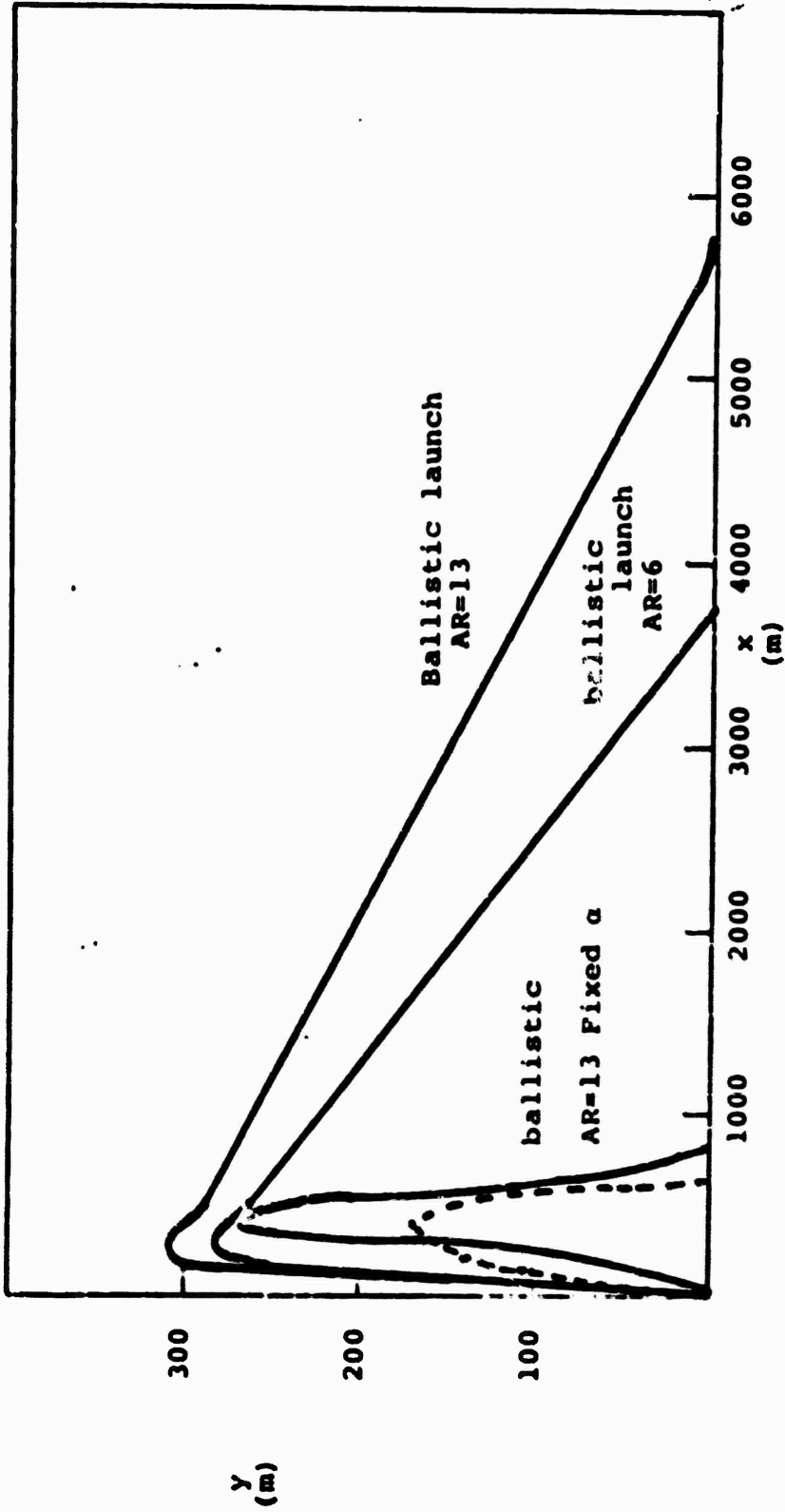


Figure 4.6 Trajectories for Ballistic with $C_D = .03$, Fixed α AR-13;
Ballistic Launch: AR = 6; AR = P 13

Table 4.1 Summary of Results

Case	γ_i	S	α	max range
	Deg	m ²	Deg	m
ballistic ($C_{Dp} = .001$)	45	0	0	808
ballistic ($C_{Dp} = .03$)	45	0	0	644
fixed α				
AR = 6	0	.2	8.9	757
AR 13	0	.3	5	836
variable α , ballistic launch				
AR = 6	65	.50	8.9	3744
10	70	.45	10.5	4940
13	70	.45	11.4	5715
16	70	.50	12.3	6362
20	70	.50	13.4	7155

References

1. Larrabee, E.E., Flying by Computer, 16.15 course notes, MIT, Spring 1978.
2. Hildebrandt, F.B., Introduction to Numerical Analysis, McGraw-Hill, NY 1956, p.237.
3. Miele, A., Flight Mechanics, 1962 Addison-Wesley, Reading, MA.
4. Kuethe, A.M., and Chow, C., Foundations of Aerodynamics, Wiley, NY. 1976, p. 155.

APPENDIX: The Computer Program

```

TYPE DL0:TRJ.FOR
C THIS PROGRAM USES THE RUNGE KUTTA INTEGRATION
C TECHNIQUE TO SOLVE THE LONGITUDINAL EQUATIONS
C OF MOTION FOR AN ELECTROMAGNETICALLY LAUNCHED
C GLIDER
      REAL L,M,LOVERD
      COMMON/AEROPR/CDP,CLALPH,S,AR,E,A,M,ALPHA,AUNDER
10     FORMAT(40H INPUT CDP,CLALPHA,AR,E,M FOR THE GLIDER)
11     FORMAT(40H CDP IS THE LIFT INDEPENDENT DRAG COEFF.
      1/26H CLALPH IS THE LIFT COEFF.
      2/22H S IS THE SURFACE AREA
      3/28H AR IS THE WING ASPECT RATIO
      4/19H E IS THE AERO. EFF
      5/14H M IS THE MASS
      6/22H A IS THE FRONTAL AREA)
      TYPE 11
      TYPE 10
      PI=3.14159
16     FORMAT(5F12.4)
15     FORMAT(4F12.4)
      READ(5,16) CDP,CLALPH,AR,E,M
      CLALPH=CLALPH/(1.+CLALPH/(PI*AR))
20     FORMAT(26H INPUT DT IN SECS,Y0,X0,U0)
      TYPE 20
      READ(5,15) DT,YI,XI,VI
151    FORMAT(23H INPUT DEPLOYMENT GAMMA)
      TYPE 151
      READ(5,118) GAMMAD
      GO TO 150
147    FORMAT(29H INPUT ANGLE OF ATTACK IN DEG)
150    TYPE 147
      READ(5,118) ALPHIN
      ALPHIN=ALPHIN*3.14159/180.
      IF(ALPHIN .GE. 0.) GO TO 167
      ALPHIN=SQRT(PI*E*AR*CDP/CLALPH**2.)
      IF(ALPHIN .GT. .2792) ALPHIN=.2792
118    FORMAT(F12.4)
155    FORMAT(17H ANGLE OF ATTACK=,F8.3,5H DEG.)
      TYPE 155, ALPHIN*180./PI
160    FORMAT(6F12.4)
157    FORMAT(52H INPUT LIMITS,SI,SF,DELTAS,GAMMAI
      1,GAMMAF,DELTA GAMMA)
167    TYPE 157
      READ(5,160) SI,SF,DELS,GI,GF,DELG
      GI=PI*GI/180.
      GF=PI*GF/180.

```

```

      DELG=PI*DELG/180.
      S=SI-DELS
175     S=S+DELS
      A=S
      GAMI=GI-DELG
      IF(S .GT. SF+DELS/2.) GO TO 1000
170     FORMAT(15H WING LOADING =,F8.3,8H LBS/FT2)
      TYPE 170,M/S*.2044
185     GAMI=GAMI+DELG
      IF(GAMI .GT. GF+DELG/2.) GO TO 175
      X=XI
      Y=YI
      V=VI
      GAM=GAMI
      IA=0
C     THESE ARE THE RUNGE KUTTA SUBROUTINE CALLS
C     X IS THE HORIZONTAL DISTANCE, Y THE ALTITUDE
C     AND GAM IS GAMMA THE FLIGHT PATH ANGLE
200     ALPHA=ANGLE(Y,GAM,ALPHIN,IA,GAMMAD)
210     UO=DT*F1(Y,U,GAM)
      GAMO=DT*F2(Y,U,GAM)
      XO=DT*F3(Y,U,GAM)
      YO=DT*F4(Y,U,GAM)
      U1=DT*F1(Y+.5*YO,U+.5*UO,GAM+.5*GAMO)
      GAM1=DT*F2(Y+.5*YO,U+.5*UO,GAM+.5*GAMO)
      X1=DT*F3(Y+.5*YO,U+.5*UO,GAM+.5*GAMO)
      Y1=DT*F4(Y+.5*YO,U+.5*UO,GAM+.5*GAMO)
      U2=DT*F1(Y+.5*Y1,U+.5*U1,GAM+.5*GAM1)
      GAM2=DT*F2(Y+.5*Y1,U+.5*U1,GAM+.5*GAM1)
      X2=DT*F3(Y+.5*Y1,U+.5*U1,GAM+.5*GAM1)
      Y2=DT*F4(Y+.5*Y1,U+.5*U1,GAM+.5*GAM1)
      U3=DT*F1(Y+Y2,U+U2,GAM+GAM2)
      GAM3=DT*F2(Y+Y2,U+U2,GAM+GAM2)
      X3=DT*F3(Y+Y2,U+U2,GAM+GAM2)
      Y3=DT*F4(Y+Y2,U+U2,GAM+GAM2)
      U=U+1./6.*(UO+2.*U1+2.*U2+U3)
      GAM=GAM+1./6.*(GAMO+2.*GAM1+2.*GAM2+GAM3)
      X=X+1./6.*(XO+2.*X1+2.*X2+X3)
      Y=Y+1./6.*(YO+2.*Y1+2.*Y2+Y3)
      IF(Y .GT. 0.1 .AND. V .GT. 1.) GO TO 200
      LOVERD=WLIFT(Y,U,S,CLALPH,ALPHA)/
      1DRAG(Y,U,CDP,CLALPH,A,ALPHA,AR,E,0.)
      TYPE 555,GAMI*180./PI,S,X,LOVERD,U,U*SIN(GAM)
555     FORMAT(15H GAMMA INITIAL=,F4.0,11H WING AREA

```

```

1=,F6.2,3H X=,F6.1,5H L/D=,F6.2,3H V=,F6.1,4H VY=,F6.1)
GO TO 185
1000  END
C  THESE ARE THE RIGHT SIDES OF THE DN/DX=
C  FOR N: V,GAM,X,Y
      FUNCTION F1(Y,V,GAM)
      REAL M
      COMMON/AEROPR/CDP,CLALPH,S,AR,E,A,M,ALPHA,AUNDER
      G=9.8
      D=DRAG(Y,V,CDP,CLALPH,A,ALPHA,AR,E,AUNDER)
      F1=-D/M-G*SIN(GAM)
      RETURN
      END
      FUNCTION F2(Y,V,GAM)
      REAL M,L
      COMMON/AEROPR/CDP,CLALPH,S,AR,E,A,M,ALPHA,AUNDER
      G=9.8
      L=WLIFT(Y,V,S,CLALPH,ALPHA)
      F2=L/M/V-G/V*COS(GAM)
      RETURN
      END
      FUNCTION F3(Y,V,GAM)
      F3=V*COS(GAM)
      RETURN
      END
      FUNCTION F4(Y,V,GAM)
      F4=V*SIN(GAM)
      RETURN
      END
C  THIS FUNCTION COMPUTES THE DRAG
      FUNCTION DRAG(Y,V,CDP,CLALPH,A,ALPHA,AR,E,AUNDER)
      RHO=DENS(Y)
      CD=CDP+CL(ALPHA,CLALPH,V,Y)**2/3.14159/E/AR
      DRAG=.5*RHO*V**2.*A*CD
      RETURN
      END
C  THIS FUNCTION COMPUTES THE LIFT
      FUNCTION WLIFT(Y,V,S,CLALPH,ALPHA)
      RHO=DENS(Y)
      WLIFT=.5*RHO*V**2.*S*CL(ALPHA,CLALPH,V,Y)
      RETURN
      END

```

```

-----
FUNCTION DENS(ALT)
DENS=1.2*EXP(-ALT/6341.)
IF(ALT .LT. .01) DENS=1.2
RETURN
END
C THIS FUNCTION COMPUTES THE LIFT COEFFICIENT
FUNCTION CL(ALPHA,CLALPH,V,Y)
REAL MACH
RHO=DENS(Y)
A=291.102*SQRT(RHO)
MACH=V/A
IF(MACH .LT. .98 .AND. MACH .GE. 0.) GO TO 20
TYPE 15,V,A,MACH
15  FORMAT(3H V=,F12.4,3H A=,F12.4,6H MACH=,F12.4)
STOP
20  COEFF=1./SQRT(1.-MACH**2)
CL=CLALPH*ALPHA*COEFF
RETURN
END

```

```

.TYPE DLO:ANGOFA.FOR
FUNCTION ANGLE(Y,GAM,ANGIN,IA,GAMMAD)
IF(IA .EQ. 1) GO TO 20
IF(GAM .LE. GAMMAD*3.14159/180.) GO TO 20
IA=0
ANGLE=0.
RETURN
20  ANGLE=ANGIN
IA=1
RETURN
END

```

INITIAL DESIGN (MARC ZEITLIN)

I. Introduction

The purpose of the initial phase of the design process was to arrive at a design for a glider that will be launched from an electromagnetic launcher. The full scale glider will have a gross weight of 22.7 kg. (50 lb.), and to have the same aerodynamic characteristics, the half-scale model will have a gross weight of 5.7 kg. (12.5 lb.). The glider should be as light as possible to allow a large payload and should have the maximum possible range. It should be very strong to withstand the launching forces, which will be a 100g (980 m/sec²) acceleration to a maximum velocity of 88 m/sec (200 m.p.h.). Knowing that the glider will need to be repaired after mishaps, an easily repairable model is also a necessity.

Since this is the first model to be launched by this method, an emphasis was placed on getting the concept to work, however well or poorly, and refining the capabilities in later models. In this light, tradeoffs were made in the payload and range capabilities to ensure strength, durability, repairability, and simplicity.

This report is divided into three parts, showing the Design Process, the Resultant Glider Design, and the Project Status.

II The Design Process

The first step in the design process (arbitrarily chosen as first) was to determine the aerodynamic characteristics of a glider with assumed structural characteristics. The

major characteristic examined was the glide ratio, a direct determinant of the range, as a function of wing geometry, specifically wing loading and wing aspect ratio. A graph of this is shown in figure 1.

The second step was to design a structure to fit the aerodynamic characteristics chosen while trying to minimize weight, and using a safety factor of two in the strength analysis. Many structural possibilities were examined and compared to obtain the required simplicity, strength, durability, and repairability.

Since the second step produces a structure different from the assumed one in part one, it is seen that steps one and two must be iterated through many times to obtain consistent aerodynamic and structural characteristics.

The third step involved examining the stability of the design. The stability was analyzed using methods found in reference 1. The stability criterion were; stable in both short period and phugoid longitudinal oscillations, and stable in rolling, dutch roll, and spiral lateral oscillations.

To obtain a glider consistent with all the stability criteria, steps one and two must be repeated, and then all three steps iterated many times to achieve consistent structural, aerodynamic, and stability characteristics.

The results of these iterations, the half-scale model glider design, will be presented in the next section.

III. The Resultant Design

A) Overview:

A sketch of the half-scale model glider is shown in figure two, and the physical characteristics are given in Appendix A. This model is a high-mid-wing, pod and twin-boom, twin rudder configuration. This is a very modular design and allows for easy construction and repair, as the model separates easily into three main sections; wing, fuselage pod, and tail and booms.

The large, high aspect ratio wings provide a respectable glide ratio of 20 when coupled with the low drag of the streamlined fuselage and tail. The model has a payload of over 50% of gross weight. The strength of the craft has not been jeopardized by obtaining these performance figures, and it is projected that better performance will be obtained in later models.

B) Structure:

The wing is a styrafoam core covered with two layers of epoxy impregnated graphite cloth. This imparts a very high strength- high stiffness quality to the wing while retaining very low weight. Since the limiting factor for the

wing skin was the torsional stiffness, graphite was chosen over either fiberglass or Kevlar, for its stiffness-to-weight ratio.

The fuselage pod is a standard spruce stringer plywood bulkhead and skin construction. This was chosen for ease of construction and repair. The control system mounts in the front of the pod while the payload sits beneath the wing. The wing and booms screw into the two rear bulkheads.

The booms are thin wall aluminum tubing, chosen for availability and price, along with ease of construction and repair. The stiffness of the booms is important, and the aluminum provides this while still being lightweight.

The tail is balsa sheet, chosen for lightness.

C) Controls:

The stability analysis has indicated that a two control surface system, consisting of elevator and rudder, is sufficient, and that is what is provided for in the half-scale model. The control surfaces are to be actuated by a standard model airplane radio control system manufactured by Kraft and consisting of a transmitter, receiver, battery pack, and two servos. All but the transmitter (human operated) are

carried in the glider.

The trajectory analysis, carried out in Michaël Paluczek's report, shows a trajectory consisting of a ballistic launch followed by a controlled glide at a constant glide speed. The glider will be trimmed (using the control system) for zero lift for the ballistic portion of the flight, and at the apex of the trajectory, when the vehicle has slowed to gliding speed, the controls will trim the aircraft for maximum glide ratio flight.

The human operator is included in the first model design to cope with any unforeseen control problems.

D) Stability:

The glider as shown is stable in all oscillatory modes mentioned at both launch velocity and glide velocity, along with all the velocities in between. The glider has natural frequencies and time constants for all oscillations that quickly return the glider to normal gliding flight.

The stability derivatives and oscillation modes are given in Appendix B.

IV. Project Status (6/3/80)

At this point in the project, parts and assembly

drawings have been drawn for each part. All parts have been procured except the styrafoam, graphite, and epoxy. The foam will be bought from Sterling Ind. in Waltham, the graphite cloth from Fiberite, and the epoxy from the Magnet Labs.

Two gliders are under construction, and two sets of tail surfaces are completed. Two sets of tail booms are 75% complete, and two fuselage pods are 50% complete. After I return from vacation in August, approximately two weeks will be necessary to completely finish both gliders. Projected first flight will be during the last week of August, with an electromagnetic launch occurring sometime in September.

Figure 1

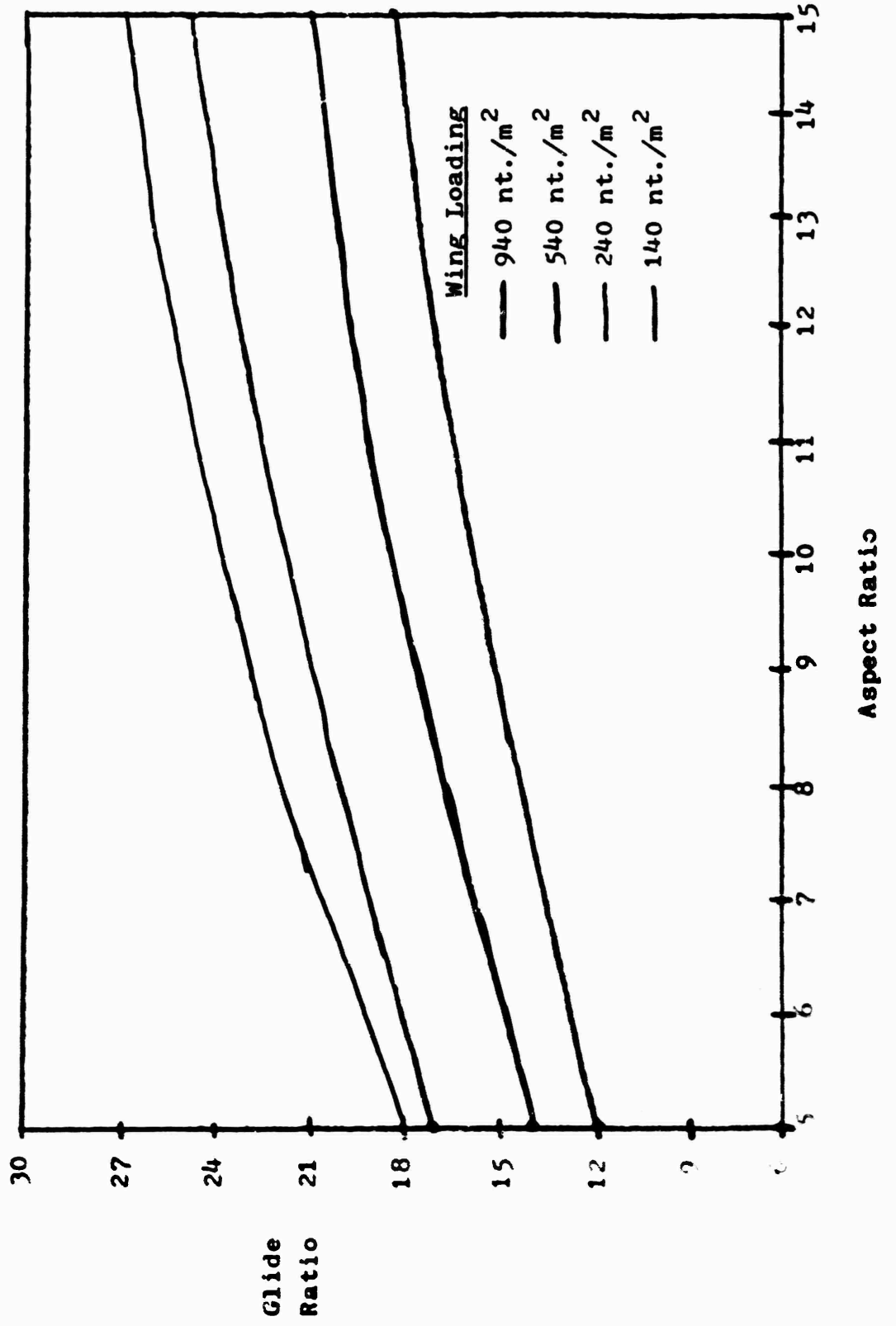
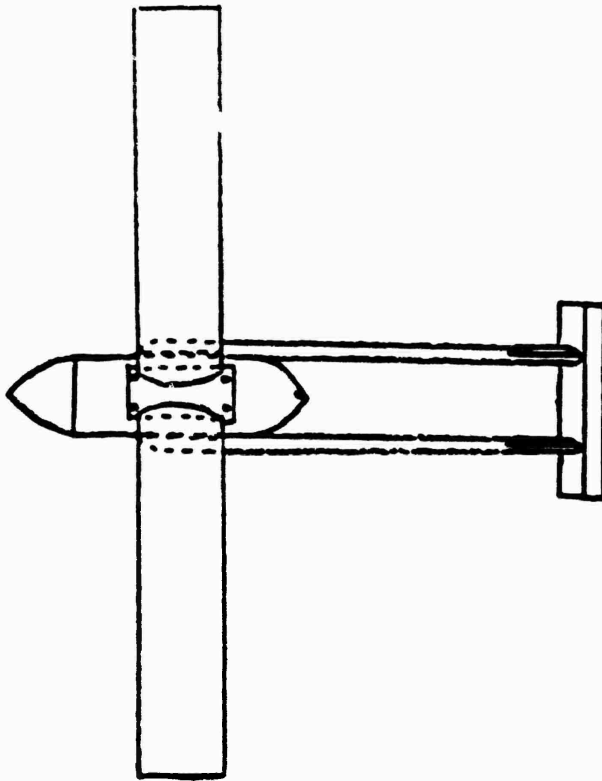
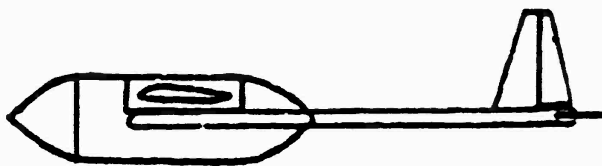


Figure 2



Top View



Side View

Appendix A

Gross Weight	5.7 kg.
Empty Weight	~2.8 kg.
Wing Loading	240 newtons/meter ²
Wing Area	0.232 meter ²
Aspect Ratio	10
Span	1.52 meters
Chord	0.15 meters
Thickness/Chord	0.18
Airfoil	NACA 65 ₃ -418
Length	1.1 meters
Fuselage Diameter	0.125 meters
Vertical Tail Area	320 cm. ²
Horizontal Tail Area	250 cm. ²
Dihedral Angle	10½ degrees

Appendix BStability Derivatives:Longitudinal:

$$C_x = 0.384$$

$$C_z = -5.48$$

$$C_l = 5.48$$

$$C_m = -1.64$$

$$C_{x_u} = -0.04$$

$$C_{z_u} = -0.0035$$

$$C_{m_u} = 0$$

$$C_{z_q} = -3.942$$

$$C_{m_q} = -20.75$$

$$C_z = -0.788$$

$$C_m = -4.15$$

$$\dot{a} = 5.24$$

Lateral:

$$C_n = 0.12 + 0.0075 C_l$$

$$C_y = -0.2715$$

$$C_l = -0.1288 - 0.03 C_l$$

$$C_{y_p} = 0$$

$$C_{l_p} = -0.375$$

$$C_{n_p} = 0.0136 - 0.1 C_l$$

$$C_{y_r} = 0.2853$$

$$C_{l_r} = 0.0136 + 0.275 C_l$$

$$C_{n_r} = -0.1574 - 0.01 C_l^2$$

@ 25 m/sec

@ 100 m/sec

Short Mode:

Period:	0.665 sec	0.166 sec
Halving Time:	0.18 sec	0.045 sec
Cycles to Halve:	0.271 cycles	0.271 cycles

Phugoid Mode:

Period:	11.4 sec	-
Halving Time:	55.3 sec	-
Cycles to Halve:	4.85 cycles	-

Spiral Mode:

Halving Time	116.4 sec	0 sec
--------------	-----------	-------

Rolling Mode:

Halving Time:	0.092 sec	0.026 sec
---------------	-----------	-----------

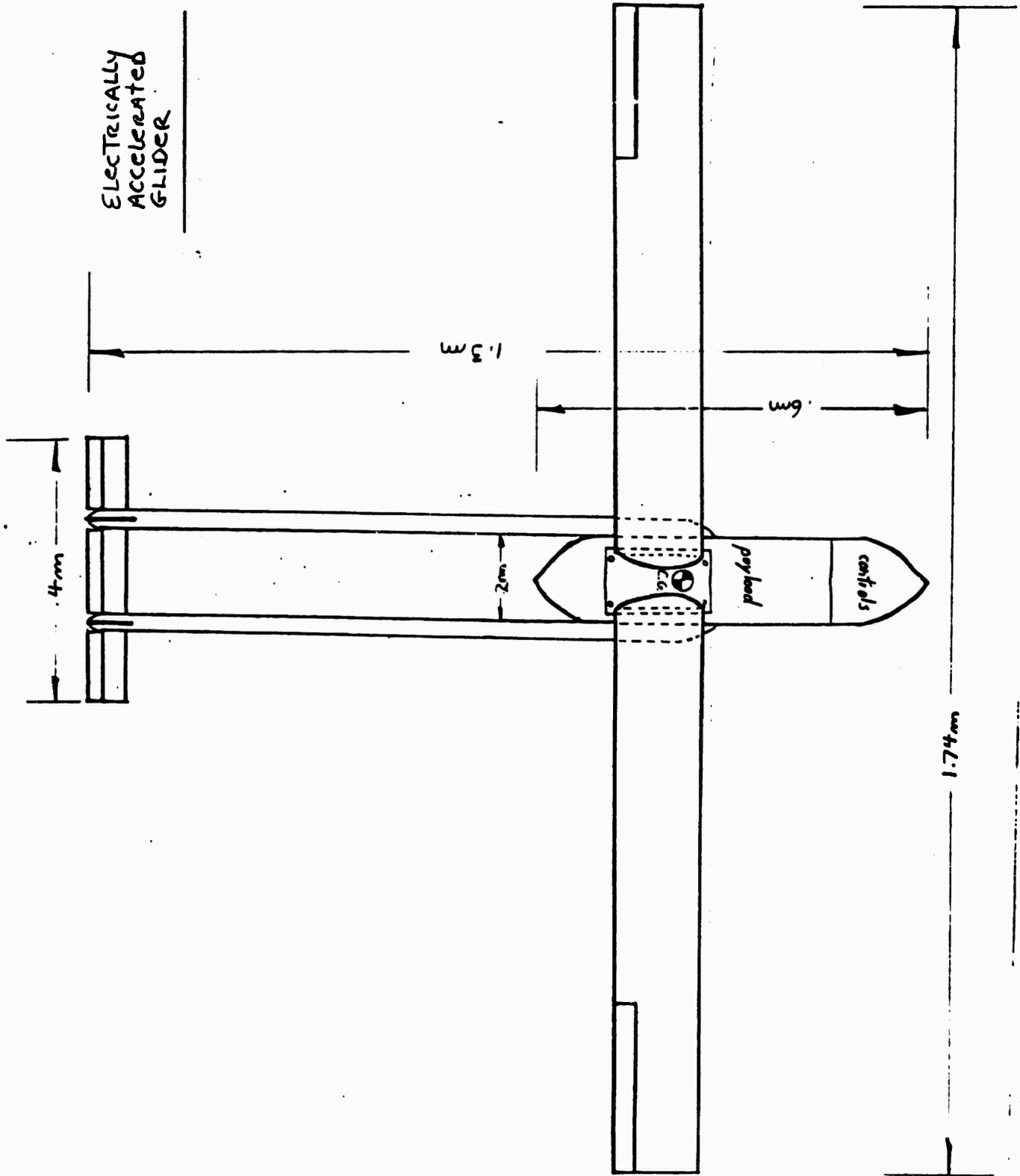
Dutch Roll Mode:

Period:	1.04 sec	0.293 sec
Halving Time:	2.286 sec	0.239 sec
Cycles to Halve:	2.2 cycles	0.8 cycles

References

- 1) Etkin, Dynamics of Flight: Stability and Control,
New York, Wiley, 1959
- 2) Welch and Irving, New Soaring Pilot, London, John Murray,
1970
- 3) Nash-Webber, The Effect of Wing Loading On The Performance
Of Advanced Sailplanes, SSA-AIAA Symposium, March 1974
- 4) D. Althaus, Stuttgarter Profilkatalog, Stuttgart,
Institute for Aerodynamics and Gas Dynamics, 1972
- 5) D.J. Marsden, Sailplane Performance Estimation, Technical
Soaring, Volume V, No. 3
- 6) E.E. Larrabee, The Aerodynamic Design of Sailplane
Tail Assemblies, Technical Soaring, Volume V, No. 1

ELECTRICALLY
ACCELERATED
GLIDER



PULSED COIL DYNAMICS

There is a category of accelerators based on the use of a line of adjacent, coaxial pulsed drive coils, each drive coil being supplied with a current pulse synchronized with the passing bucket. In the case of mass drivers, the bucket coils carry a persistent superconducting current, and the drive coils are energized by SCR switches triggered on the basis of position sensors. Acceleration in this case is limited by the current or energy handling capability of available SCRs. It is possible to achieve higher performance however by switching the pulsed current by means of a spark or arc triggered by the vehicle itself. Such arc-commutated synchronous impulse accelerators can operate with energized bucket coils (superconducting or brush-fed), or bucket coils which are simply short-circuited and are energized by induction, like a brass washer being repelled by a pulsed field coil. The melting limit in such accelerators is very high, and performance is limited, in practice by failure of the pulsed drive coils.

Massive helical and spiral pulsed field coils, such as are used for metal forming and solid state research, have been studied on a number of occasions, but the kind of thin coils which must be used in synchronous accelerators, i.e., coils whose build is small compared to their diameter, have never been studied. The performance limit of such coils is completely unknown, and there exists no data base suggesting how their performance limit can be maximized. For example, is it better to surround a drive coil with lead or with pre-stressed glass or boron filaments?

Considered statically, a thin coil is subjected simply to radial expansion forces (hoop stress). If it has any appreciable length, it is also subjected to axial compression which may be the dominant failure mode. A coil will tend to become spherical, just as if it were containing a compressed gas between imaginary end plates. Static stress analysis is applicable in the slow pulse regime, say in the range of one to tens of milliseconds. Containment in this range is most easily accomplished by using a pre-stressed hoop or reinforced conductor, or both.

Under faster pulse conditions, say from several microseconds to a millisecond, stress containment is predominantly dynamic. In addition, the situation is complicated by other effects. Current and magnetic field no longer penetrate the entire conductor, being limited by skin depth effects. Percussive forces overcome the friction which keeps steady state coils from simply unwinding. In the absence of friction the turns of a coil no longer behave independently but act mechanically in series, each turn adding its force to that of the preceding turn like members of a tug-of-war team pulling on a single rope. Cumulative forces are now applied to the insulation between layers. In addition, inductive effects make high voltages appear between coil layers and at terminal connections. Coil wires are also subjected to image forces generated by eddy currents induced in nearby metal structures, including the bucket being accelerated. The situation is too complicated for failure modes to be predicted, and it is therefore necessary to develop an understanding of the problems by a combined program of experimentation and analysis.

For this purpose we have constructed a test jig shown at right, in which thin pulsed coils can be tested to failure, either without proximity of metal, or near an aluminum reaction plate which simulates axial repulsive forces due to a neighboring drive coil or due to the bucket coil being accelerated. The jig is contained in a plywood strongbox. Deformation was measured by unwinding the coil wire and noting its change in length, but provisions have been made for strain gages.

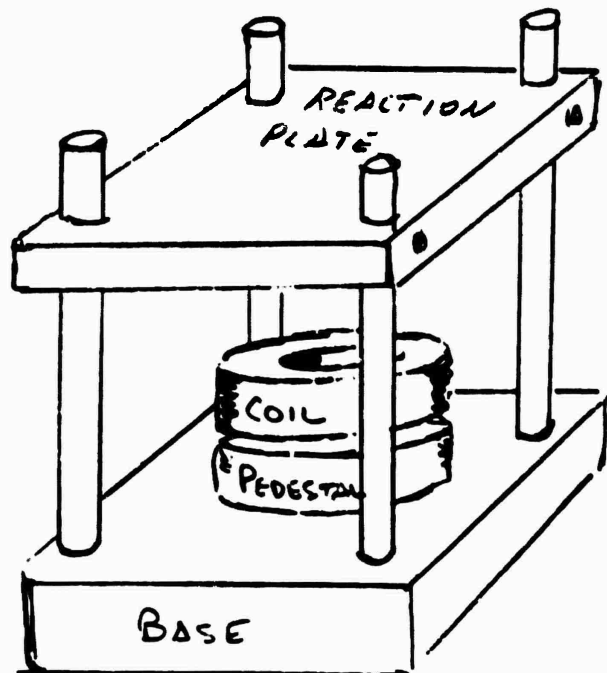


Fig. 17. Coil testing jig

Tests were done with copper wire, aluminum wire, and a readily available reinforced copper wire in the form of niobium-titanium superconductor made of niobium-titanium filaments having very high tensile strength embedded in about three times their cross section of copper matrix. Energy was obtained from modules of the electrolytic capacitor bank. Pulse durations thus far have been in the range where coil failure is either thermal, or governed by purely static considerations. The fast capacitor bank will eventually be used to operate in the range where containment is dynamic. In the dynamic range an impulse, the time-integral of a force which is proportional to current squared, is delivered to the conductor in a time too short for any motion to occur. After the impulse, the conductor is left with momentum locally equal to the force integral, which is equivalent to a kinetic energy distribution. This kinetic energy is then dissipated against restoring forces either within the elastic limit, or else under plastic flow conditions if the elastic limit is exceeded. It is in this range that local mass concentrations coupled to the conductor may be more effective for force containment than high-strength reinforcement.

The coil dynamics project was conducted by Osa Fitch as an experimental project for academic credit, with supervision by W. Markey and A. Shaw. Several other undergraduate students also participated in the work, notably Ken McKinney, who assisted with computer programming. More details of this study are contained in Osa Fitch's report, which is attached as Appendix A.

THE MOMENTUM TRANSFORMER

BASIC PRINCIPLE

Conventional kinetic energy penetrators are typically 35 mm caliber tungsten darts which are accelerated in a 105 mm barrel by means of a sabot which breaks away when leaving the muzzle. The kinetic energy of the sabot is lost.

It is possible in principle to transfer some of the sabot's energy to the penetrator, transferring momentum from a massive, slowly moving assembly to a lighter, faster moving part of it. The penetrator could thus be made to emerge at a significantly higher velocity than can be achieved in a chemical gun.

The process is based on the principle of the flux concentrator, a device developed at MIT in 1960 and used to achieve strong pulsed fields for research and for metal forming applications. When a funnelled metal cylinder with a radial slot is surrounded by a pulsed field coil as shown in Fig. 19, eddy currents induced in the metal as indicated cause all the magnetic flux which would have filled the entire coil to be compressed into the interior of the funnelled cylinder. Flux is thus compressed by a ratio approaching the cross section area ratio of the funnel.

By accelerating a sabot shaped like the flux concentrator into a magnetic field it is possible to eject the penetrator by means of the compressed flux at the expense of kinetic energy of the sabot.

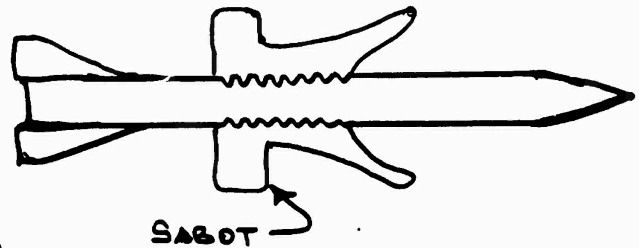


Fig. 18. Conventional sabot and armor penetrator.

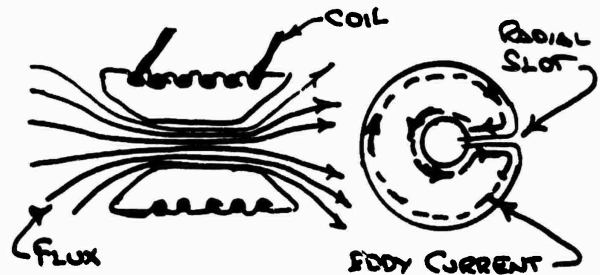


Fig. 19. The flux concentrator

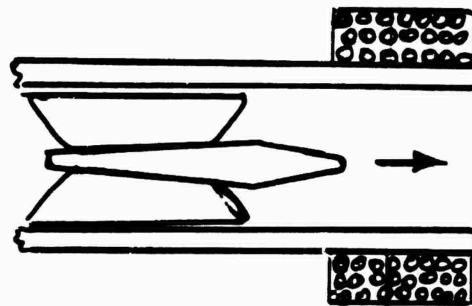


Fig. 20. The momentum transformer.

EXPERIMENTAL APPARATUS

Apparatus has been constructed for exploring this effect by using compressed gas to inject a flux concentrating sabot containing a projectile into a magnetic field located at the end of a 3 meter barrel. A caliber of one inch proved expedient because it results in the maximum velocity obtainable with commercially available solenoid valves. A photograph of the installation is shown in Fig. 20, and an elevation drawing in Fig. 21 on the following page.

Fig. 21 Pneumatic injector for momentum transformer experiment; also shown is bench model of helical accelerator and two modules of 6 kV, fast capacitor bank, under bench.



A ballast tank, contained in plywood box, is pressurized to a maximum of 1,500 psi from a compressed gas tank. The projectile is placed into the breech block, which is then sealed with a pipe plug. The breech is pressurized by means of a solenoid valve. Volume of the ballast tank is 3.3 times the barrel volume. Aluminum bolts of 55 gm mass can be accelerated to about 280 m/s if helium is used as propellant gas.

The coil for generating the magnetic field, comprising 200 turns, is wound around a copper muzzle extension secured to the test bench, as shown in Fig. 21. The total length of the apparatus is 12 feet.

Two single-flash strobes are used to make a Polaroid photograph of the sabot and projectile emerging from the muzzle, and the event is also

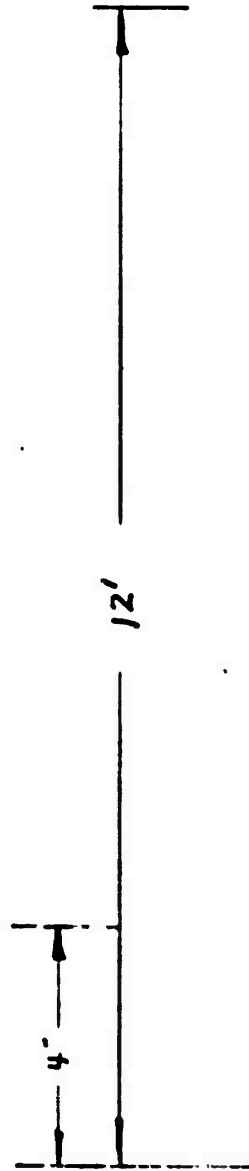
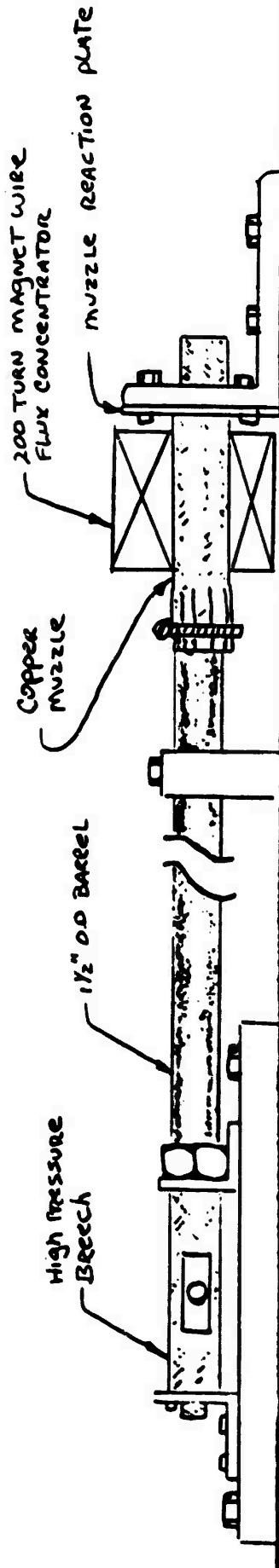


Fig. 22. Pneumatic injector and muzzle coil for momentum transformer

recorded electrically with the Nicolet digital oscilloscope. Added information is obtained by recovering the sabot and projectile intact from a target box filled with polyurethane foam and sand.

PRELIMINARY RESULTS

A number of difficulties have been encountered, and results are still ambiguous. The projectile usually separates from the sabot, but this could be due to deceleration of the sabot without any significant acceleration of the projectile. The basic problem is the fact that electromagnetic flight cannot be scaled in the manner of aerodynamic flight, where performance can be explored by simple wind tunnel experiments.

The scaling problem is related to the fact that the skin depth, or the depth at which a penetrating magnetic field is attenuated to $1/e$, is inversely proportional to the square root of effective frequency, or to the square root of the rise time or duration of a pulse. Skin depth is also proportional to the square root of resistivity.

The full size system we are modelling has a caliber of 105 mm (4 inches) and operates at a velocity of say 1100 m/s. Our model is one quarter scale (1 inch caliber), and operates at one quarter velocity (280 m/s). The effective pulse duration, or the time required for the sabot to pass through the muzzle coil, is therefore the same in our model as in the full size system, which means that the skin depth is also the same, i.e., four times the scaled size. To reduce the skin depth to proper size, one would have to increase the velocity or the conductivity by a factor of sixteen.

The fact that skin depth is four times proper size makes the entire process mushy. Magnetic flux is pushed into the copper muzzle tube as the sabot enters, and magnetic pressure between the sabot and the projectile is decreased because flux penetrates into both.

The copper muzzle pipe needs to be four times thicker than in the full size device, and this prevents the pulsed field from penetrating to the interior. We attempted to generate a quasi-continuous muzzle field by using six lead-acid batteries, but this field was too weak to cause even separation of the projectile. One test was made by moving the pneumatic injector to a 190 kilogauss continuous Bitter solenoid magnet, but the extended field generates enough drag to decelerate both the sabot

and the projectile, masking whatever momentum transfer might have taken place between them.

It was also noted in the one test with the Bitter solenoid that the sabot is deflected violently in the direction opposite the slot, with enough force to mash it against the copper barrel so as to cause visible friction wear opposite the slot.

It may be necessary to evolve a more sophisticated design, such as for example a second flux concentrator surrounding the barrel, energized with a considerably faster pulse from our fast bank. Cooling the sabot and projectile to liquid nitrogen temperature would also help, but only by decreasing the skin depth by a factor of about $\sqrt{6} = 2.45$.

If all else fails, the experiment will have to be done at full scale and full velocity, using an explosive gun rather than the pneumatic injector.

MASS DRIVER TWO CRYOGENIC SYSTEM

Mass Driver Two is a four inch caliber, synchronous accelerator with SCR-switched copper drive coils and a superconducting bucket, operating in an evacuated tube. Design acceleration is 500 gee. The drive coil structure and associated power supply is being built at Princeton University by a group headed by Prof. G.K.O'Neill and William Snow. The superconducting bucket and associated cooling station is being designed and built by the MIT group, both operations being supported by a NASA grant administered by Lewis Research Center.

The driver was to be housed in standard pyrex flanged piping surrounded by the drive coils, but it proved impossible to prevent the pyrex from shattering due to dynamic deflection of the structure supporting the drive coils. The 2.5 meter accelerating-decelerating section was rebuilt using a vacuum grade of lexan plastic. It also proved impossible to contact-cool and induction-charge the bucket coils in a pyrex tube without radiation shielding, and therefore the cooling station was re-designed to operate in a stainless steel tunnel surrounded by liquid helium. The tunnel tube contains a set of copper contact blocks against which the bucket is forced by a set of cams, and the tube is surrounded by two superconducting coils which serve to induce a persistent current into the bucket coils. The procedure is to energize the induction coils, cool the bucket to below its transition temperature, and then de-energize the induction coils, leaving the bucket coils with the persistent current required to maintain the induced flux.

The two bucket coils are imbedded in woods-metal, the material which has the highest specific heat at helium temperature except for helium itself and water ice. There is enough thermal inertia to keep the bucket coils superconducting as they are ejected from the cooling station by a set of two pulsed copper ejection coils along teflon guides.

Detailed design calculations have been reported in earlier NASA progress reports. Drawings and photographs of the re-designed station appear on the following pages.

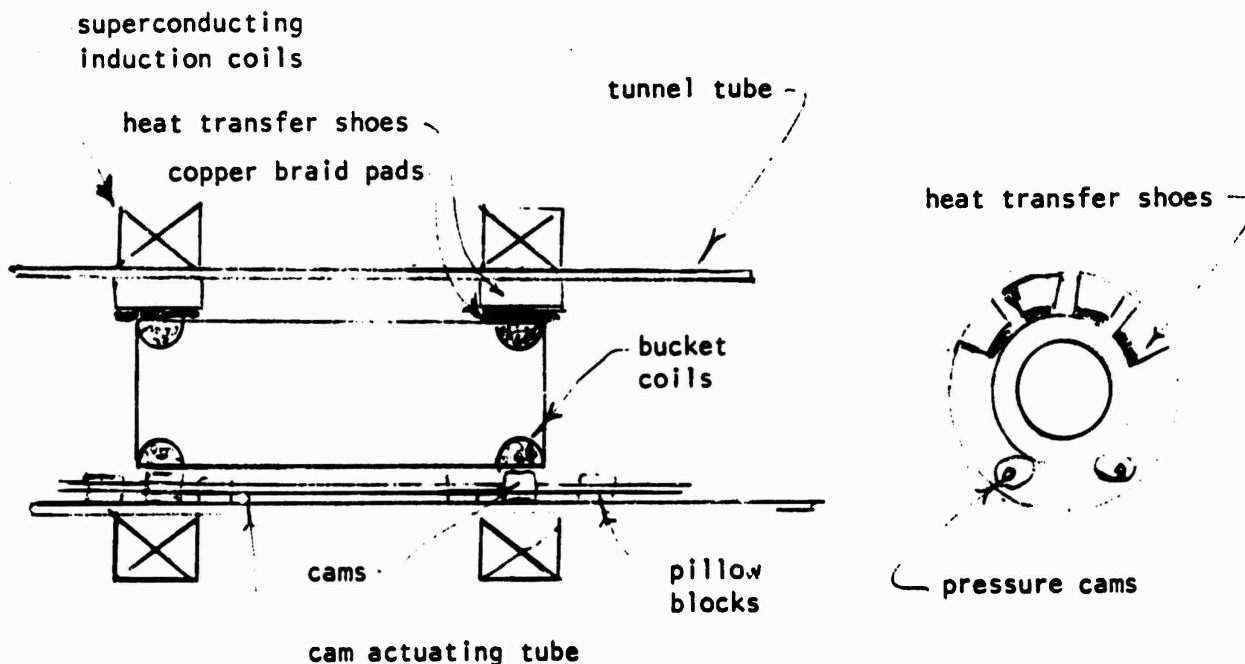


Fig. 23 Mass Driver Two bucket in cooling station tunnel tube; the tunnel tube is surrounded by liquid helium

The tunnel tube and associated parts were constructed first. The tube was welded shut at one end, and provided with a flanged top at the other end in order to permit operational testing before construction of the remainder of the dewar. The tunnel tube is shown in the photograph of Fig. 25 prior to immersion in an available helium dewar for testing. Longitudinal and cross section views are shown in Fig. 23, and Fig. 24 shows the bucket in front of a section of tunnel tube with the copper heat transfer shoes visible. Fig. 26 is a simplified sectional assembly view of the entire dewar.

With the radiation heating eliminated, the bucket can be cooled down rapidly to about 13°K, the cool-down rate depending crucially on contact pressure applied by the cams. Introduction of helium transfer gas increased the cool-down rate tremendously. Cool-down from 25°K following a quench to 4.2°K required about one minute, with transfer gas.



Fig. 24 Mass Driver Two bucket in front of section of tunnel tube, showing heat transfer shoes with copper braid pads



Fig. 25. Tunnel tube, with ends closed for testing in helium dewar in Bitter magnet. Only a short center section of the tunnel tube will be used in the final dewar vessel

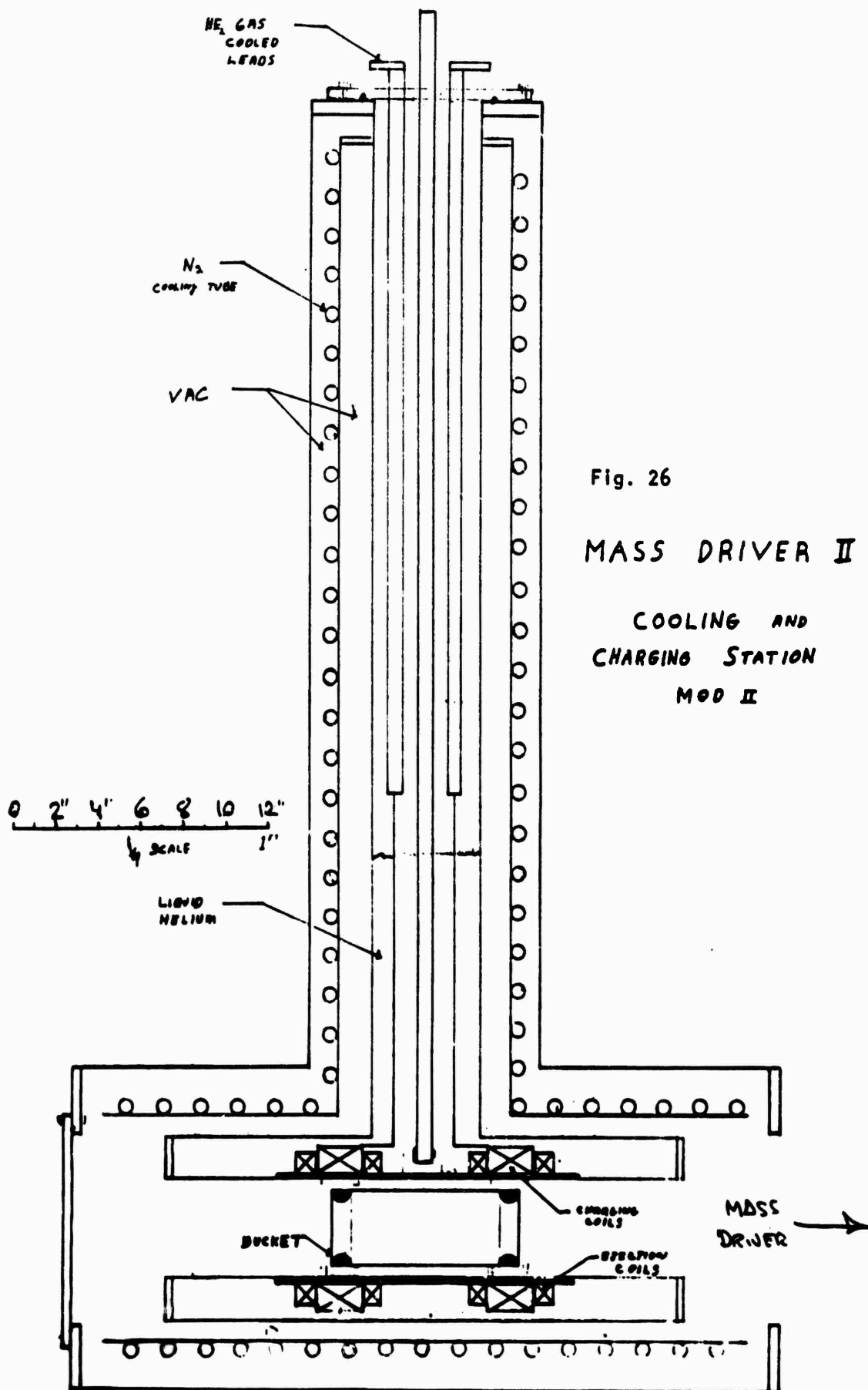


Fig. 26

MASS DRIVER II

COOLING AND
CHARGING STATION
MOD II

RESULTS OF TEST IN BITTER SOLENOID MAGNET

The tunnel tube was immersed in liquid helium using an available dewar, and placed inside the bore of a ten inch caliber Bitter solenoid magnet. Ten resistance thermometers were used to monitor heat flow, and pick-up coils served to observe the persistent superconducting current in the bucket. The results are summarized as follows:

THERMAL BEHAVIOR

With a thermal vacuum in the tunnel tube, contact cooling resulted in a bucket temperature of 13°K in several minutes, but at that temperature the contact transfer just balanced radiation input from the top flange, which was at room temperature. No further cool-down could be achieved. The minimum temperature varied with the force applied to the contact pressure cams, confirming that it was the contact transfer which limited cool-down. The contact pressure was limited in essence by deformation of the 0.064 wall tunnel tube. The pressure mechanism is being re-designed to achieve greater total contact force distributed over a larger area. Heat transfer is known to be proportional to total force.

With several millimeters of helium gas in the transfer tube, cool-down to 4.2°K took place within seconds. The time required to cool the bucket from 25°K (following a quench) to 4.2°K, with transfer gas, was about one minute.

ELECTRICAL BEHAVIOR

Stable operation was achieved to a background field in the Bitter Solenoid of 14 kilogauss, i.e., the bucket did not quench to that field intensity, and the persistent current which remained after the solenoid magnet was turned off showed no measurable decay in a period of ten minutes. The bucket was found to quench at 18.1 kG, which provides ample safety margin.

The current density corresponding to a persistent current capable of sustaining a central field of 14 kilogauss is:

- 31.7 kA/cm², referred to the entire bucket coil structure,
- 45.3 kA/cm², referred to the superconducting cable with copper,
- 136 kA/cm² referred to the superconducting filaments of NbTi.

The design value of current density is 25 kA/cm² referred to the cable. The bucket is thus able to carry nearly twice the design current density, which implies that it will achieve twice the anticipated acceleration. However, in actual operation the bucket coils will be subjected to a certain amount of transient background field as the bucket enters the first drive coil, although most of this transient will be shielded by the massive copper ring which surrounds each bucket coil. Some degradation of critical current must be expected.

CONCLUSIONS

Electrical operation of the bucket exceeds design expectations by a factor of two in terms of stable current density in the absence of background field transients, even with the first bucket built!

The contact cooling system is able to transfer only one watt across the copper-to-copper surfaces, which is in approximate agreement with heat transfer rates reported in the literature at the total force achieved.

However, it is known that heat transfer rates are better by a factor of twenty if the surfaces are gold-to-gold, due to quantum-mechanical effects involving phonon transfer matching conditions at the metal-to-metal interface without the interposition of an oxide. Detailed results are reported in *Guy K. White, "Experimental Techniques in Low Temperature Physics", Oxford University Press 1979, page 149*. Evidently the field of contact heat transfer has received considerable attention recently.

A twenty-fold increase in heat transfer rate will eliminate the need for using a transfer gas. It therefore seems that after gold-plating the heat transfer contact, construction of the remainder of the cooling station can proceed without further problems or delay.

EARTH-BASED SPACE LAUNCHERS

RATIONALE FOR CATAPULTS

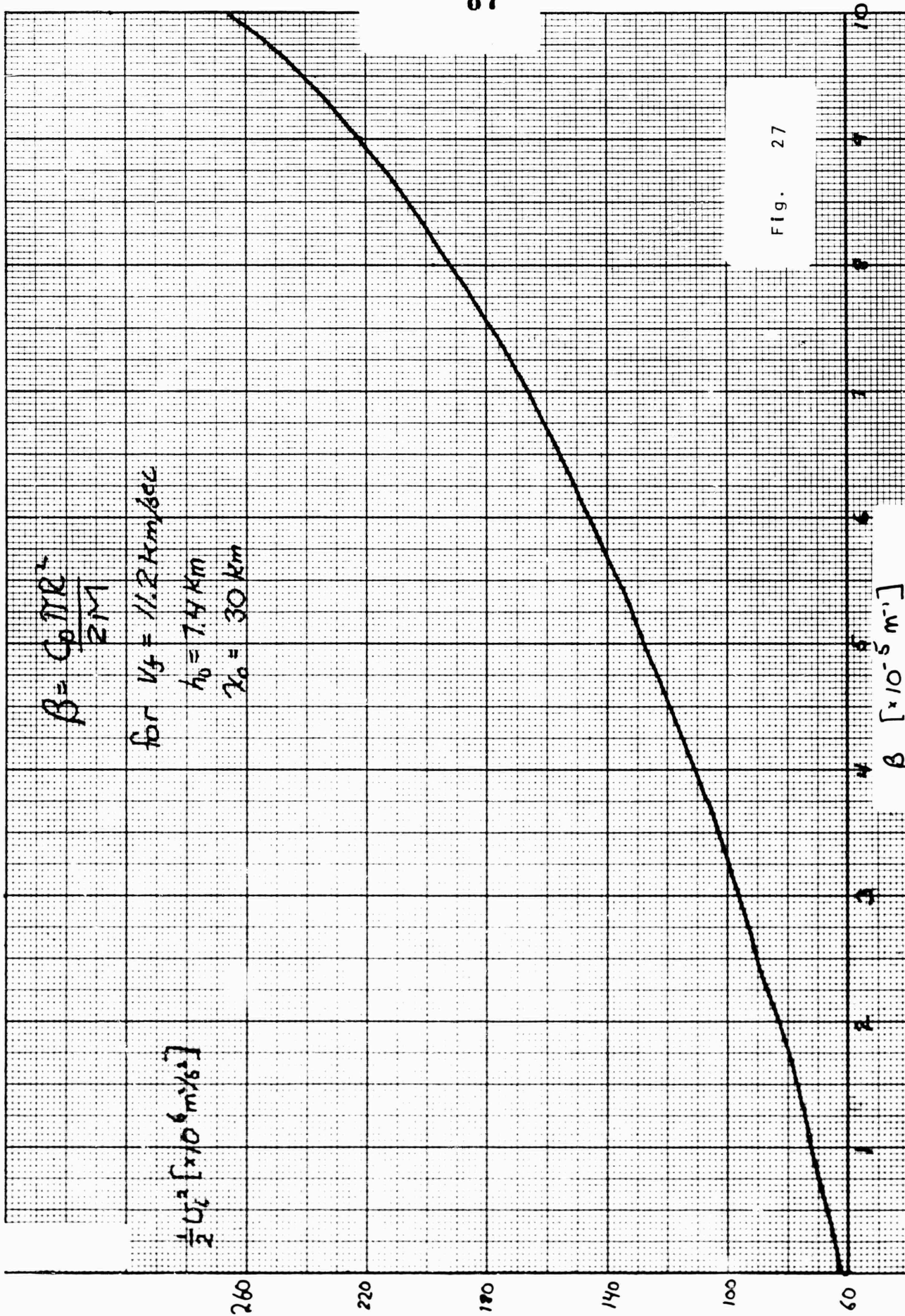
The typical payload ratio of present launch vehicles is 137 (the European Ariadne); i.e., 136 pounds of fuel and expensive engines accompany each pound of payload. Launch velocities range from about 7 km/s for low orbit, to 11 km/s for earth escape, and chemical guns are unable to achieve these, although attempts made in the sixties by welding two naval gun barrels together came close.

Electromagnetic catapults are able in principle to achieve required launch velocities, certainly for first stage purposes, and have been written about by science fiction authors for several decades. They have never been taken seriously, however, because it was assumed that launch vehicles would have to be unrealistically large to survive passage through the atmosphere at a reasonable loss of ablation mass and energy.

The first serious study of ablation and energy losses, to our knowledge, was made during the 1977 NASA-AMES Summer Study on Space Industrialization by Chul Park and Stuart Bowen. Their work has only recently been completed (December 1979), and is to appear in *Journal of Energy*, under the title: *Ablation and Deceleration of Mass Driver Launched Projectiles for Space Disposal of Nuclear Wastes*. Preprints are available from Dr. Chul Park, Nasa-Ames Research Center, Moffett Field, CA 94035.

From the formulation of Park and Bowen we have derived the beta factor for launch to escape velocity (11.2 km/s), plotted in Fig. 27, and used this curve to calculate the launch energy as a function of vehicle mass for vehicles of radius 3cm, 5cm, 10cm and 15cm, plotted in Fig. 28 to 31 respectively. Each curve shows a distinct minimum mass, below which the launch energy increases drastically. For a vehicle radius of 3 cm, the minimum mass is only 25 kg!

These losses seem surprisingly low, considering the well publicized difficulty in entering the atmosphere from above. There are two direct



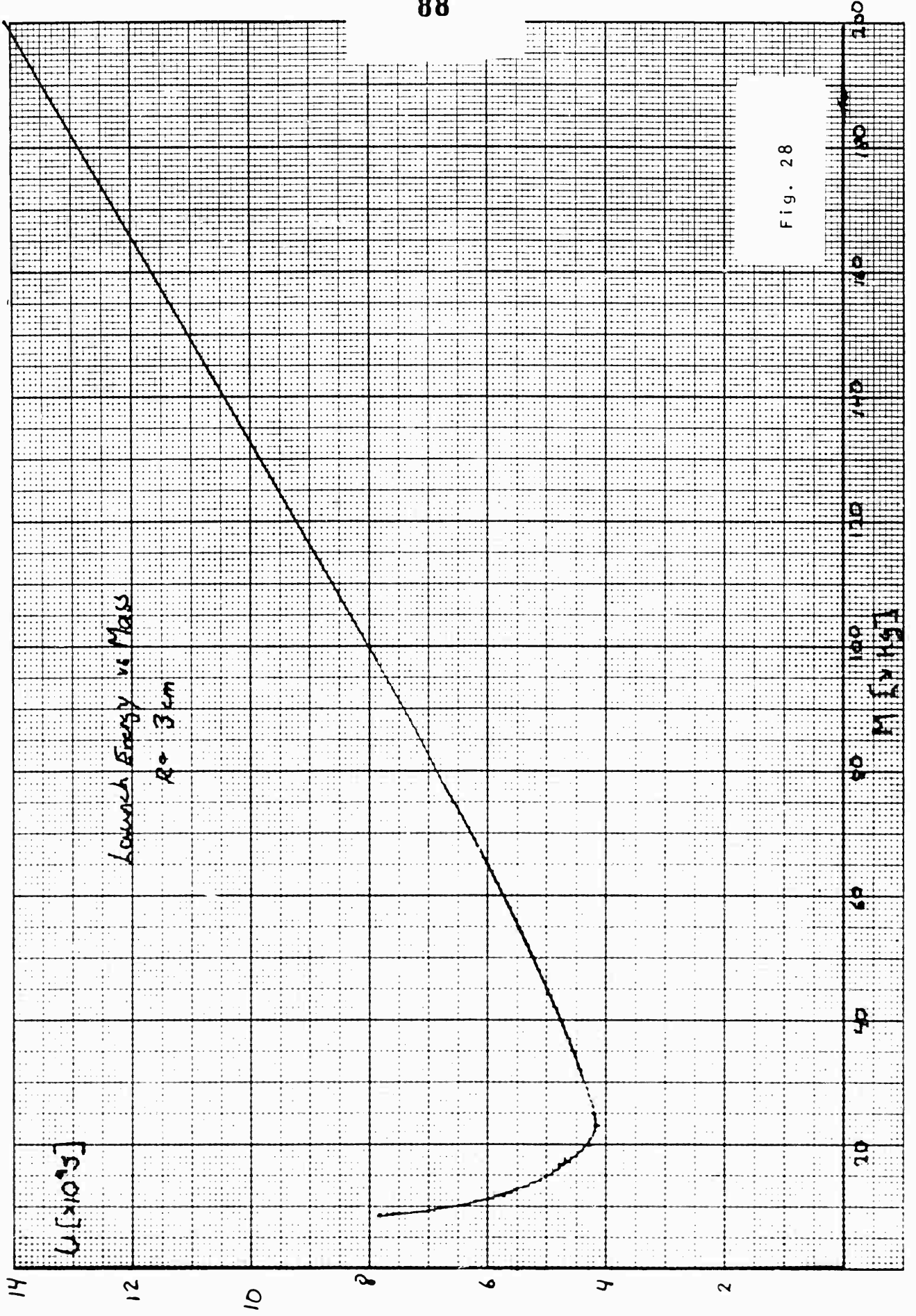
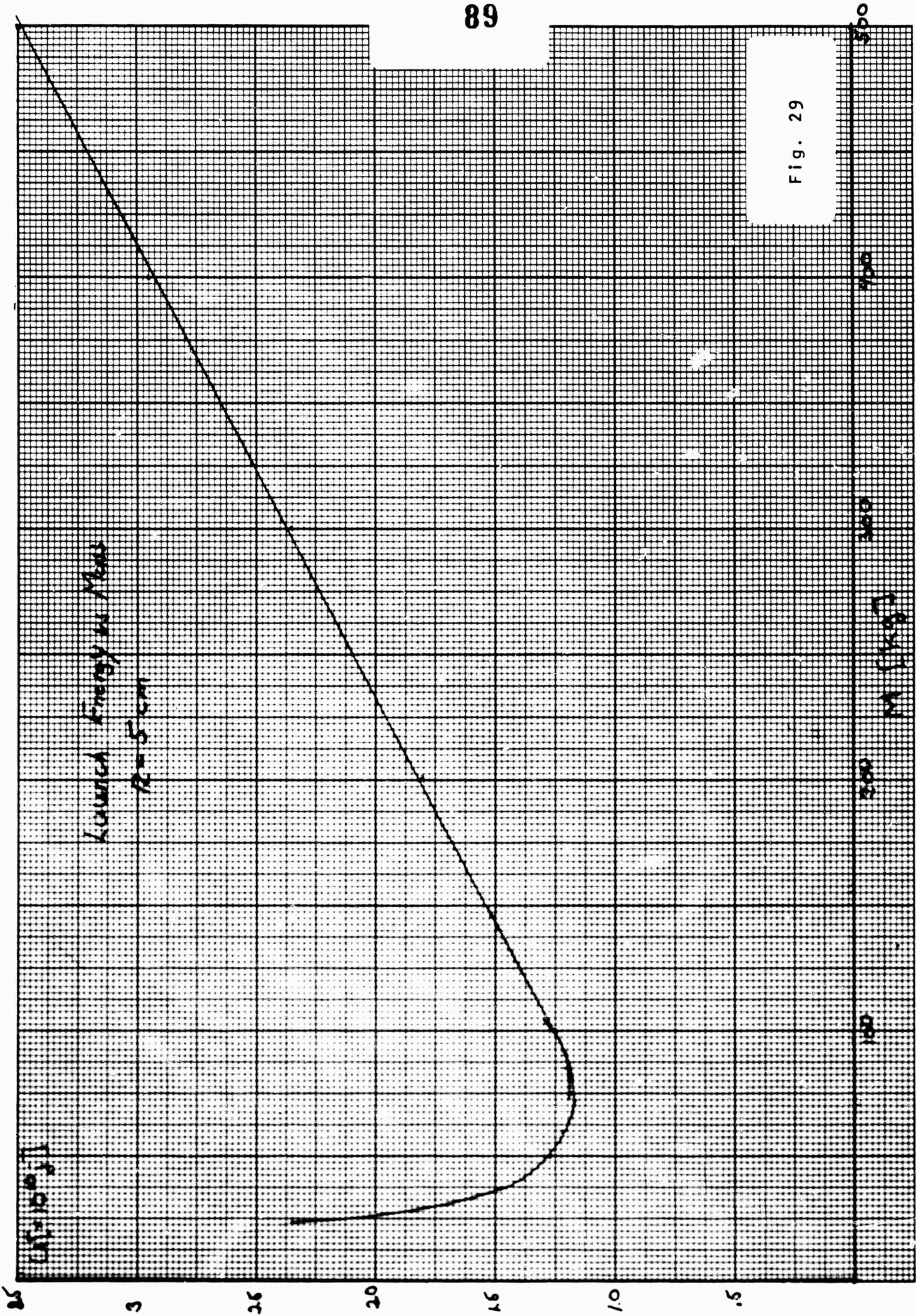
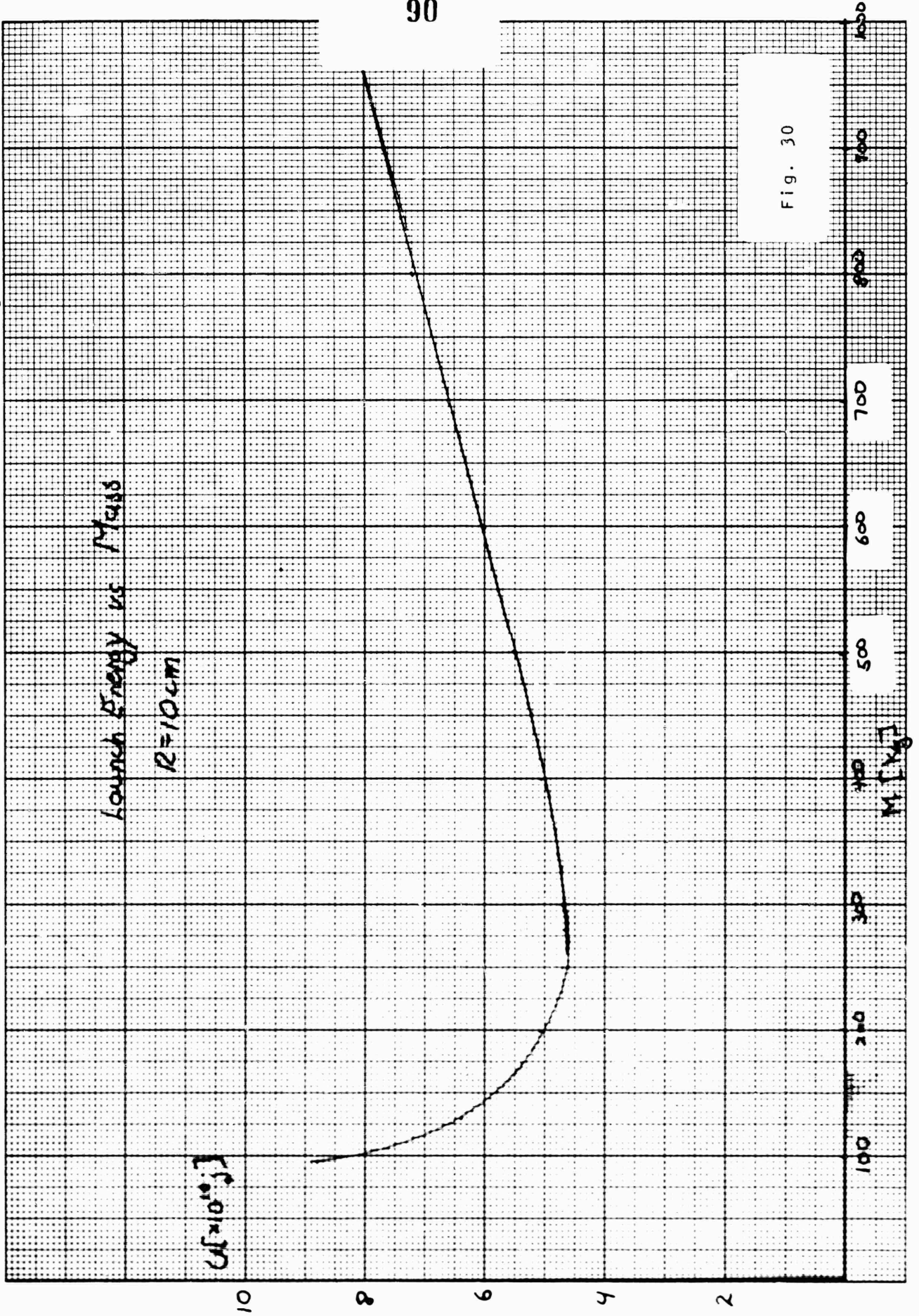


Fig. 28





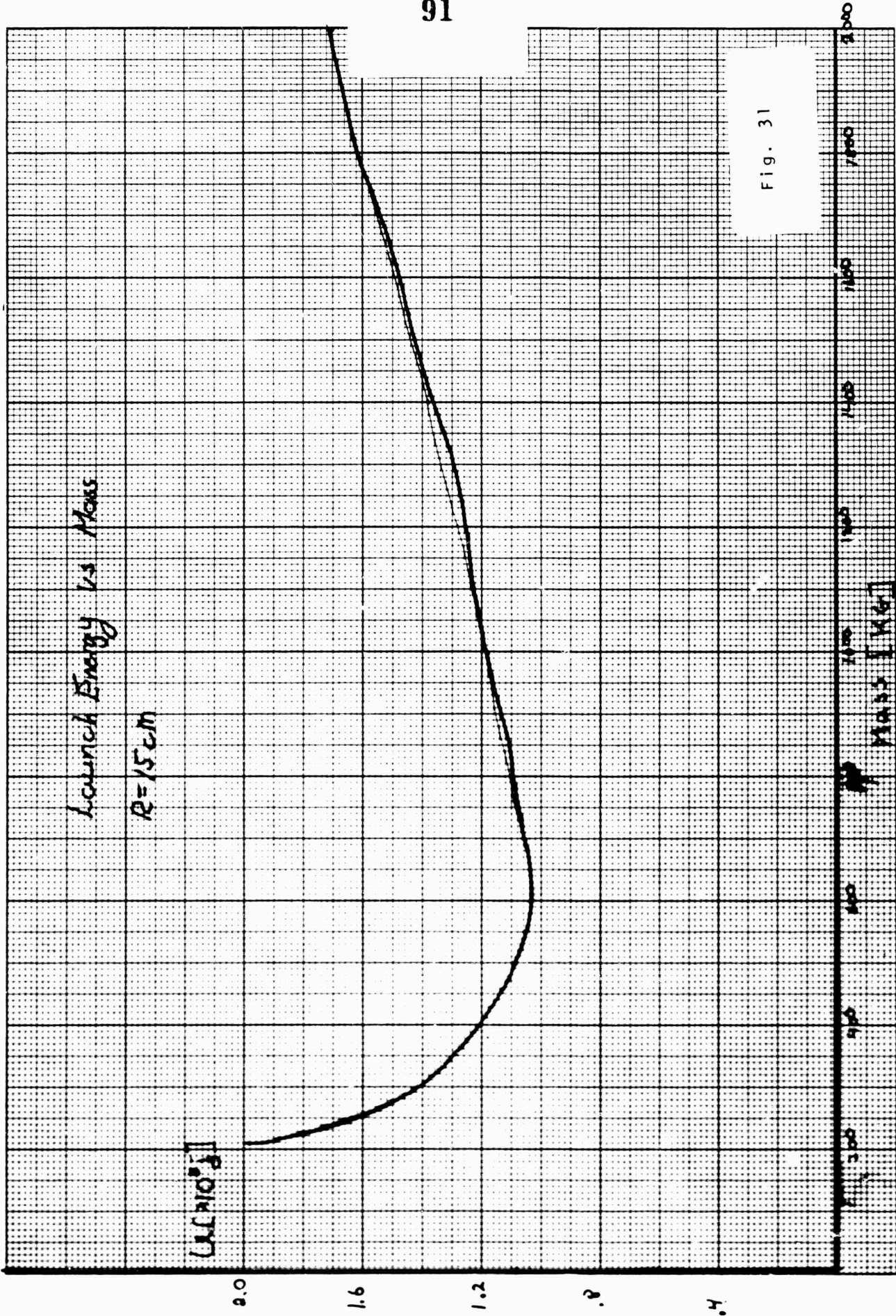


Fig. 31

reasons for the low losses. Traversing the atmosphere vertically at escape velocity results in a two-second flight, as compared to the many minutes required for atmospheric braking at a deceleration level survivable by astronauts. A second, less obvious advantage derives from the fact that ablation products (carbon vapor) are sufficiently opaque at high atmospheric pressure to shield the nose cone from heat generated at the shock front and transferred mainly by radiation.

It is thus clearly possible to launch vehicles of reasonable size electromagnetically, at payload ratios approaching unity, and at a cost approaching the cost of the launch energy, which is only 65 cents/pound, excluding amortization of equipment.

THE TELEPHONE POLE LAUNCHER

For the purpose of exploring earth-based launchers, we consider a reasonable reference design. We select a vehicle having the shape and size of a telephone pole and a mass of 1,000 kg, a useful cargo package which is large enough to make energy losses acceptable, and small enough to keep energy storage requirements low. We select a launcher length equal to the deepest well holes customarily drilled in order to permit a near-vertical trajectory. The design parameters are as follows:

Vehicle:	telephone pole shaped, mass 1,000 kg
launch velocity:	12.3 km/s
velocity at top of atmosphere:	11 km/s, earth escape velocity
kinetic energy at launch	76×10^9 joule
ablation loss, carbon shield	3 percent of mass
energy loss	20 percent
acceleration	1,000 gee ($10,000 \text{ m/s}^2$)
launcher length:	7.8 km
launch duration:	1.26 second
average power	60×10^6 kilowatts
average force	9.8×10^6 newton = 2.2×10^6 pound-force
charging time, from 1,000 MW power plant	1.5 minute

The cost of the required mass driver, in terms of copper, steel and concrete is only of the order of 22 M\$. However, the capacitors for storing 76 Gigajoules of energy would cost about 11 B\$.

It is somewhat less discouraging to consider the energy requirement in terms of power: the proposed launch would require storing the output of a 1,000 MW power plant for 1.5 minutes, and releasing it in 1.5 seconds, a 60-fold power compression.

Reducing the acceleration would result in a longer launcher which, up to several more miles, would have to be installed on a mountainside at a launch angle of perhaps 45 degrees. This is not out of the question, since the increased atmospheric loss might be offset by the reduced cost of storage. With a sufficiently small vehicle and a sufficiently long launcher it might even be possible to operate at a level of power which can be derived from an existing power plant, or several connected plants, perhaps during off-peak hours, without the need for any storage system.

Another alternative approach might be to use electromagnetic launching only to replace the first stage vehicle, representing a launch velocity of only about half the escape velocity assumed above, or a launch energy of 25 percent.

Another alternative worth considering is the use of inductive energy storage in superconducting coils, a method which has been considered for a variety of applications, including even the peak-shaving of electric power demand.

Inductive energy storage is very expedient for electromagnetic launching purposes because an inductor represents a constant current source.

THE SELF-ENERGIZED SUPERCONDUCTING MASS DRIVER

A very attractive possibility is that of using the drive coil structure of a mass driver for inductive energy storage. Peter Graneau of our group has studied this possibility in detail, and his analysis is contained as Appendix 2. We summarize the results on the following page, in Fig. 32, which gives the design parameters of this reference design. The bottom line is that a 35 cm caliber mass driver, 1 km long with superconducting drive coils can store enough energy inductively (at a very conservative current density) to accelerate a 20 kg bucket to 10.5 km/s.

This mass driver would be a pull-only device, operated by pre-charging all drive coils and then breaking the circuit of each coil at the instant the bucket reaches the plane of symmetry. It is interesting to note that the drive coil current can be made to have an arbitrarily low value at the instant the circuit is broken by suitable choice of the bucket coil parameters, because flux conservation will tend to cause current sharing between drive coil and bucket coil. Clearly the remaining energy would have to be dissipated in external resistors rather than in the cryostat system, by quenching. Very challenging engineering problems remain to be solved, but the project clearly merits serious study. The carrot ahead of us is the possibility of launching cargo into space at a cost of 65 cents/pound. Even if an electromagnetic catapult were to replace only the first stage of a space launch, it would still represent more than a ten-fold savings in energy and cost!

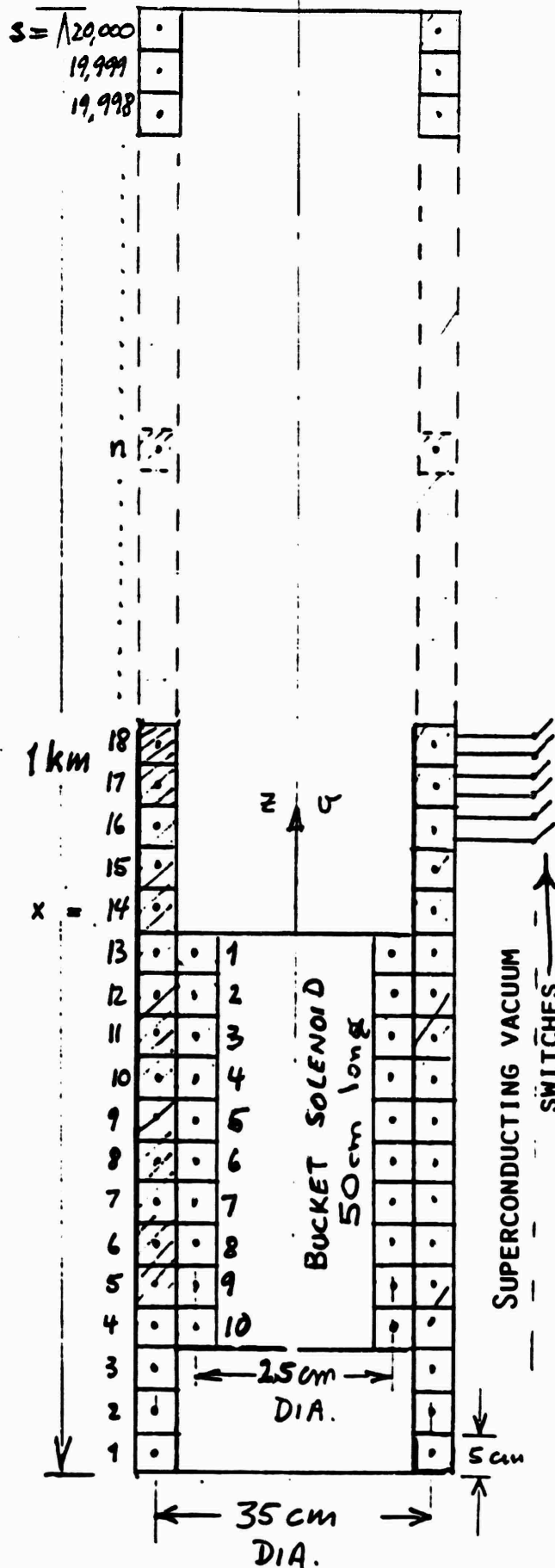


Fig. 32

**SELF-ENERGIZED
SUPERCONDUCTING
ACCELERATOR**

CALIBER: 35 CM
LENGTH: 1 KM
DRIVE COILS: 20,000, EACH:
 5x5 CM CROSS SECTION
 2500 TURNS, 100 AMPS
 10 KA/CM² OVERALL
CURRENT DENSITY

BUCKET:

10 IDENTICAL COILS
 LENGTH: 50 CM
 MASS: 20 KG
STORED ENERGY: 1.375 x 10⁹ JOULE
EFFICIENCY: 80%
ACCELERATION: 5,000 GEE AVERAGE
FORCE: 100,000 KG-F
VELOCITY: 10.5 KM/S

APPENDIX A

THE DYNAMIC DEFORMATION OF PULSED CURRENT COILS

The Dynamic Deformation of Pulsed Current Coils

Author: Osa E. Fitch

Project Advisor: Dr. Henry Kolm

Subject: 16.62, Experimental Projects

Instructors: Professor W. R. Markey

Mr. A. R. Shaw

Date: May 14, 1960

Department of Aeronautics and Astronautics

Massachusetts Institute of Technology

Cambridge, Massachusetts 02139

The Dynamic Deformation of Pulsed Current Coils

Abstract

Thin coils made from aluminum and copper wire were pulsed with large amplitude currents, and the resulting plastic strains were measured. Two theories were tested against the experimental results, and it was found that one of the theories, the impulse model of coil deformation, predicted incorrect strain values, while the other theory, the steady-state-to-yielding model of coil deformation, predicted correct, but inaccurate values for the strain. The steady-state theory was found to be highly dependent on the yield stress of the material, which could not be measured accurately. In the course of the experiment three other modes of coil failure were observed that were not dependent on the coil's deformation: baking of the insulation on the windings, arcing between the windings, and blowing of the coil leads away.

I. Introduction

A. The need for understanding the dynamic behavior of thin coils.

This project was conducted with the Electro-magnetic Accelerator Group at the National Magnet Lab. Its purpose was to gain a theoretical understanding of the deformation of thin coils when pulsed with large currents. In this purpose I have been successful.

Thin coils (i.e. coils whose diameters are much greater than their winding thicknesses) were under test in this experiment because they are the most suitable for use in electro-magnetic accelerators. In order to optimize the design of these accelerators, the factors which contribute to coil failure and the relationships between them must be determined. To do this, a theory which adequately predicts the dynamic deformation of the coil in question is necessary. The coils in the accelerator are then optimized by designing them such that at the maximum acceleration of the accelerator, the coils are stressed just below failure.

B. The origin of forces operating on thin coils

The forces operating on thin coils are a consequence of the fact that current flowing in the windings of a coil creates a magnetic field. This then acts on the current which originally created it, producing a force tending to make the coil expand radially (i.e. such that the diameter of the coil increases). (See Figure 1). This force is opposed at least partially by the hoop-stress in the coil, or by the inertia of the coil as it is accelerated radially. A second form of deformation which affects long, solenoidal type coils is the buckling of the coil windings, and their subsequent collapse axially toward the center of the coil. This is caused by the magnetic field

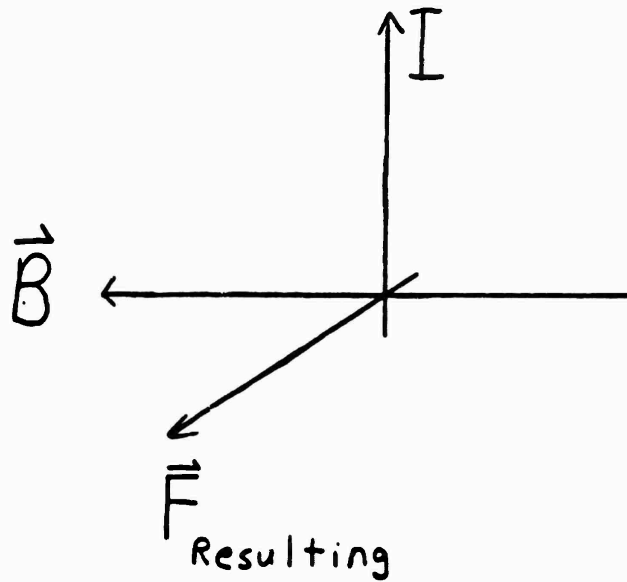
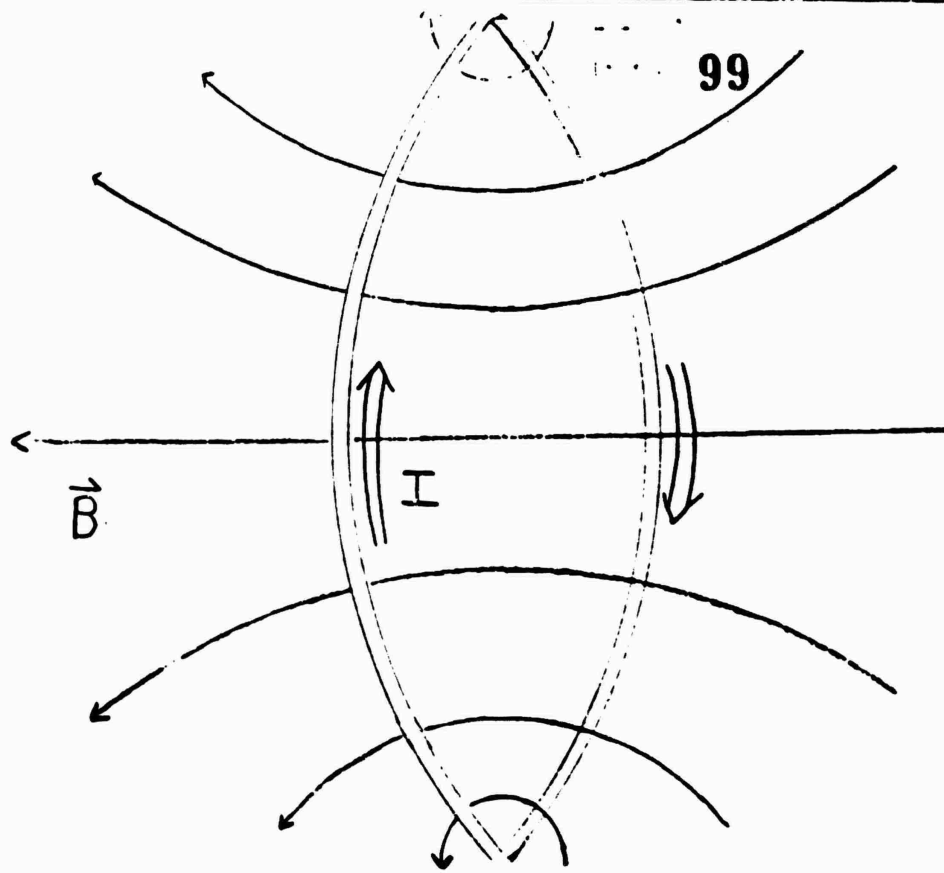


Fig. 1: MAGNETIC FIELD OF A CURRENT LOOP AND THE RESULTING FORCE THE COIL EXPERIENCES

traction between the coil windings (see Figure 2). In general this form of coil failure doesn't occur unless enough radial deformation is also present to give the windings room to collapse.

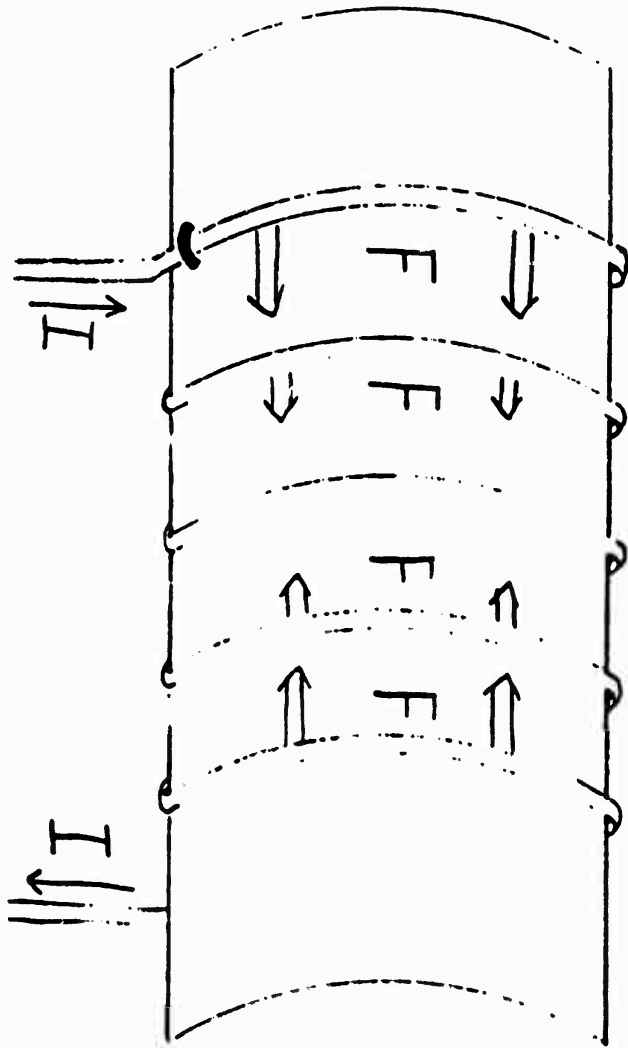
Three other types of coil failure were also observed in the course of these experiments: Arcing between the coil windings; baking of the winding insulation; and failure of the coil leads at their attachment points. In none of these cases was it necessary for the coil to deform significantly for the coil to fail.

C. Overview of the theory used in the prediction of the mechanical behavior of coils stressed to yielding and failure

For the theoretical prediction of coil behavior I assumed that the material of the coil windings behaved in a linear-elastic/ purely-plastic manner as illustrated in Figure 3. While none of the winding materials used in this experiment deform in exactly this fashion, it is a good first approximation to their behavior.

Using this model, two theories of dynamic coil deformation were tested against experiment. The first model tested was the impulse model, in which it was assumed that the length of the current pulse sent through the coil was much shorter than the time needed for the coil to respond to the pulse. Because the coil would not have sufficient time to expand and thereby generate the hoop-stresses needed to oppose the radial magnetic force, the coil would be accelerated radially. This would place kinetic energy into the windings of the coil which would then have to be stored elastically or dissipated plastically. The result is that the coil suffers some final plastic

Fig. 2: AXIAL FORCE ON A SOLENOID



σ
(Stress)

101

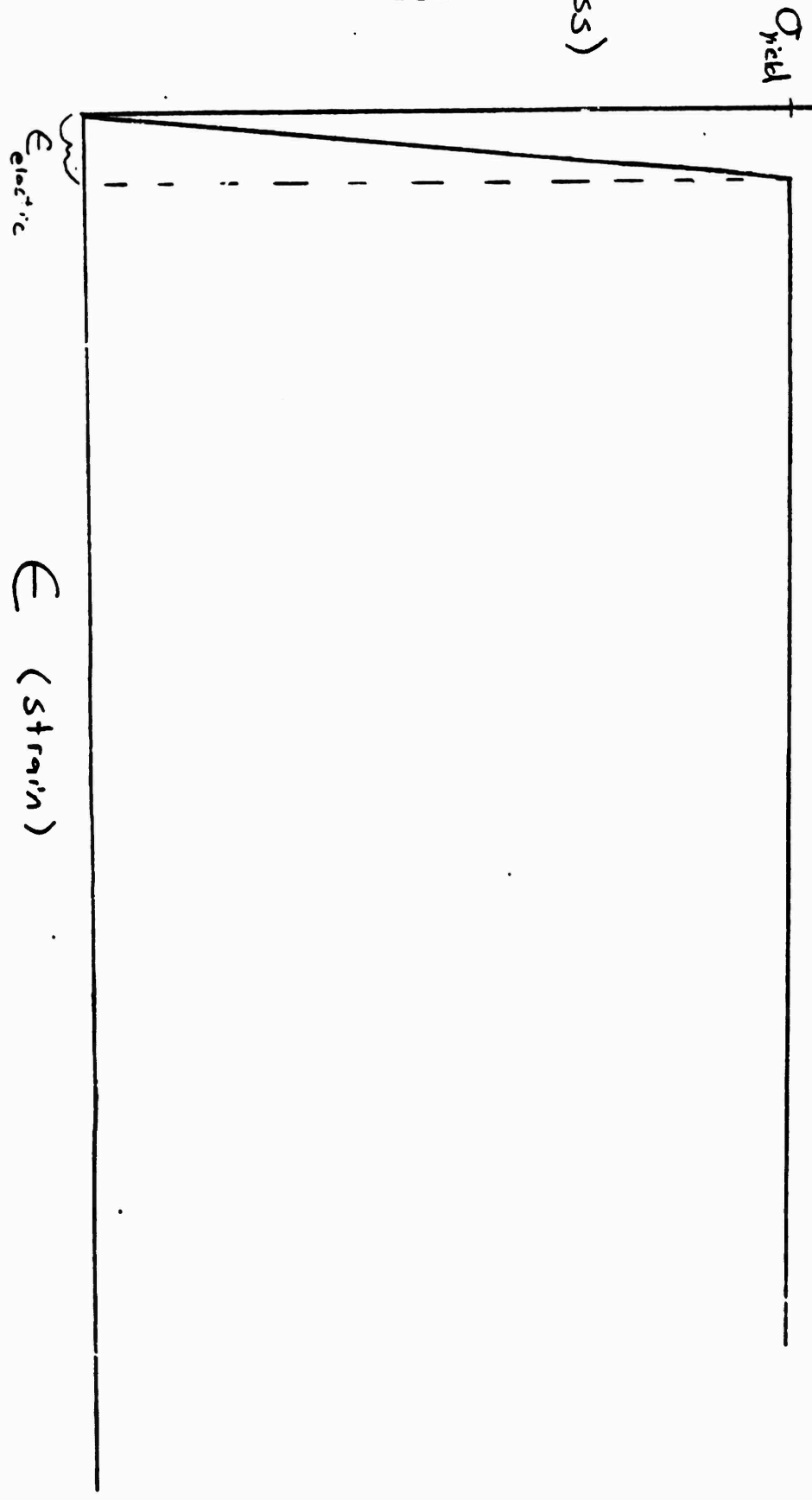


Fig.3: Perfectly Elastic / Purely Plastic Stress vs. Strain Curve

deformation, which could then be measured empirically.

The second model tested was the steady-state-to-yielding model, in which it was assumed that the length of the current pulse sent through the coil was much longer than the time needed for the coil to respond to the pulse. The coil would expand slowly (compared with what it was capable of doing) and oppose the outward-radial magnetic force with the hoop-stress in the coil windings. This state of equilibrium would continue until the hoop-stress reached the yield stress of the material. At this point the difference between the outward-radial magnetic force and the opposing hoop-stress force would accelerate the coil. When the outward-radial magnetic force fell below the value of the opposing hoop-stress force, the difference would decelerate the coil until it came to rest. This acceleration from rest followed by deceleration again to rest occurs in the plastic strain region. It leads to some final plastic deformation of the coil, which is what was measured in the experiment.

Finally, for all of the tests with long, solenoidal coils, I approximated the magnetic field inside as being the same as that for an infinite solenoid. For the tests with short coils, I approximated the magnetic field at the center as being the same as that for a single-loop coil, with an appropriate current flowing in it. The current for the single-loop approximation was taken as the number of turns making up the short coil times the current in the short coil. The magnetic field near the windings of the short coil was taken as twice that at the center of the coil.

D. The limitations of this study

Due to the lack of time, I was not able to do any tests with coils that had been externally reinforced and I was able to do very few tests with coils whose windings had been potted in epoxy. The experiments were performed primarily using totally unreinforced coils made from 0.10 inch round aluminum wire, 0.10 inch square copper wire, and 0.025 inch round copper wire. In addition, two tests were done using 0.025 inch round copper/ niobium-titanium composite wire, normally used as a super-conductor, but in this instance used only for its high tensile strength.

II. Theoretical analysis of the pulsed-coil system

A. The system as an RLC electrical circuit

Figure 4 shows a schematic diagram of the test circuit. Initially, the capacitor bank is charged to an initial voltage V_0 , which it holds until the SCR (silicon controlled rectifier) is fired by the trigger circuit. The dashed box is the test coil, which is taken to contain an ideal inductor and an ideal resistor. The diode across the test coil "crowbars" the circuit to prevent the capacitor voltage from swinging more negative than -0.5 volts. The entire resistance in the circuit, R , is taken to be the DC resistance of the coil, the entire inductance in the circuit, L , is taken to be the inductance of the coil and the entire capacitance in the circuit, C , is taken to be the capacitance of the capacitor bank. Using this model (and assuming the diode is switched off), the equation which governs the current, I , in the circuit is

$$\frac{d^2 I}{dt^2} + \frac{R}{L} \frac{dI}{dt} + \frac{I}{LC} = 0.$$

This equation has three solutions, depending on whether the system is lightly damped, heavily damped, or critically damped. For light damping,

$$I = \frac{V_0}{L \sqrt{\frac{1}{LC} - \left(\frac{R}{2L}\right)^2}} e^{-\left(\frac{R}{2L}\right)t} \sin \sqrt{\frac{1}{LC} - \left(\frac{R}{2L}\right)^2} t$$

which has its maximum value at

$$t_{max} = \frac{1}{\sqrt{\frac{1}{LC} - \left(\frac{R}{2L}\right)^2}} \tan^{-1} \left[\frac{\sqrt{\frac{1}{LC} - \left(\frac{R}{2L}\right)^2}}{\left(\frac{R}{2L}\right)} \right].$$

For heavy damping,

$$I = \frac{V_0}{L \sqrt{\left(\frac{R}{2L}\right)^2 - \frac{1}{LC}}} e^{-\left(\frac{R}{2L}\right)t} \sinh \sqrt{\left(\frac{R}{2L}\right)^2 - \frac{1}{LC}} t$$

which has its maximum value at

$$t_{max} = \frac{1}{\sqrt{\left(\frac{R}{2L}\right)^2 - \frac{1}{LC}}} \ln \left(\frac{\frac{R}{2L} + \sqrt{\left(\frac{R}{2L}\right)^2 - \frac{1}{LC}}}{\frac{R}{2L} - \sqrt{\left(\frac{R}{2L}\right)^2 - \frac{1}{LC}}} \right).$$

For critical damping,

$$I = V_0 C \left(\frac{R}{2L}\right)^2 t e^{-\left(\frac{R}{2L}\right)t}$$

which has its maximum value at

$$t_{max} = \frac{2L}{R}.$$

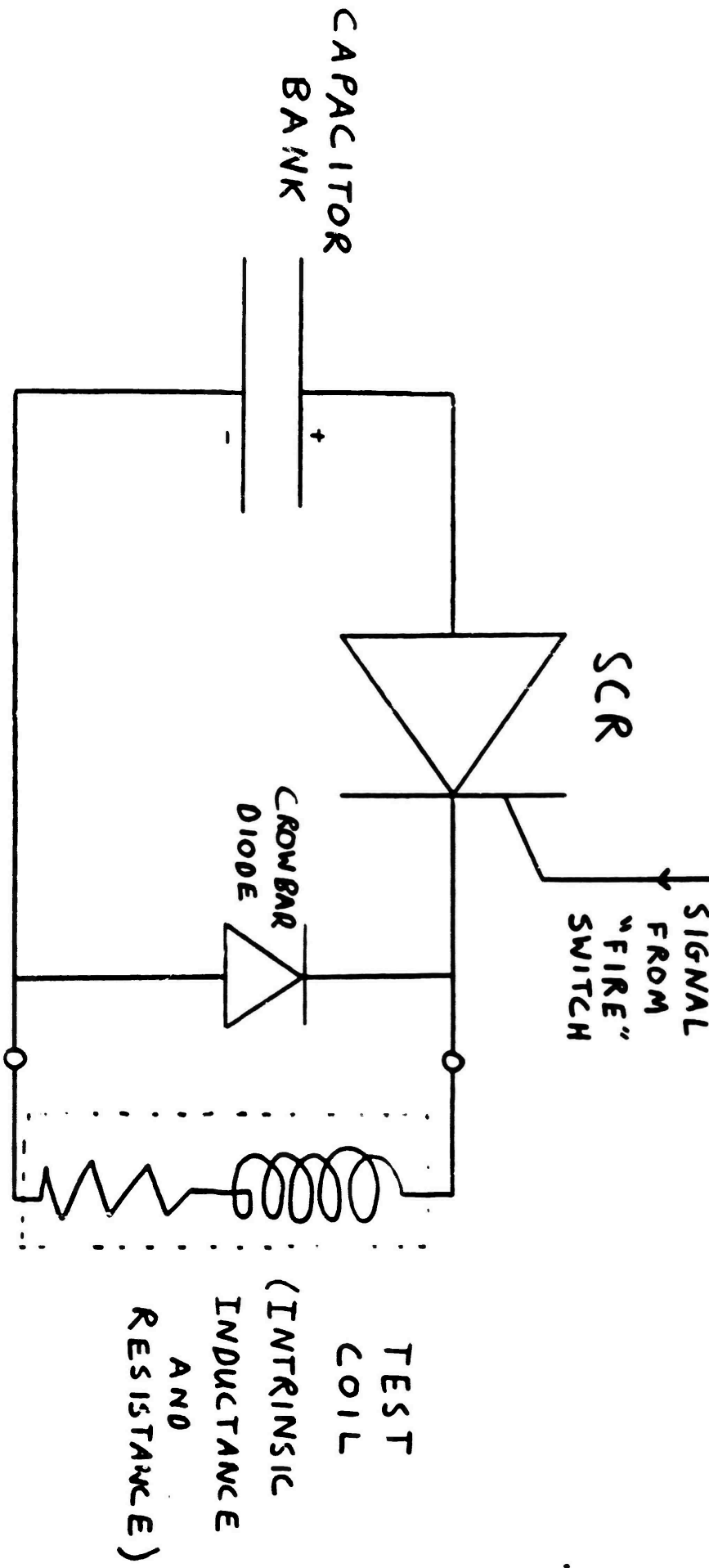


Fig. 4 : SCHEMATIC OF TESTING CIRCUIT

Theoretically, critical damping occurs at only one point, i.e. when $(R/2L) - 1/LC = 0$. In practice, it is convenient to use the critically damped formulae whenever $(R/2L) - 1/LC \approx 0$, since using either the lightly damped or heavily damped equations would result in a loss of accuracy. Normally however, either the lightly damped or the heavily damped equations are used.

B. Factors related to coil geometry

The magnetic field, B , produced by a coil depends on the geometry of the coil and is proportional to the current flowing in the coil windings.

For a coil long enough to be treated as an infinite solenoid, the field is

$$B = \frac{\mu_0 N I}{l}$$

where N is the total number of turns in the coil, l is the total length of the coil, and $\mu_0 = 4\pi \times 10^{-7}$ MKS units. This formula begins to be a good approximation of the magnetic field generated by the coil when the coil length, l , becomes larger than the inside diameter of the coil.

For coils whose length is less than about one third of their diameter, a better formula for the magnetic field is,

$$B_{\text{center}} = \frac{N \mu_0 I}{2 R_0}$$

where R_0 equals one half of the diameter of the coil. Unlike long, solenoidal coils, the magnetic field of short coils near the windings is not approximately equal to the field at the center of the coil. For the generalized short coil case, I have taken the field near the windings to be twice that of the field in the center.

For coils with multiple layers of windings I used the principle of superposition. For the inner layer of windings all of the above formulas hold. To find the magnetic field on the inner surface of the next layers, the same formulas may be used except that N must be replaced by the total number of

turns minus the number of turns contained in all lower layers, and R_0 may have to be changed to take into account the finite thickness of the layers.

The magnetic pressure that a single-layer coil must withstand is,

$$P = \frac{B^2}{2\mu_0},$$

and which must be applied separately to each layer of a multi-layer coil.

When this is done, an average pressure, \bar{P} , can be defined as

$$\bar{P} = \frac{1}{n} \sum_{i=1}^n P_i = \left[\frac{1}{n} \sum_{i=1}^n \left(\frac{n+1-i}{n} \right)^2 \right] P = KP; \quad \left[K \equiv \left(\frac{1}{n} \sum_{i=1}^n \left\{ \frac{n+1-i}{n} \right\}^2 \right) \right]$$

where P is the pressure just inside the innermost layer of the coil. This expression is valid for all multi-layer coils with n layers where the thickness of the windings is small compared to R_0 so that it can be neglected.

In order to decide whether the impulse theory or the steady-state theory is a more valid description of the coil's behavior, the coil's response time, which corresponds to the ringing period, must be determined. By using a radial force balance and applying Newton's law, the equation which describes a coil's deformation is,

$$\ddot{\epsilon} + \frac{E}{\rho R_0^2} \epsilon + \frac{KP}{\rho(R_0/A)},$$

provided that the deformation of the coil remains in the elastic range, and where ϵ is strain, E is Young's modulus, ρ is density, A is the cross-sectional area of the wire used to wind the coil, and σ is the diameter of a single winding measured along the axis of the coil. For a freely ringing coil $P=0$, and

$$\omega = \sqrt{\frac{E}{\rho R_0^2}} \quad \text{giving,}$$

$$T = 2\pi R_0 \sqrt{\frac{\rho}{E}}.$$

To determine the more valid theory then, compare t_{max} to $T/4$: If t_{max} is long compared to $T/4$, then the pulse is long enough so that the coil can respond according to the steady state theory; if t_{max} is short compared to $T/4$, then the coil cannot respond fast enough to keep up with the pulse, and the impulse theory should be used.

C. The linear-elastic/ purely-plastic model of material behavior

1. The steady-state-to-yielding model of coil deformation.

If t_{max} is long compared to $\sqrt{1/4}$, then the steady-state model should be used to describe coil deformation. In all of the experiments that I conducted, this was the case. For the elastic region then, the strain is changing rather slowly, such that $\ddot{\epsilon} \approx 0$. This leads to

$$\epsilon_{linear} \approx \frac{\delta R_0}{EA} k P.$$

In general,

$$\epsilon_{linear} = \left(\frac{\delta R_0 k}{2EA\mu_0} \right) B^2,$$

which is valid for all coils under the steady-state theory, having neglectable winding thicknesses.

The linear strain relation is valid until the yield stress of the material is reached. The maximum pressure that the coil can withstand without deforming plastically is

$$P_{max} = \frac{\sigma_{yield} A}{\delta R_0 k}.$$

Any pressure above this level will cause plastic deformation in the material, which will lead to a non-neglectable $\ddot{\epsilon}$. Because there is no longer an elastic term, due to perfect plasticity,

$$\ddot{\epsilon}_{plastic} + \frac{\sigma_{yield}}{\rho R_0^2} = \frac{P k}{\rho \left(\frac{\delta}{2}\right) A}, \quad \text{which becomes}$$

$$\ddot{\epsilon}_{plastic} = \frac{(P - P_{max}) k}{\rho \left(\frac{\delta}{2}\right) A}.$$

This equation can be integrated twice, but only if the limits of integration are known. It is desired to integrate from the moment that the pressure exceeds P_{max} , since this is when both the acceleration and the plastic deformation begin, to the moment when $\dot{\epsilon}_{plastic}$ is next zero, since this is when the plastic deformation ends. By setting the pressure equal to P_{max} , $t_{0,plastic}$, the time at which plastic deformation begins, can be found.

$$P_{\max} = \frac{\sigma_{\text{yield}} A}{\int R_0 K} = \frac{B_{\text{plastic}}^2}{2\mu_0}$$

$$B_{\text{plastic}} = \sqrt{\frac{2\mu_0 \sigma_{\text{yield}} A}{\int R_0 K}}$$

If the coil is a long solenoid,

$$B = \frac{\mu_0 N I}{L} \quad \text{and}$$

$$I_{\text{plastic}} = \frac{L}{N} \sqrt{\frac{2\sigma_{\text{yield}} A}{\mu_0 \int R_0 K}}$$

If the coil is short,

$$B_{\text{ind}} = \frac{N \mu_0 I}{R_0} \quad \text{and}$$

$$I_{\text{plastic}} = \frac{L}{N} \sqrt{\frac{2\sigma_{\text{yield}} A}{\mu_0 \left(\frac{R_0}{L}\right) K}}$$

For light or heavy damping define

$$\Psi = \frac{L}{V_c} \sqrt{\left|\left(\frac{R}{2L}\right)^2 - \frac{1}{LC}\right|} I_{\text{plastic}}$$

For light damping solve numerically

$$\left(e^{-\left(\frac{R}{2L}\right)t_{\text{plastic}}}\right) \sin \sqrt{\frac{1}{LC} - \left(\frac{R}{2L}\right)^2} t_{\text{plastic}} = \Psi, \quad \text{to find } t_{\text{plastic}}$$

For heavy damping solve

$$\left(e^{-\left(\frac{R}{2L}\right)t_{\text{plastic}}}\right) \sinh \sqrt{\left(\frac{R}{2L}\right)^2 - \frac{1}{LC}} t_{\text{plastic}} = \Psi, \quad \text{to find } t_{\text{plastic}}$$

For critical damping define

$$\Psi = \frac{L}{V_c} \left(\frac{2L}{R}\right) I_{\text{plastic}},$$

and solve numerically

$$\left(\frac{R}{2L}\right)t_{\text{plastic}} e^{-\left(\frac{R}{2L}\right)t_{\text{plastic}}} = \Psi, \quad \text{to find } t_{\text{plastic}}$$

Once t_{plastic} has been found, $\dot{\epsilon}$ at a general point in time is found by integrating $\dot{\epsilon}$ from t_{plastic} to t . The resulting equation is then set equal to zero and a numerical solution for t_{end} is found. Finally, the general equation for $\dot{\epsilon}$ is integrated from t_{plastic} to t_{end} to give the final resulting plastic deformation.

2. The impulse model of coil deformation. If t_{max} is short compared to τ_4 , then the impulse model should be used to describe coil deformation. Since the pulse is assumed to be over before the coil has deformed significantly the equation describing the linear strain is

$$\ddot{\epsilon}_{linear} \approx \frac{\rho \kappa}{\rho (\frac{R_0}{2}) A}$$

To find the final plastic strain, calculate the kinetic energy which the impulse imparts to the coil and set it equal to the energy stored elastically and dissipated plastically. The impulse imparted to the coil is

$$\int_0^{\tau} P dt = \left(\frac{R_0}{2}\right) \frac{A \rho}{\kappa} \dot{\epsilon}_0,$$

which allows an initial strain-velocity, $\dot{\epsilon}_0$, to be found,

$$\dot{\epsilon}_0 = \left(\frac{2}{R_0}\right) \frac{\kappa}{A \rho} \int_0^{\tau} P dt.$$

The kinetic energy associated with this velocity is

$$E = \frac{1}{2} R_0 \frac{\rho^2 \kappa^2}{A \rho} \left[\int_0^{\tau} P dt \right]^2,$$

which we then set equal to the sum of the final stored elastic-strain energy and the dissipated plastic-strain energy. So,

$$E = \frac{R_0 A (\sigma_{yield})^2}{2 E} + \sigma_{yield} A R_0 \epsilon_{plastic}$$

which leads to the final expression for the plastic deformation of the coil,

$$\epsilon_{plastic} = \frac{\rho^2 \kappa^2}{2 A^2 \rho \sigma_{yield}} \left[\int_0^{\tau} P dt \right]^2 - \frac{\sigma_{yield}}{2 E}$$

valid for the impulse model. The τ in the upper limit of the impulse integral is evaluated as ∞ if the system is either heavily or critically damped, and it is evaluated as the first zero of the lightly damped current equation. This is found by the same method of solution as $t_{0,plastic}$ was found for the lightly damped steady-state case with the exception that ψ is set to zero.

III. Experimental procedures

The method I used to test the deformation of coils was extremely simple. I did not receive the strain-gauges that were small enough to mount upon 0.10 inch diameter wire in time to do any testing with them, so I used a cruder method of measuring plastic strain. Before winding a coil, I made two marks a measured distance apart on the wire. After pulsing the coil I unwound it and measured the new distance between the marks. The difference between the new and old distances was taken and divided by the old distance. This gave the measured plastic strain suffered by the coil due to the pulse.

Using this method I was unable to measure strains smaller than about 0.20% accurately. Because I did not want to waste the test coil I had prepared for measurement by pulsing it at a voltage which would produce strains that I could not measure, I used two coils for my test shots. The coils were wound as identically as possible, so that all of their parameters would be the same. The first coil was pulsed repeatedly at regularly increasing initial voltages until it was seen to yield. The second coil was then pulsed at a slightly lower initial voltage (since it would be cooler and therefore conduct more current), and afterward unwound, and the strain measured.

The current trace was observed for all shots using a Nicolet digital oscilloscope connected across a calibrated shunt. In this way the maximum current in the circuit could be measured directly, and the shape of the current vs. time function could be compared with theoretical predictions.

IV. Results

A. Initial testing: Coils wound from 0.10 inch round aluminum wire

The initial tests of my experiment used coils wound from 0.10 inch diameter round aluminum wire. They were hand wound as tightly and as uniformly as possible around sections of wooden dowel 3 inches in diameter. The leads were secured by passing the wire through a hole drilled along a chord of the cylinder, looping it back around and through the hole a second and final time. They were all single layer coils with no external reinforcement or epoxy.

The first test of an aluminum coil used a coil with 34 turns and a length of 8.6 cm. After several pulses at low voltages (approximately 25 volts) to insure that all of the circuitry was working properly, the initial voltage on the capacitor bank was raised to 1000 volts. The coil, which was inside a thick plywood box for safety, was pulsed at this voltage and failed through radial deformation, axial buckling of the windings, and arcing through the insulation on the windings. The radial deformation was the primary mode of failure, and the other modes came about as a result of it. The coil actually ruptured (primarily due to melting of the windings caused by the necked-down aluminum being unable to handle the current flowing through it) in five separate places, but of the pieces which were intact, the plastic strain was approximately 100% (with 20-30% uncertainty). (See Table 1).

The second test of an aluminum coil used a coil with 44 turns and a length of 11.2 cm. The arcs on the middle 20 turns of the coil initially separated 5.12 meters of wire. First, a similar coil of 50 turns was pulsed at increasing voltages until it was observed to yield at an initial voltage of 375 volts. The 44 turn coil was pulsed initially at 20 volts for an

Test	Wire Used	Type of Coil	Voltage	R/L/C (obs./prev./fund.)	Peak stress N/m ²	study-state model predicted % strain	Measured strain %	Failure Mode
①	0.10 inch Round Aluminum	34 Turns Single layer long solenoidal	1000 V	.055 6.3x10 ⁻⁵ .165	1.84x10 ⁷	5.06x10 ⁻⁶ %	100%	Radial Deformation Arcing
					2.72x10 ⁷	3.30x10 ⁻⁶ %		
					3.33x10 ⁷	2.63x10 ⁻⁶ %		
②	0.10 inch Round Aluminum	44 Turns Single layer long solenoidal	325 V (429 V)	.101 2.7x10 ⁻⁵ .165	1.84x10 ⁷	5.589 %	0.96 %	Radial Deformation
					2.72x10 ⁷	14.4 %		
					3.33x10 ⁷	No plastic strain		
③	0.10 inch Square Copper	20 Turns Double layer 5 Turns/layer Short	260 V	.010 1.12x10 ⁻⁵ .165	3.00x10 ⁷	6.75 %	1.4 %	Radial Deformation Lead Failure
					4.24x10 ⁷	19.63 %		
					5.17x10 ⁷	27.0 %		
④	0.025 inch Round copper	20 Turns Double layer 10 Turns/layer Short	118 V	.309 5.75x10 ⁻⁵ .165	3.00x10 ⁷	No plastic strain	0.0 %	Baking of the insulation
					4.24x10 ⁷	No strain		
					5.17x10 ⁷	"		
⑤	0.025 inch Round copper	20 Turns Double layer 10 Turns/layer Short Power in Epoxy	2000 V	.309 5.75x10 ⁻⁵ 1.08x10 ⁻³	5.00x10 ⁷	1.54x10 ⁻⁶ %	Undetermined	Inner winding Blow-out and Rupture
					4.24x10 ⁷	1.17x10 ⁻⁶ %		
					5.17x10 ⁷	8.29x10 ⁻⁵ %		
⑥	0.025 inch Superior insulation	20 Turns Double layer 10 Turns/layer Short Power in Epoxy	2000 V	"	7.69x10 ⁷	5.63x10 ⁻⁵ %	0.0 %	Arcing
					3.00x10 ⁷	No strain		
⑦	0.025 inch Superior insulation	20 Turns Double layer 10 Turns/layer Short Power in Epoxy	2000 V	"	?	?	0.0 %	Arcing

TABLE 1:
Experimental Results

equipment and connection check, and then it was pulsed at 325 volts. As expected it yielded, giving a plastic strain of $9.6 \times 10^{-3} \pm 2 \times 10^{-3}$, or about 1% strain. (See table 1). In this test the measured maximum current was 3700 amps, whereas theory predicted a maximum current of only 2057 amps, for an initial capacitor bank voltage of 325 volts. I do not know what caused this discrepancy, but in order to give the rest of the theoretical analysis as much chance at accuracy as possible, I decided to use the empirical current value. The theoretical initial voltage corresponding to this value of maximum current was 429 volts, which was what I used.

B. Tests of copper coils

The first copper coil test was with a coil made of 0.10 inch square copper wire, wound in two layers of 5 turns each. Its total length was 1.5 cm, and it was not epoxied or otherwise externally reinforced. Like the aluminum coils, the copper coils were also wound around a wooden dowel 3 inches in diameter. For this coil under test the leads were connected to a terminal block which was mounted to the wood. The terminal block served to hold the leads of the coil in place and also as an attachment point for the leads coming from the capacitors. The first coil was pulsed at successively increased initial voltages until at a voltage of 200 volts some slight deformation was detected. In order to obtain more deformation the initial voltage was increased to 300 volts, and when the capacitor bank was triggered the leads from the capacitor bank to the terminal block blew off. By insuring that the leads to the second coil were on very tightly, we were able to fire a 200 volt shot, and get a plastic strain of $1.4 \times 10^{-2} \pm 3 \times 10^{-3}$ or slightly

more than 1% strain. (See table 1). In this shot the measured maximum current was 11640 amps, with a theoretical prediction of 15648 amps for an initial voltage of 260 volts.

Four other copper coil shots were done, none of them giving useable results. Those results are listed in Table 1. The first of these tests was of a coil wound from 0.025 inch round copper wire, having 2 layers of 10 turns each. It was not epoxied or externally reinforced, and its leads were secured to two separated terminal blocks, to which the capacitor leads were also secured. When this coil was pulsed, it was so heavily damped that the current largely heated the coil instead of deforming it radially. For an initial voltage of 110 volts the coil became so hot that the insulation failed by boiling and charring.

For the other three tests, a different capacitor bank was used, one which was capable of storing higher voltages and which had a smaller capacitance than the first bank. The smaller capacitance led to much lighter damping, and in fact made the system for the next three tests lightly damped. This also gave the system a much faster pulse, but not so fast that the steady-state model could not be used.

The next test was a coil identical to the previous one, except that its windings were potted in epoxy. It was pulsed at 500 volts, 1000 volts, and 1500 volts with no visible deformation. When it was pulsed at 2000 volts, a section of inner windings blew out and rumbled in the. Other than that, I could not detect any other deformation. I believe that the reason this coil was able to withstand pulsing at such high voltages is that the epoxy glued the windings together, and therefore prevented them from buckling, and that the epoxy glued the windings to the lead, spreading the forces over a much larger area than other wise would have been possible.

The last two tests used coils that were identical to the first two except that they were wound from 0.025 inch super-conductor wire, which consists of filaments of niobium-titanium potted in 0.025 inch thick copper wire. For my purposes I did not use this wire as a super-conductor, but as a composite having a tensile strength greater than that of copper alone. One of these coils was potted in epoxy, the other was no. Both failed at 2000 volts by arcing through their insulation. Again, I could not detect any radial deformation.

C. Yield stress measurements

In order to check the values I used for yield stress, I measured the yield stress for two of the materials, aluminum and copper, which I used in my experiment. Using a dial micrometer, I measured the deflections of measured pieces of wire in the testing machine as a function of the force applied to the wire. I defined σ_{yield} as being that stress at which the stress-strain curve first diverged from linearity. For the aluminum, of the three different valid measurements that I made, the yield stresses were $1.04 \times 10^7 \text{ N/m}^2$, $2.72 \times 10^7 \text{ N/m}^2$, and $3.33 \times 10^7 \text{ N/m}^2$. For the copper, as measured using the 0.10 inch square wire, the yield stresses were $3.00 \times 10^7 \text{ N/m}^2$, $4.24 \times 10^7 \text{ N/m}^2$, $5.17 \times 10^7 \text{ N/m}^2$, and $7.07 \times 10^7 \text{ N/m}^2$. My attempts to measure the yield stress of the 0.025 inch super-conducting wire were unsuccessful, and I was unable to find a tabulated value for it.

V. Discussion of results

The most important characteristic of the theory is its extreme sensitivity to yield stress. (See Figure 5). For predictions in the small strain region, an error on the order of 1% in the accuracy of the yield stress can cause double the predicted plastic strain. With the large scale uncertainties as to what the correct yield stress in our material is, and given the numerous factors, such as temperature and strain hardening, that can affect the value of the yield stress, accurate prediction of the amount of plastic strain becomes impossible with a model this simplified. The fact that the model is conceptually correct however, is shown by the bracketing of the empirical value for strain by the various predicted values using the different yield stresses.

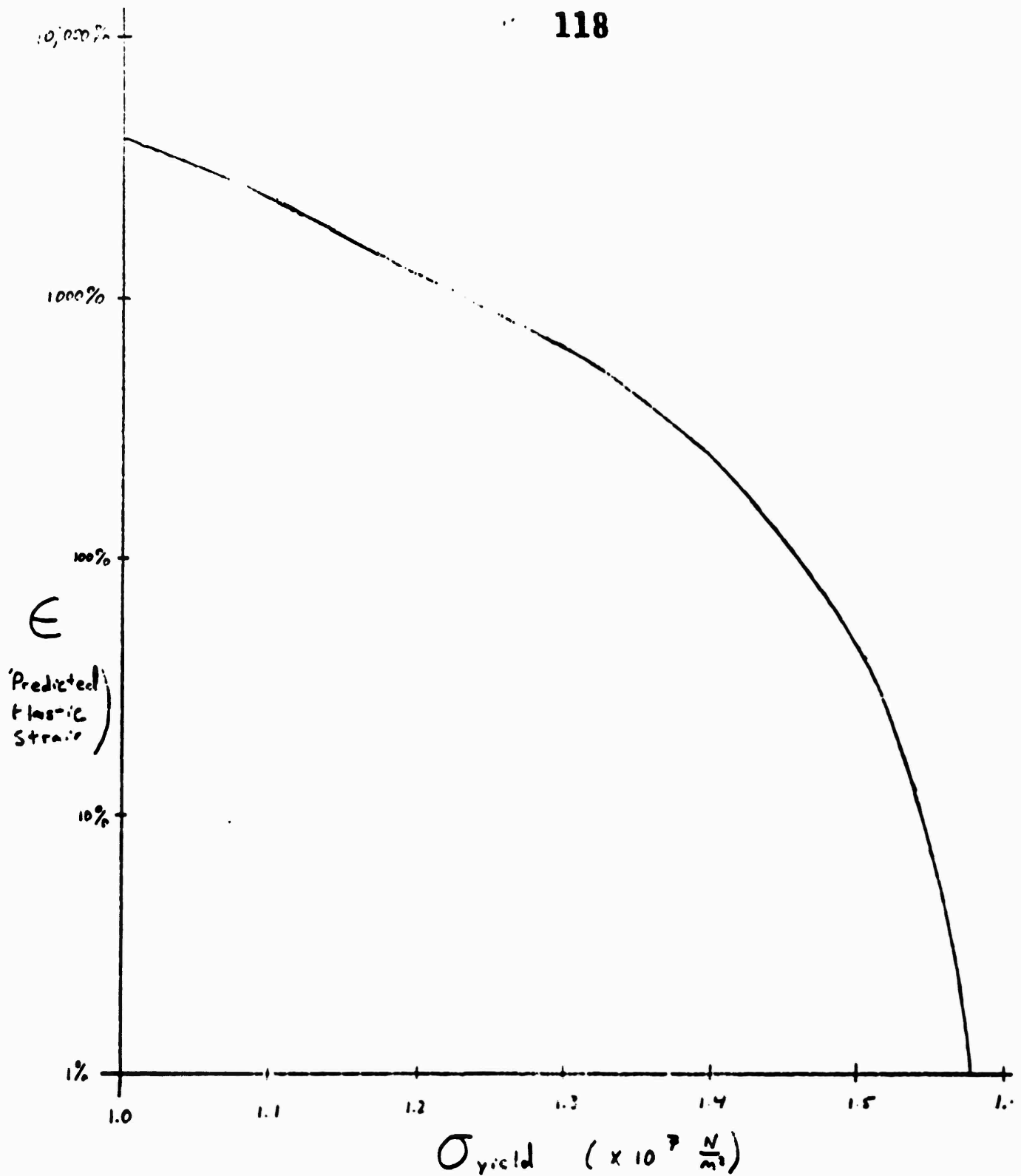


Figure 5: Predicted plastic strain as a function of varying the yield stress used as input to the theory. Plot is from predictions made for the second Aluminum coil at a voltage of 225 v.

VI. Conclusions

The steady-state-to-yielding model is a conceptually correct model of dynamic coil behavior, but one that does not allow accurate prediction of the final coil deformation due to inaccuracies in determining the yield stress in the coil material. However, the theory should be adequate to design and optimize coils, since it is desired to have zero plastic deformation after each shot. The impulse model will be rarely used, since it does not adequately predict coil behavior unless the pulse length is much less than the response time of the coil.

The steady-state model, on the other hand, is valid when the response time of the coil is much less than the pulse length, which is a situation that occurs much more frequently.

Further study in this area is recommended to investigate the effects of adding external reinforcement to the coils, and potting the windings in epoxy. Also the possible deformative effect of one coil pulsing near another coil should be investigated, although that was outside the area of study of this report.

APPENDIX B

THE SELF-ENERGIZED, SUPERCONDUCTING MASS DRIVER
AS A MEANS FOR LAUNCHING SPACE VEHICLES FROM EARTH1.0 INTRODUCTION

Rocket propulsion has become the established way of launching objects into deep space and into orbits around the earth. A possible alternative to this method of propulsion are electromagnetic accelerators. A major advantage of electromagnetic traction should be the more efficient use of energy because no fuel has to be hoisted into space. The penalty for this is the high velocity with which the projectile has to travel through the densest layers of the atmosphere.

At present it is by no means clear how trade-offs of this nature would influence the economics of space flight. Different concepts of electromagnetic accelerators may be envisaged, but this investigation deals only with one particular version. This is the coaxial superconducting mass driver in which the traction solenoid and the armature (bucket) coil carry persistent supercurrents. The analysis does not go beyond establishing electrodynamic ^u feasibility.

A primary objective of the design is to use a long superconducting solenoid, at one and the same time, as fast access energy store and drive coil. Other electromagnetic earth launchers have been proposed. They require specially provided energy storage devices dedicated to the launch facility and existing in addition to the drive coils. Since the energy has to be made available in the short time span of a few ^{or less,} seconds, not all conventional methods of energy storage are suitable for earth launchers. The most attention has been given to electrostatic capacitors and flywheels in homo-

polar generators. Storage devices of this kind are likely to be the most costly items of an electromagnetic accelerator. They would be eliminated if it should prove possible to convert most of the magnetic energy stored by a long solenoid into kinetic energy of the projectile.

The following analysis aims at establishing concept feasibility without attempting design optimization. It should therefore be easy to improve the performance and economics of the all-superconducting mass driver by further design studies.

2.0 ENERGY CONVERSION PROCESS

2.1 Energy Storage

The electromagnetic accelerator configuration to be examined is shown in fig.1. It employs a 1000 m long vertical solenoid of 5 cm thickness and 30 cm bore. It is assumed that the solenoid and most of the accelerator components would be set up in a vertical mine shaft. The traction solenoid consists of 20,000 identical square-section coils of 5 x 5 cm winding cross-section. Each coil is wound with 2500 turns of 1 x 1 mm conductor cross-section.

For analytical purposes, each drive coil will be treated as a circular filament coinciding with the center turn of the coil and carrying a current equal to the ampere-turns of the coil. A single 5 x 5 cm section coil serves for acceleration of the payload. No clearances are shown on fig.1 between drive and armature coils, but they may easily be introduced by assuming the winding cross-sections to be reduced to, say, 4 x 4 cm with a corresponding increase in current density. This preserves the location of all central filament rings by which the coils are represented in the mutual inductance analysis.

All inductance calculations have been carried out in compliance with the formulas provided by Grover, "Inductance Calculations". The selfinductance of the traction solenoid shown in fig.1 comes to

$$L_S = 2.75 \times 10^5 \text{ H} = 2.75 \times 10^{14} \text{ cm} \quad \dots (1)$$

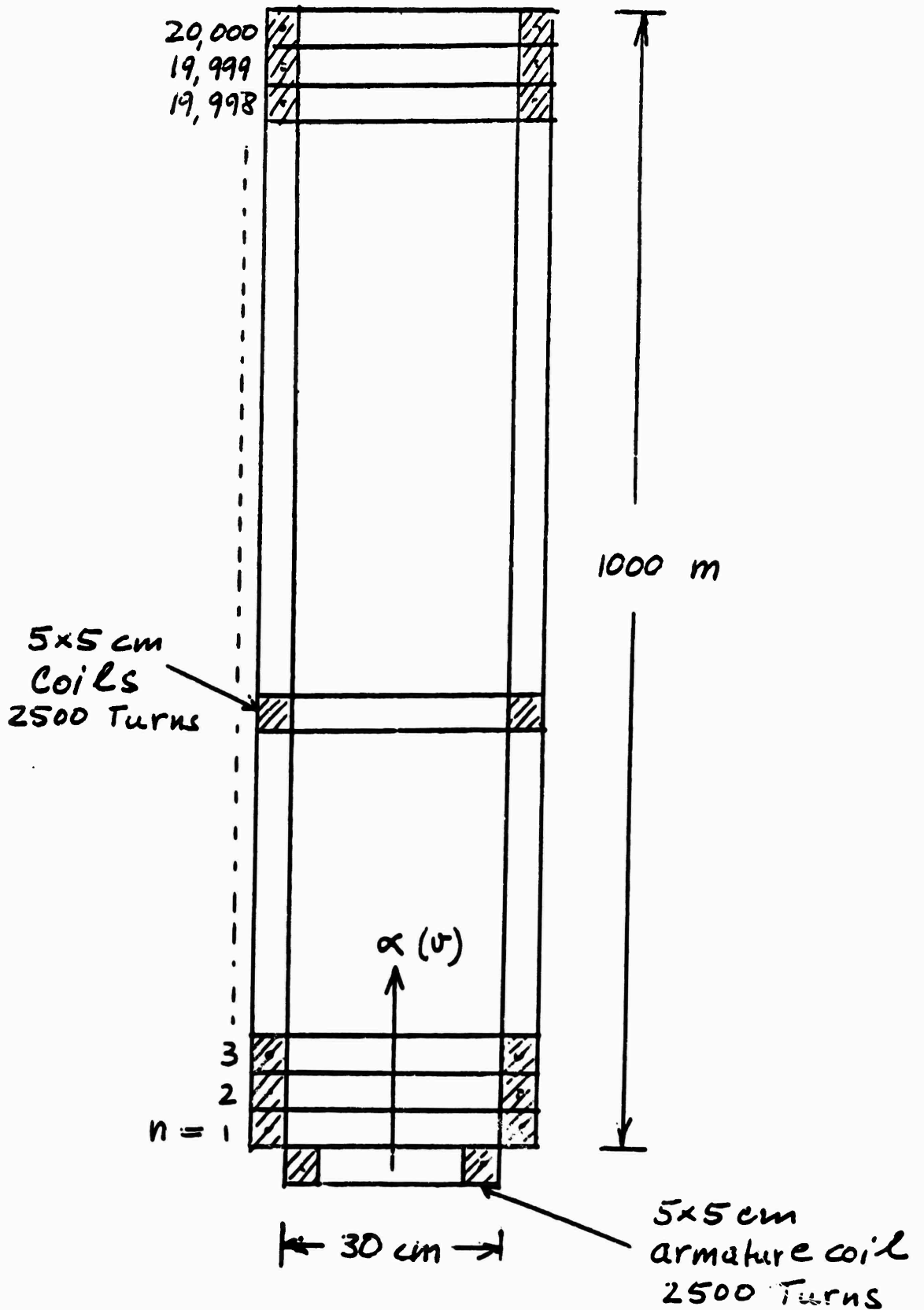


Fig. 1 Dimensions of traction solenoid and armature coil

With an overall current density in the solenoid of 10,000 A/cm², the current in each turn of each individual drive coil is

$$i_s = 100 \text{ A} \quad \dots(2)$$

This results in a maximum magnetic field strength at the center of the solenoid of

$$B_{\max} = 6.3 \text{ T} \quad \dots(3)$$

The total magnetic energy stored by the solenoid is

$$E_0 = (1/2)L_s i_s^2 = 1.375 \text{ GJ} \quad \dots(4)$$

Assuming that 80 percent of the stored energy will be converted to kinetic energy, the remainder being dissipated by induced drag currents, mechanical friction and arc heating, this leaves 1.1 GJ for mass acceleration.

Let the total projectile mass be 20 kg, then the final velocity of the payload would be

$$v = \sqrt{1.6E_0/m} = 10.5 \text{ km/s} \quad \dots(5)$$

where m is the accelerated mass. Hence a one kilometer long coaxial superconducting mass driver has the potential of accelerating useful payloads to earth escape velocity, which exceeds 10 km/s by an amount depending on the aerodynamics of the projectile. Much more magnetic energy may be stored in longer solenoids of greater diameter. The dimensions of the accelerator of fig.1 were chosen to obtain some idea of just how small a useful electromagnetic earth launcher could be.

For the projectile to reach the final velocity of 10.5 km/s over the length of 1 km, the average acceleration must be

$$\bar{a} = v^2/2l = 55,125 \text{ m/s}^2 = 5619 \text{ g} \quad \dots(6)$$

where g is the acceleration due to gravity. The average force required to satisfy (6) is

$$F = m\bar{a} = 112,385 \text{ kg} \quad \dots(7)$$

The axial stress on the solenoid and armature coil resulting from the acceleration force is

$$\bar{\sigma}_s = F/(\pi/4)(40^2 - 30^2) = 204 \text{ kg/cm}^2 = 2907 \text{ psi} \quad \dots(8)$$

$$\bar{\sigma}_a = F/(\pi/4)(30^2 - 20^2) = 286 \text{ kg/cm}^2 = 4068 \text{ psi} \quad \dots(9)$$

The magnitude of these stresses seem acceptable for superconducting windings. The weakest metal component of the superconductor would be the backing material. High purity aluminum can operate safely at 5000 psi at ambient temperature and 10,000 psi at helium temperatures. The electrical insulation of the 1 x 1 mm superconductor wires will be compressed by the axial stresses. Not many dielectric materials are capable of withstanding the high compressive stresses which will arise, particularly, in the solenoid. Designers of all kinds of superconducting magnets face the same difficulty. Most reliance is being placed on fiberglass reinforced epoxy (G10) in sheet or spacer form, and the alumina coating of anodized aluminum.

2.2 Current Transfer to the Armature Coil

A long superconducting solenoid utilizing its stored energy can accelerate the armature coil only by attraction and not by repulsion. Attraction is in any case more desirable for lateral stability of the projectile in the confined space of the solenoid bore. For the attraction force to be reasonably constant over the full length of the projectile flight through the solenoid, the portion of the solenoid behind the projectile has to be de-energized or quenched as the armature coil progresses. The most promising method of quenching the persistent current in the drive coil through which the armature passes appears to be current interruption by a vacuum circuit breaker.

The operation of any one of a battery of circuit breakers arranged alongside the traction solenoid has to be carefully timed to coincide with the passage of the armature coil. A possible switching arrangement is illustrated in fig.2. The vacuum circuit breakers make and break persistent current contacts between a superconducting return conductor and taps on the traction solenoid. For the armature position indicated in fig.2, contacts (a) have to close before contacts (b) are opened.

The process of current interruption will induce emf's in the neighboring part of the traction solenoid and in the armature coil. The armature emf helps to maintain the armature current and this is an essential feature of the superconducting accelerator concept. But additional current in the solenoid would be undesirable as this

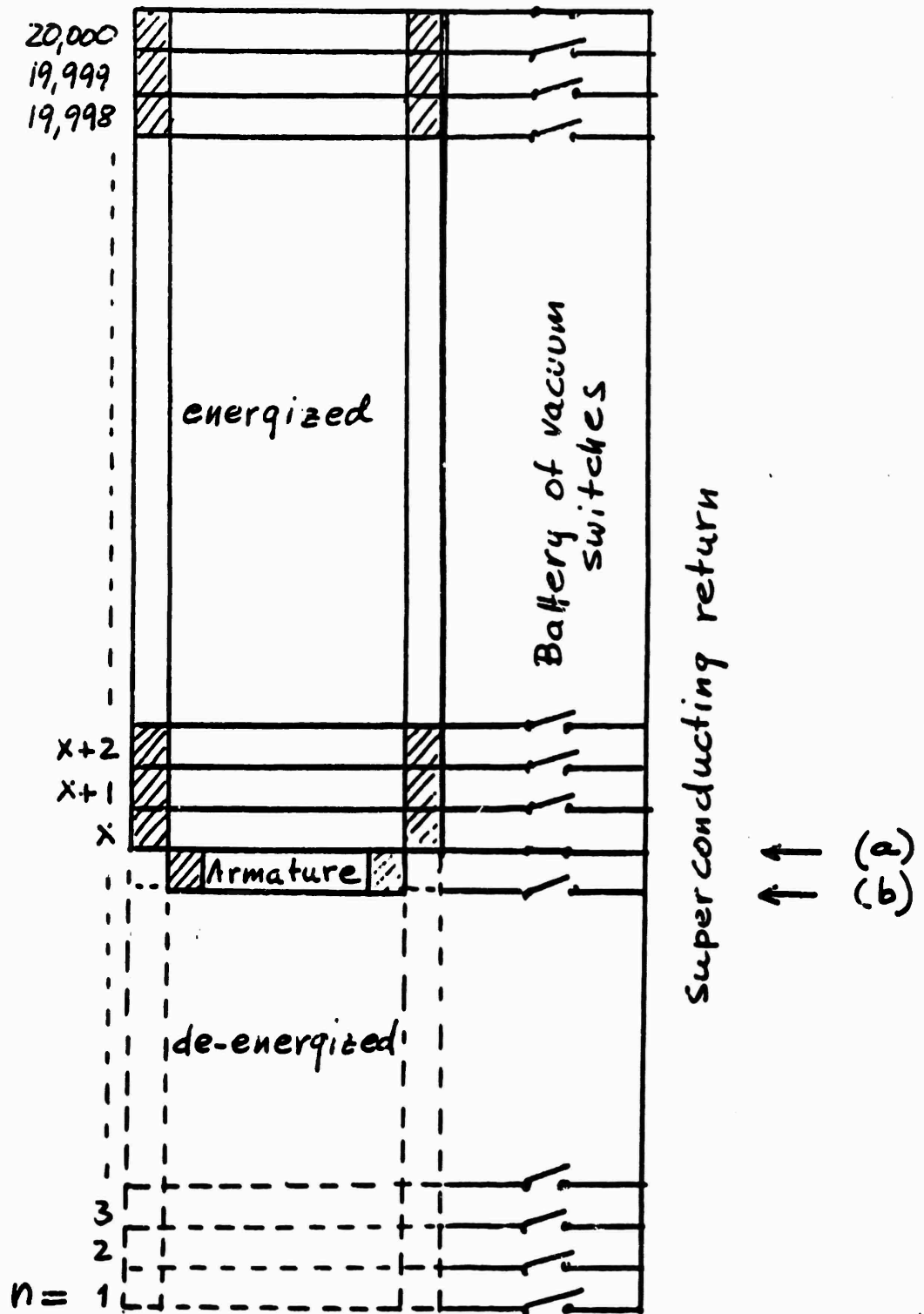


Fig. 2 Vacuum circuit breaker arrangement

would bring the current closer to the critical level.

Initially an arrangement was studied in which each drive coil was closed upon itself and isolated from all others. In this type of accelerator, it was found, current would pile up ahead of the armature coil, because of the switching operations, and it gave rise to strongly non-uniform acceleration of the projectile. As will be shown presently, the current pile-up problem is completely avoided by series-connection of all traction coils and the use of a return conductor.

To analyze the current transfer from the de-energized drive coil to the armature coil we make use of the fact that a perfect conductor (of zero resistivity) cannot sustain an internal electric field. Therefore, if e is the induced emf in a closed filament of the perfect conductor,

$$e = -d\phi/dt = 0 \quad \dots(10)$$

and the flux ϕ linked by the filament, or coil, has to remain constant. We may refer to this fact as flux conservation.

Flux conservation will make it, in general, impossible to maintain a positive (in the same direction as the solenoid current) ^{current} in the armature coil when the latter is charged a long way away from the drive solenoid. This is the result of the disparity of the selfinductances and magnetic field strengths of a long and a short coil. Hence the armature coil has to be charged in position at the inlet of the traction solenoid, as shown in fig.3(a). Assuming that the solenoid is charged first, armature and projectile have to be held back by a mechanical interlock while the armature current is being raised, by an external voltage source, to the desired level. During the charging process, the armature circuit includes resistance and the flux through it may change continuously. At the end of their respective charging cycles, both the solenoid and the armature have to be closed upon themselves by superconducting contacts to freeze in persistent currents. Breaking the mechanical interlock after charging of the armature will start the the flight of the projectile.

Let the initial solenoid current be $i_s = i_{n,1}$. As a first step, before releasing the armature, we will assume that the bottom coil of the solenoid ($n=1$) is interrupted just after $n=2$ has been connected to the return conductor. The current in

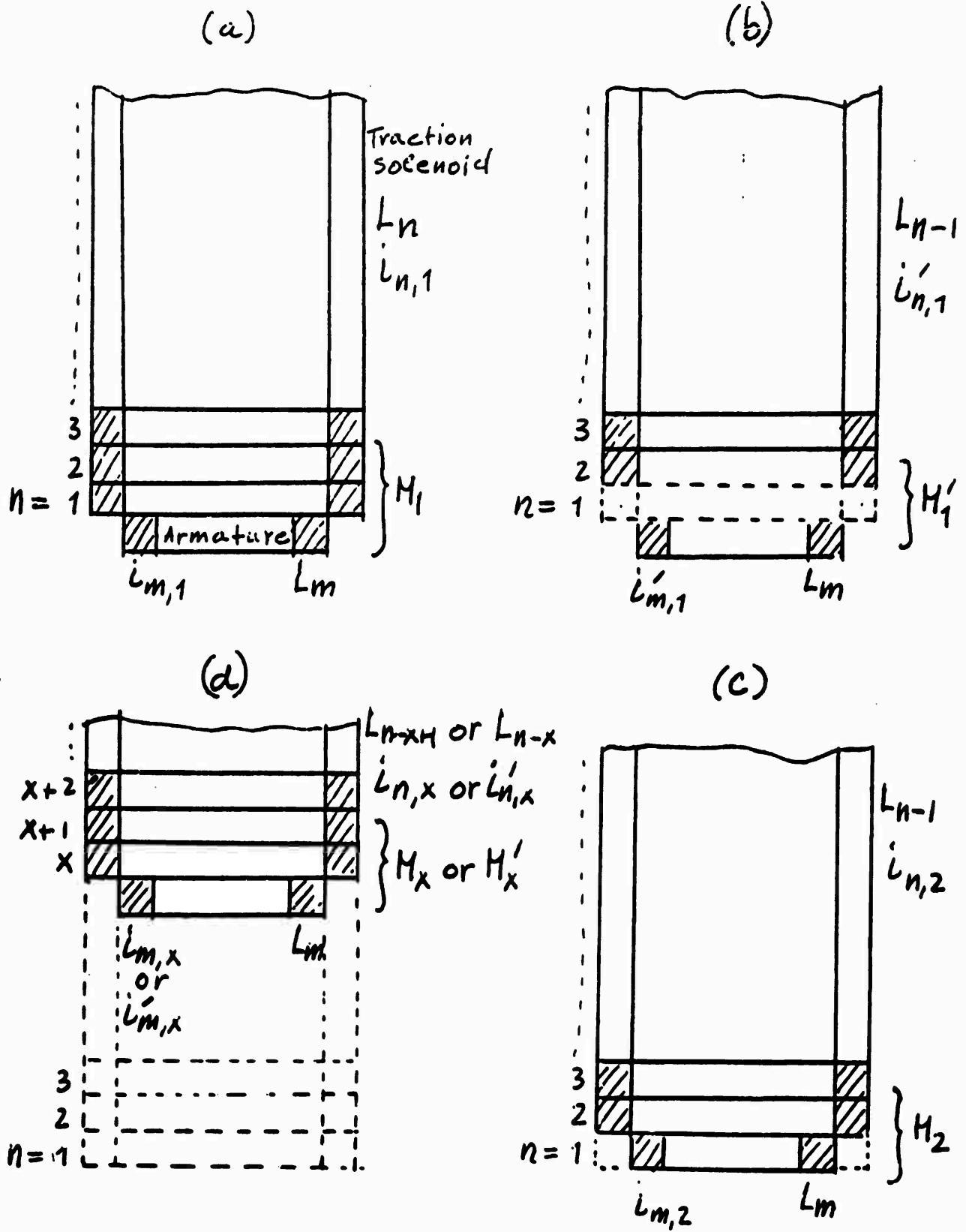


Fig. 3 Current and inductance notation

the solenoid should then increase from $i_{n,1}$ to $i'_{n,1}$ and the current in the armature from $i_{m,1}$ to $i'_{m,1}$. The following inductances are required for computing the variations in solenoid and armature currents:

L_m - selfinductance of armature coil

L_{n-x} - selfinductance of solenoid after opening the first x coils

M_x - mutual inductance between armature coil and energized portion of the solenoid just before the armature enters this energized portion (see fig.3)

M'_x - mutual inductance between armature coil and energized portion of the solenoid just after the current in the coil ahead of the armature has been interrupted (see fig.3)

Equating flux linkages in the solenoid and armature before and after interruption of the current in the drive coil $n=1$ gives

$$i'_{m,1}L_m + i'_{n,1}M_1 = i_{m,1}L_m + i_{n,1}M_1 \quad \dots(11)$$

$$i'_{n,1}L_{n-1} + i'_{m,1}M'_1 = i_{n,1}L_n + i_{m,1}M_1 \quad \dots(12)$$

Solving (11) and (12) for the adjusted currents $i'_{m,1}$ and $i'_{n,1}$ results in

$$i'_{m,1} = (M_1M'_1 - L_mL_{n-1}) / \{(M_1')^2 - L_mL_{n-1}\} i_{m,1} + (L_nM'_1 - L_{n-1}M_1) / \{(M_1')^2 - L_mL_{n-1}\} i_{n,1} \quad \dots(13)$$

$$i'_{n,1} = L_m(M'_1 - M_1) / \{(M_1')^2 - L_mL_{n-1}\} i_{m,1} + (M_1M'_1 - L_mL_n) / \{(M_1')^2 - L_mL_{n-1}\} i_{n,1} \quad \dots(14)$$

For the next step we consider the change in the currents from $i'_{m,1}$ to $i_{m,2}$ and $i'_{n,1}$ to $i_{n,2}$ as the armature coil moves up to the energized portion of the solenoid, as indicated in fig.3(c). Flux conservation then demands

$$i_{m,2}L_m + i_{n,2}M_2 = i'_{m,1}L_m + i'_{n,1}M'_1 \quad \dots(15)$$

$$i_{n,2}L_{n-1} + i_{m,2}M'_2 = i'_{n,1}L_{n-1} + i'_{m,1}M_1 \quad \dots(16)$$

Solving (15) and (16) for the adjusted currents $i_{m,2}$ and $i_{n,2}$ produced by the forward motion of the armature by 5 cm gives

$$i_{m,2} = (M'_1M_2 - L_mL_{n-1}) / (M_2^2 - L_mL_{n-1}) i'_{m,1} + L_{n-1}(M_2 - M'_1) / (M_2^2 - L_mL_{n-1}) i'_{n,1} \quad \dots(17)$$

$$i_{n,2} = L_m(M_2 - M'_1)/(M_2^2 - L_m L_{n-1})i'_{m,1} + (M_2 M'_1 - L_m L_{n-1})/(M_2^2 - L_m L_{n-1})i'_{n,1} \dots\dots(18)$$

This procedure can be repeated step-by-step until $\lambda - 1$ coils of the solenoid have been opened and the armature has moved right up to the portion of the solenoid still carrying current, as in fig.3(d), when the armature and solenoid currents will be

$$i_{m,x} = (M'_{x-1} M_x - L_m L_{n-x+1})/(M_x^2 - L_m L_{n-x+1})i'_{m,x-1} + L_{n-x+1}(M_x - M'_{x-1})/(M_x^2 - L_m L_{n-x+1})i'_{n,x-1} \dots\dots(19)$$

$$i_{n,x} = L_m(M_x - M'_{x-1})/(M_x^2 - L_m L_{n-x+1})i'_{m,x-1} + (M_x M'_{x-1} - L_m L_{n-x+1})/(M_x^2 - L_m L_{n-x+1})i'_{n,x-1} \dots\dots(20)$$

And after interruption of the current in the next drive coil, the two currents become

$$i'_{m,x} = (M_x M'_x - L_m L_{n-x})/((M'_x)^2 - L_m L_{n-x})i_{m,x} + (L_{n-x+1} M'_x - L_{n-x} M_x)/((M'_x)^2 - L_m L_{n-x})i_{n,x} \dots\dots(21)$$

$$i'_{n,x} = L_m(M'_x - M_x)/((M'_x)^2 - L_m L_{n-x})i_{m,x} + (M_x M'_x - L_m L_{n-x+1})/((M'_x)^2 - L_m L_{n-x})i_{n,x} \dots\dots(22)$$

In order to evaluate equations (19) to (22) it is necessary to compute the numerical values of the eight dimensionless inductance coefficients of these equations. The only constant in those coefficients is the armature selfinductance. Its value is

$$L_m = 287 \text{ cm} \dots\dots(23)$$

Grover formulas have been used for (23) and the calculation and the variable self-inductance L_x of the energized portion of the solenoid. The results are plotted on fig.4.

Grover also provides a formula for the mutual inductance M between a long solenoid and a coaxial circular filament in the end-plane of the solenoid. For the 20,000 coils of the traction solenoid, this value of M must be equal to

$$M = \sum_{n=1}^{20,000} M_{m,n} = \sum_{n=1}^{1000} M_{m,n} \dots\dots(24)$$

The Grover formula also shows that for the dimensions of the solenoid of fig.1,

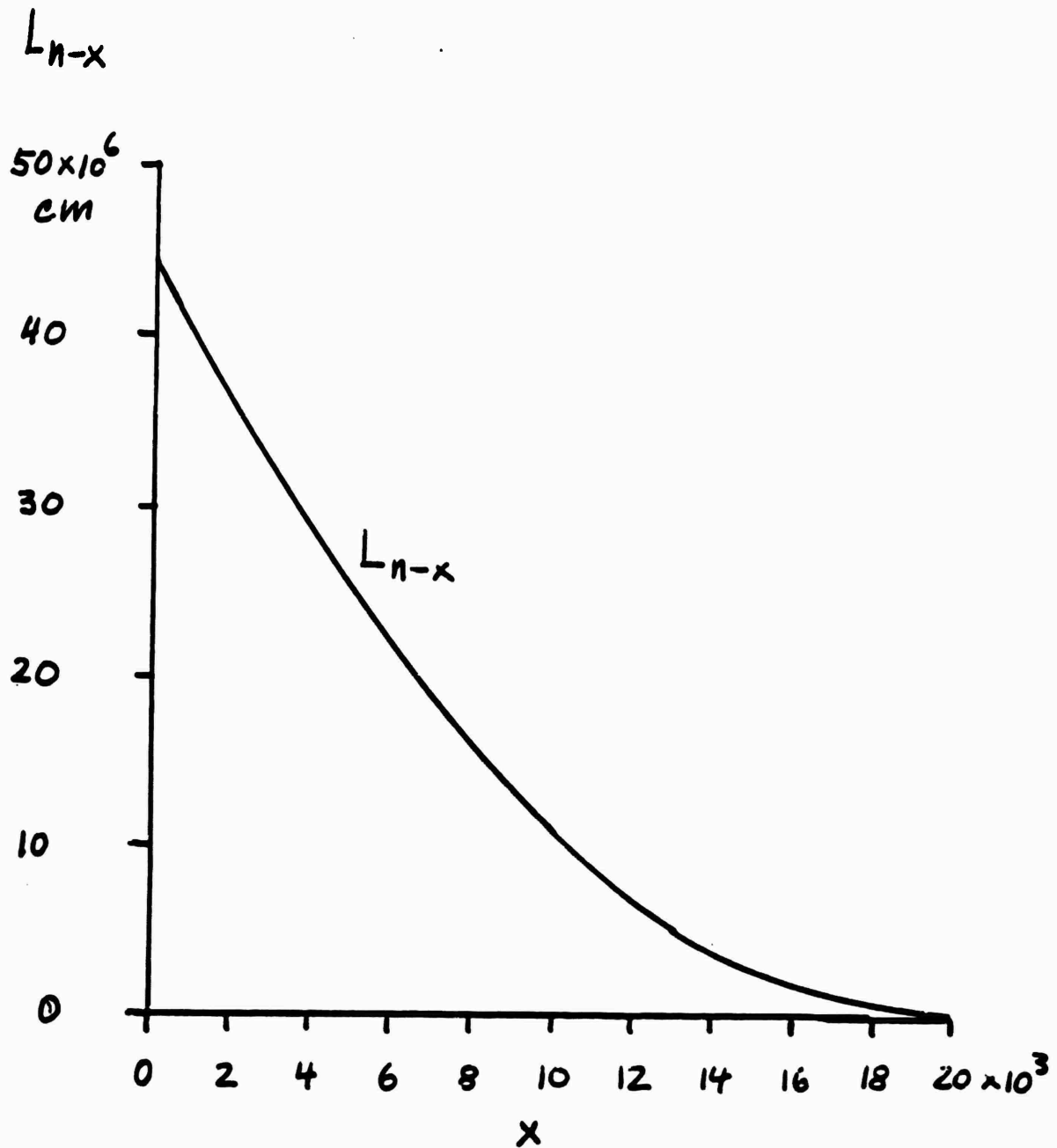


Fig. 4 Selfinductance of energized portion of the traction solenoid

coils 1001 to 20,000 make virtually no contribution to M, which justifies the approximation in (24). Hence the mutual inductance is very nearly constant until the projectile has traversed 95 percent of the accelerator. Over this ^{initial} distance

$$M_x = M - M_{m,1} \dots\dots(25)$$

where $M_{m,1}$ is the mutual inductance between the armature coil and a drive coil directly surrounding the armature. Also

$$M'_x = M - M_{m,1} - M_{m,2} \dots\dots(26)$$

where $M_{m,2}$ is the mutual inductance between the armature and the drive coil just ahead of it. Using Grover formulas, the mutual inductances of '25) and (26) were found to be

$$M_x = 392 \text{ cm} \dots\dots(27)$$

$$M'_x = 212 \text{ cm} \dots\dots(28)$$

While the projectile travels through the last 1000 coils of the solenoid, both M_x and M'_x decrease from the values given in (27) and (28).

We are now able to compute the numerical value of the first inductance coefficient in (19) for $0 < x < 19,001$.

$$\frac{(M'_{x-1}M_x - L_m L_{n-x+1}) / (M_x^2 - L_m L_{n-x+1})}{= 1} = \frac{(212 \times 392 - 287 L_{n-x+1}) / (392^2 - 287 L_{n-x+1})}{\dots\dots(29)}$$

For all values of $L_{n-x+1} < 19,000$ we have $L_{n-x+1} > 0.25 \times 10^6$. Hence for the first 950 m of the solenoid the inductance coefficient of (29) is very nearly equal to one.

The second inductance coefficient of (19) is

$$\frac{L_{n-x+1}(M_x - M'_{x-1}) / (M_x^2 - L_m L_{n-x+1})}{= -0.627} = \frac{L_{n-x+1} (392 - 212) / (392^2 - 287 L_{n-x+1})}{\dots\dots(30)}$$

The remaining inductance coefficients of equations (20) to (22) are

$$\frac{L_m(M_x - M'_{x-1}) / (M_x^2 - L_m L_{n-x+1})}{= 0} = \frac{287(392^2 - 212) / (392 - 287 L_{n-x+1})}{\dots\dots(31)}$$

$$\frac{(M_x M'_{x-1} - L_m L_{n-x+1}) / (M_x^2 - L_m L_{n-x+1})}{= 1} = \frac{(392 \times 212 - 287 L_{n-x+1}) / (392^2 - 287 L_{n-x+1})}{\dots\dots(32)}$$

$$\frac{(M_x M'_x - L_m L_{n-x}) / ((M'_x)^2 - L_m L_{n-x})}{= 1} = \frac{(392 \times 212 - 287 L_{n-x}) / (212^2 - 287 L_{n-x})}{\dots\dots(33)}$$

$$\begin{aligned} (L_{n-x+1} M_x' - L_{n-x} M_x') / \{(M_x')^2 - L_m L_{n-x}\} &= (212 L_{n-x+1} - 392 L_{n-x}) / (212^2 - 287 L_{n-x}) \\ &= +0.627 \end{aligned} \quad \dots (34)$$

$$\begin{aligned} L_m (M_x' - M_x) / \{(M_x')^2 - L_m L_{n-x}\} &= 287(212^2 - 392) / (212^2 - 287 L_{n-x}) \\ &= 0 \end{aligned} \quad \dots (35)$$

$$\begin{aligned} (M_x M_x' - L_m L_{n-x+1}) / \{(M_x')^2 - L_m L_{n-x}\} &= (392 \times 212 - 287 L_{n-x+1}) / (212^2 - 287 L_{n-x}) \\ &= 1 \end{aligned} \quad \dots (36)$$

Substituting approximations (29) to (36) into (19) to (22) gives the currents as

$$i_{m,x} = i_{m,x-1} - 0.627 i_{n,x-1} \quad \dots (37)$$

$$i_{n,x} = i_{n,x-1} \quad \dots (38)$$

$$i_{m,x} = i_{m,x} + 0.627 i_{n,x} \quad \dots (39)$$

$$i_{n,x} = i_{n,x} \quad \dots (40)$$

Equations (38) and (40) prove that the solenoid current remains constant until the projectile reaches the last 50 m of the traction solenoid. The stability of i_n is the result of the large selfinductance of the solenoid compared to that of the armature coil.

Equation (39) expresses the increase in armature current due to the extinction of the current in the drive coil just ahead of the armature. This is the current transfer equation. According to (37), the transferred current is lost again when the armature moves up to the energized portion of the solenoid. Hence for the first 950 m of its travel into the solenoid the armature current varies in saw-tooth fashion between $i_{m,1}$, the current to which the armature was originally charged, and this current plus 62.7 percent of the solenoid current. Each circuit breaker therefore pumps a certain amount of current (ampere-turns) from the solenoid to the armature, and this is expended in acceleration before the next pumping stroke occurs. In the last 50 m of the solenoid, the average armature current decreases and the drive current increases, keeping the acceleration approximately constant right up to the exit of the projectile from the accelerator.

The current fluctuations in the armature coil will be smoothed out to a considerable extent by the gradual arc quench in the vacuum interrupter. The saw-tooth waveform of the armature current arises from the assumption that the current is

extinguished instantaneously. In practice this is impossible, a fact which will help to keep the armature current more constant. But it seems unavoidable that the armature current contains as significant ac component which increases in frequency as the projectile accelerates, reaching several hundred kilo-hertz at the end of the accelerator. This will give rise to ac losses in the armature circuit which, together with heat inleak and friction ~~and also generated heat~~, will have to be absorbed by the coolant and the cold metal. Fortunately the process of acceleration through the whole length of the solenoid takes only 0.2 s.

It will be seen from (34) that the amount of current pumped into the armature by each circuit breaker is determined by $(M'_x - M_x)/L_m$. The numerator of this fraction depends on the number of circuit breakers installed along the solenoid. The larger this number, the smaller will be the current pumped with each stroke. The number of circuit breakers that can be usefully employed is ultimately determined by their speed of operation. A larger selfinductance of the armature coil will also reduce the amount of current pumped per stroke. This would be best achieved by lengthening the armature coil.

In the present example in which a solenoid current of 100 A has been assumed, the initial armature current $i_{m,1}$ should not be larger than 37.3 A to prevent the current density in the armature coil from exceeding that in the solenoid.

3.0 PERSISTENT CURRENT MAINTENANCE AND INTERRUPTION

The maintenance of persistent currents through mechanical contacts and the arc interruption of these currents is an uncharted area of technology. The contacts would operate in hard vacuum and therefore could be kept very clean, except for a monolayer of gas. By using adequate pressure, it is hoped that superconducting contact can be made reliably between niobium electrodes. The contacts would have to be internally cooled with helium or by conduction to a helium pool.

A very large number of solenoid turns has been chosen in the present example to keep the current small and therefore interruptible. Even with vacuum circuit

breakers it is difficult to interrupt dc currents of 1000 A or more. The voltage drop across the arc is of the order of 20-100 V, depending on the ionization potential of the metal vapor atoms. This is a very small voltage compared with the self-induced emf's which will normally try to maintain the current constant. However, the proximity of the short-circuited armature coil of zero resistance experiences similar emf's which result in ~~the~~ current transfer and by this action reduce the self-induced emf in the drive coil circuit which is being opened. This sequence of events should greatly help with the extinction of the drive coil current.

Furthermore, a 100 A arc generates relatively little heat and this will starve the arc of ^{metal} ions and make it unstable. With this small amount of current the gap plasma may have more the nature of a glow discharge than an arc. Glow discharges are capable of opposing much larger induced voltages than arcs. Another technique used for dc vacuum arc extinction is the application of a crossed magnetic field to divert electrons into the vacuum background.

Of the twin problems of the maintenance of persistent currents through mechanical contacts and dc arc interruption, the former is expected to be the more difficult one to solve. An essential step in establishing the feasibility of the superconducting earth launcher has to be some experimental evidence of the working of the make and break action of the vacuum switches. Arc interruption could be explored with normal conductors at liquid nitrogen temperature, but persistent current contact experiments require liquid helium cooling.

4.0 SOLENOID FORCES

Another critical issue are the maximum mechanical stresses that may arise in the traction solenoid from the combination of axial magnetic pressure, acceleration force and weight. According to formulas and tables provided by Grover, the force of attraction between the two halves of the solenoid comes to

$$F = 309,000 \text{ kg} \quad \dots(41)$$

The winding contact area between the two halves is

$$A = (\pi/4)(40^2 - 30^2) = 550 \text{ cm}^2 \quad \dots(42)$$

Hence the compressive stress across the midplane of the solenoid is

$$F/A = 562 \text{ kg/cm}^2 \approx 8000 \text{ psi} \quad \dots(43)$$

The weight of half the column of the solenoid adds to the stress of (43). For an aluminum/niobium ratio of 3:1, the average density of the superconductor would be 4.17 g/cm^3 . The total weight of the solenoid column therefore is

$$W_{Al} = 4.17 \times 10^{-3} A \ell = 230,000 \text{ kg} \quad \dots(44)$$

The compressive stress due to this weight at the bottom of the column is

$$W_{Al}/A = 417 \text{ kg/cm}^2 \approx 6000 \text{ psi} \quad \dots(45)$$

Half this stress added to the axial compression makes the midplane stress 11,000 psi.

The maximum stress would actually occur below the midplane and it may be too high for pure aluminum. With a copper-backed superconductor the compressive stresses in the solenoid would be even higher because of the greater specific gravity of copper, but pure copper would tolerate 20,000 psi. The difficulty with copper is that its oxides are inadequate electrical insulation and G10 sheets may have to be inserted between pancake coils.

5.0 SPACE DISPOSAL OF HAZARDOUS WASTE

A small launch facility, as the one studied in this investigation, may find application in the space disposal of hazardous waste. Radioactive substances from various nuclear programs are obvious candidate materials. Small-packet launching would greatly reduce the risks associated with aborted space shots. Rocket launching of payloads of the order of 20 kg is completely out of the question on account of the amount of fuel required per shot.

Assuming an 80 percent charging efficiency, each shot of the superconducting earth launcher would consume under 5000 kWh of electricity at a cost of less than \$ 500.